Doctoral Dissertation

IMPROVEMENT OF DIMENSIONAL ACCURACY USING BENDING COMPENSATION FRAMEWORK IN A SELECTIVE LASER SINTERING

Sangho Ha

Department of System Design and Control Engineering

Graduate School of UNIST

2019

IMPROVEMENT OF DIMENSIONAL ACCURACY USING BENDING COMPENSATION FRAMEWORK IN A SELECTIVE LASER SINTERING

Sangho Ha

Department of System Design and Control Engineering

Graduate School of UNIST

Improvement of dimensional accuracy using bending compensation framework in a selective laser sintering

A dissertation
submitted to the Graduate School of UNIST
in partial fulfillment of the
requirements for the degree of
Doctor of Philosophy

Sangho Ha

12 / 14 / 2018

Approved by

Namhun Kim

Advisor
Namhun Kim

Improvement of dimensional accuracy using bending compensation framework in a selective laser sintering

Sangho Ha

This certifies that the dissertation of Sangho Ha is approved.

12 / 14 / 2018

Namhun Kim

Advisor: Namhun Kim

Duck Young Kim

Daeil Kwon

Young-Bin Park

In Gwun Jang

Abstract

At present, additive manufacturing (AM) technology is getting attention as an innovative technology in the industrial sector. Particularly, AM methods using powder materials, for example, selective laser sintering (SLS) and selective laser melting (SLM), have attracted attention. This is because the above manufacturing methods (SLS and SLM) use materials similar to or the same as parts used in traditional manufacturing methods. In this study, I specifically focus on SLS. The selective laser sintering (SLS) processes are known for enhancing the engineering properties and durability of parts that are widely used for rapid prototyping and rapid manufacturing in auto part development processes, such as prototypes for assembly tests, and jig production. The geometric deformations of the three-dimensional (3D) printed parts, however, frequently hinder manufacturers from applying the technology to the direct manufacturing of the automotive parts.

In order to mitigate the shape deformation of AM parts, I focused on the deformation factors of AM parts. One of the deformation factors is the densification of materials among various processing parameters which cause shape deformations. The correlation between the degree of contraction and the energy density is analyzed by measuring the density variation of AM parts. In addition, I analyzed the overall deformation patterns and provides manuals for improving the dimensions of 3D printed parts. After fabrication, the validation of the analytic model and the effective compensation method for getting more accurate AM parts was also presented.

In this research, I propose a systematic dimensional compensation framework and validate it by studying the bending deformation patterns of 3D printed vehicle parts using the SLS platform. During the experimental phase of this research, specially designed samples with multiple features were produced and, by using them, the reference 3D deviation of the SLS process was analyzed. Next, the deformation patterns are formulated with polynomial regression model in the global Cartesian coordinates of the platform. Then, the dimensional compensation was implemented and the original 3D Computer-Aided Design(CAD) file is pre-processed with an inverse transformation of the features to compensate the deformation patterns.

A software package to provide the automated compensation for AM parts was implemented to present the applicability of the proposed method, which is statistically shown to effectively predict the deformation and significantly mitigate deformations of the auto parts in SLS. The compensation software system is currently being used by a vehicle manufacturer for manufacturing of prototypes.

Through these processes, I can contribute to the improvement of dimensional accuracies for AM. The improvement of accuracy of AM parts reduce post-processing and minimize the cost and time through this compensation framework. This would highlight the advantages of AM, which would extend the applications of AM. It is expected to apply the systematic dimensional compensation

method to improve the manufacturing accuracy not only in SLS but also in other types of AM processes (e.g., SLM) for various industrial applications.

Contents

List of Figures

List of Tables

1. Introduction

1.1 Additive manufacturing (AM)

According to ISO/ASTM 52900, the definition of additive manufacturing (AM) is “the process of joining materials to make parts from 3D model data, usually layer upon layer, as opposed to subtractive and formative manufacturing methodologies” (ASTM, 2012). AM related technology can be divided into three major categories. First, pre-processing technology usually refers to 3D model related work, such as slicing operations or support structure designs for 3D printing. Second, printing related technology usually refers to 3D printing methods, such as selective laser sintering (SLS), and stereolithography (SLA). The final technology is a post-processing technology. Examples of post-processing techniques include support material removal, heat treatment, and polishing (Wohlers, 2018).

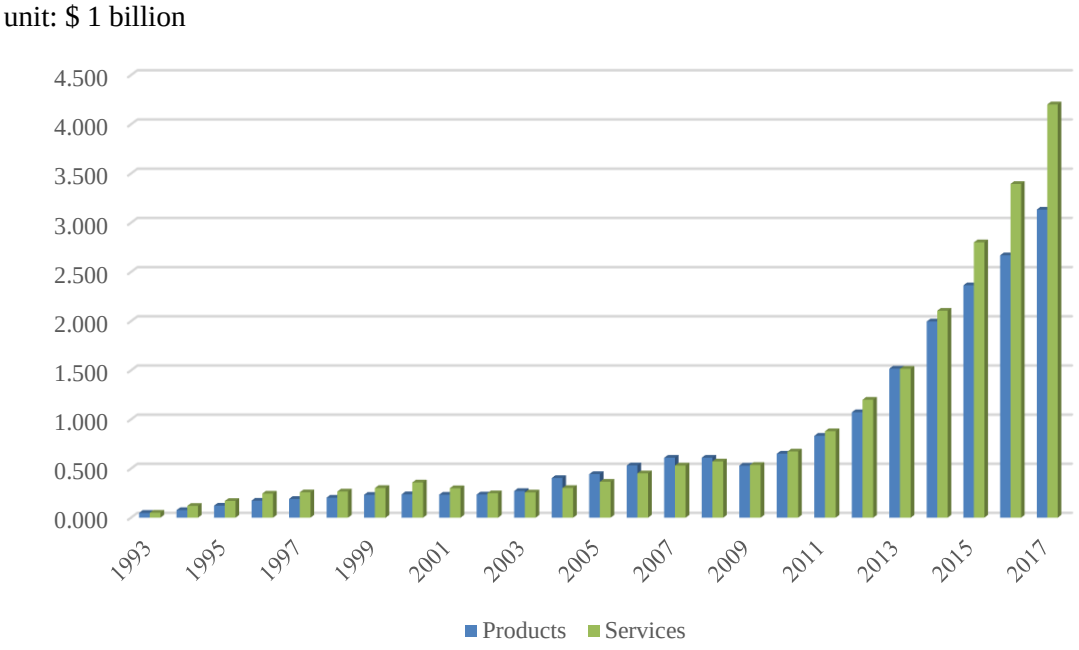

Figure 1-1 Worldwide revenues from AM (Wohlers, 2018)

AM is currently attracting attention as an important next-generation manufacturing method, and AM-related businesses are growing rapidly. Figure 1-1 shows the change in profits of AM businesses in the world over the last 25 years. In 2017, AM products earned $ 3.133 billion. AM product sales revenue has continued to increase since 2009, and AM product sales revenue in 2017 increased by 17.4% compared to 2016 revenue. AM service revenues have also increased steadily since 2009, the same as AM product revenues. In 2017, AM services earned $ 4.202 billion. This is an increase of

21.2% compared to 2016 and service revenues are showing a recent sharp increase compared to AM product revenues (Wohlers, 2018).

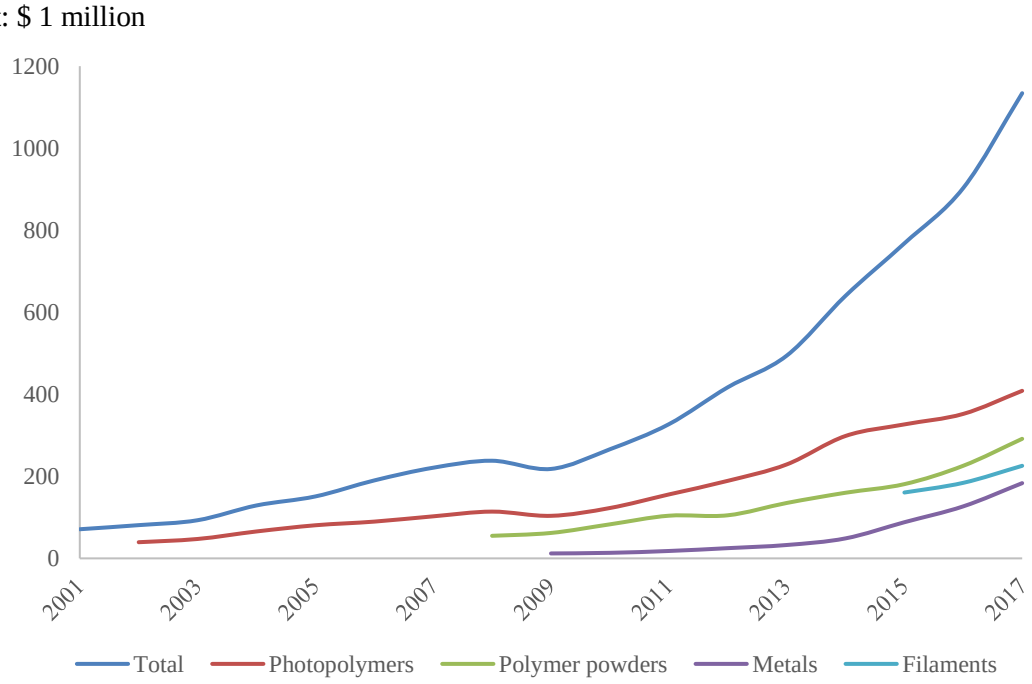

Figure 1-2 Additive manufacturing material sales (Wohlers, 2018)

AM technologies are available in a variety of ways and thus use a variety of materials. The consumption of materials is steadily increasing every year, with photopolymers making up the largest proportion, while polymer powder materials are in second place. The consumption of metal has shown the sharpest increase in recent years (Figure 1-2) (Wohlers, 2018).

Then, what are the merits of AM? Compared to conventional manufacturing methods, AM methods have the following advantages (Attaran, 2017; Gao et al., 2015; Huang et al., 2014).

-. Sustainable manufacturing: The conventional subtractive manufacturing makes products by cutting large base materials. However, AM is a method of stacking layers one by one. Therefore, unlike conventional methods, very few materials are wasted.

-. Decentralized manufacturing: Since AM technology spreads around the world, products designed with CAD software can be produced anywhere in the world with only those files. In other words, it can be produced without additional transportation costs and time through 3D printing companies all over the world.

-. Production Flexibility: With AM technology, it is possible to easily change products without additional parts or costs through CAD file modification. Therefore, it is possible to easily manufacture products according to the consumers' demands without additional cost.

-. Part Flexibility: Compared to conventional manufacturing methods, the AM methods almost never have design constraints. Therefore, it is possible to fabricate a very complicated shape, and it is very easy to apply a lightweight design through AM.

However, AM technology still has the following drawbacks compared to conventional manufacturing methods. In particular, the drawbacks are more pronounced in the mass production field (Huang et al., 2014).

-. Size Limitation: Most AM machines have limited production sizes. Each layer is built using laser sources to melt or to harden the material or using motors to eject the material or the binder. Therefore, it is difficult to mechanically manufacture a large AM machine. Also, it is difficult to fabricate large size products because manufacturing errors may occur due to deformation problems in the manufactured products.

-. Material Limitation: Compared to conventional manufacturing processes, the materials available for AM technology are limited. However, the choices of materials currently used in AM technology is increasing as AM develops.

-. Imperfections: When manufacturing parts using AM equipment, it is necessary to carry out some additional work such as removing the support structure or removing the powder. Depending on the AM process, surface treatment may be required.

-. Lower Precision: There is still a shortage of precision in the AM manufacturing methods compared to the subtracted manufacturing method.

To solve these problems, various studies are being conducted. First, researchers are studying what is known as Big Area Additive Manufacturing (BAAM) to solve the limitations of size. Attempts have been made to manufacture a full-size car using BAAM (Talagani et al., 2015). Second, the choice of materials is increasing as AM develops. For example, Markforged Inc. has developed carbon printing technology (Ahmed, 2017). In the case of imperfections, there has been some research about hybrid manufacturing and production constraints (Newman, Zhu, Dhokia, & Shokrani, 2015; Di Wang, Yang, Yi, & Su, 2013).

1.2 Motivation

Currently, AM technology is being applied to various industrial sectors. In the field of aircraft, AM technology is used in the manufacture of diverse parts. It is widely used in the field of medical devices to make implants. In contrast to traditional method with constraints in geometric design, AM can provide almost complete design freedom for part fabrication (Beyer, 2014). It is also widely used in the automotive field and is being applied to the development and practical use of these parts by BMW, Inc. In the case of Local Motors, Inc, the entire automobile is manufactured using AM technology. However, as it is difficult to control the dimensional stability and accuracy of AM, AM products often require post-processing or re-production. So, it is difficult to get the benefits of AM because of the additional cost and time involved. Therefore, despite the many advantages of AM, global automotive companies have difficulties in applying AM (Sangho Ha et al., 2015; Sangho Ha et al., 2018; Hopkinson & Sercombe, 2008; Huang, 2016; Huang et al., 2014; Huang, Zhang, Sabbaghi, & Dasgupta, 2015; Islam & Sacks, 2016; S. Jin, Liu, Lai, Li, & He, 2017; Luan & Huang, 2015; S. Singh, Sachdeva, & Sharma, 2012; Soe, 2012; Soe, Eyers, & Setchi, 2013; S. Song, Wang, Huang, & Tsung, 2014; Tong, Amine Lehtihet, & Joshi, 2003; Tong, Joshi, & Amine Lehtihet, 2008; A. Wang, Song, Huang, & Tsung, 2017).

In order to apply AM technology to industry, it must be possible to satisfy the dimensional requirements. In the case of AM, unlike existing technologies, there are many shortcomings in this area because of the short research period. For example, in the case of SLS devices, calibration is basically performed after the installation of the device. Calibration method calculates the contraction rate in each direction of x, y, and z, adjusts the scale factor and adjusts the part bed temperature before manufacturing. However, looking at the example shown in Figure 1-3, despite these adjustments, when the engine block or the crankshaft is manufactured, the following deflection occurs, and the dimension of the tail lamp cannot satisfy the dimensional requirements. In order to solve this problem, there is a method of post-processing through Computerized Numerical Control (CNC). In case of such a large deformation, post-processing is difficult to correct, so those samples are discarded. The new samples are then re-produced with the consideration that they will be modified by the CNC. However, in this case, additional costs and time are required. Therefore, it is difficult to fully demonstrate the advantages of AM due to the additional charge.

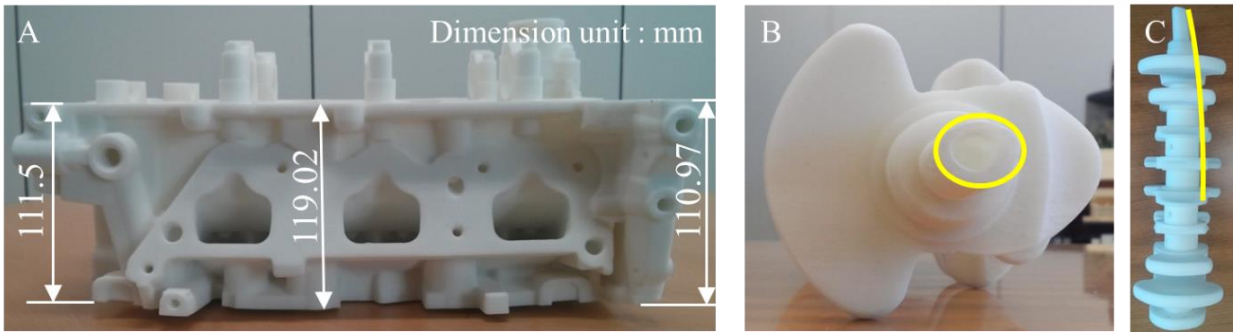

Figure 1-3 SLS 3D printed samples (A): Engine block (B, C): Crank shift

Therefore, investigation and analysis of the AM process, especially SLS, were carried out to recognize and solve these problems. In the following studies, I investigated the causes of dimensional deformation and dependent parameters. And I proposed methods to improve dimensional accuracies in SLS processes (Sangho Ha et al., 2015; Sangho Ha et al., 2018; S Ha, Ransikarbum, & Kim, 2016), and process management methods for dimensional quality control (Kwon, Park, Ha, & Kim, 2017; J.-y. Park, Ha, Park, Kwon, & Kim, 2016).

1.3 Objective

For the reasons explained in the motivation section, the main objective of this study is to improve the dimensional accuracy of AM. To achieve this objective, the detailed objectives are classified as follows. First, to find the causes of deformation in SLS. Based on the results, a deformation prediction model is presented. This deformation prediction model also suggested methods for improving the dimensions. In this study, a compensation model is presented, and the parameters used in this compensation model were the main effects of the analysis on the cause result of the deformation. The aforementioned compensation model was then validated. In particular, it was intended to demonstrate actual availability by using complex feature models used in actual industrial sites. To summarize detailed objectives, they are as follows

- To find the causes of deformation in SLS
- To suggest a predictive deformation model
- To suggest methods to improve dimensional accuracy
- To validate the compensation model

1.4 Outline

In this study, I will deal with the dimension related issues of additive manufacturing. The overall outline is shown in Figure 1-4 below. First, I tried to understand the causes of dimensional deformation. This is the focus of Chapter 3. To be more specific, Analysis of the causes of dimensional deformation is through the process of presenting an analytic deformation model and verifying it. Additionally, an effect pattern analysis was performed on the deformation for each parameter. In Chapter 4, I analyze the cause of dimension deformation and then identify the pattern and finally, alleviate it. To do this, I developed a compensation model by analyzing dimensional deformation according to each parameter change and then proposed a framework for applying this model. In the last Chapter, the compensation model was verified by applying it to actual vehicle parts. Ultimately, further studies will develop the final compensation model, which includes analytic deformation model and contraction according to their locations of layout found in pattern analysis, in the bending compensation model presented below.

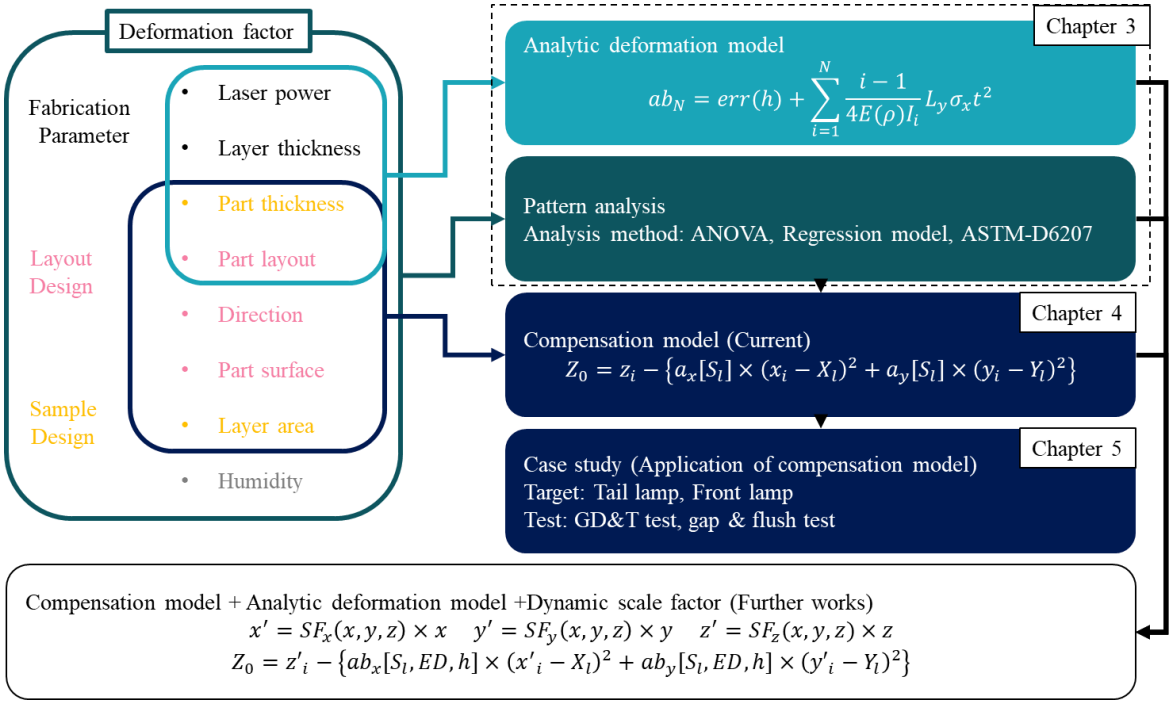

Figure 1-4 The proposed framework for controlling the dimensional accuracy of additive manufacturing samples

2. Literature survey

Before carrying out this research, papers related to dimension accuracy and the dimensional reliability of powder-based fusion type AM technologies were studied. In this Chapter, the relevant research is summarized, starting with the types of AM technologies. Particularly, powder-based fusion type AM are summarized. And then, I provide information on studies on dimensional deformation and parameters related to dimensional deformation. In addition, the studies on theoretical deformation models were summarized, particularly those related to the model applied to the selective laser mapping (SLM). I also investigated the methods of dimension improvement through existing CAD model modifications.

2.1 The Processes of AM

The AM process is shown in Figure 2-1. It can be broadly divided into four stages: pre-processing, fabricate processing post processing and finally the verification and management process (I. Gibson, 2010; Yang, Kong, & Sarder, 2016).

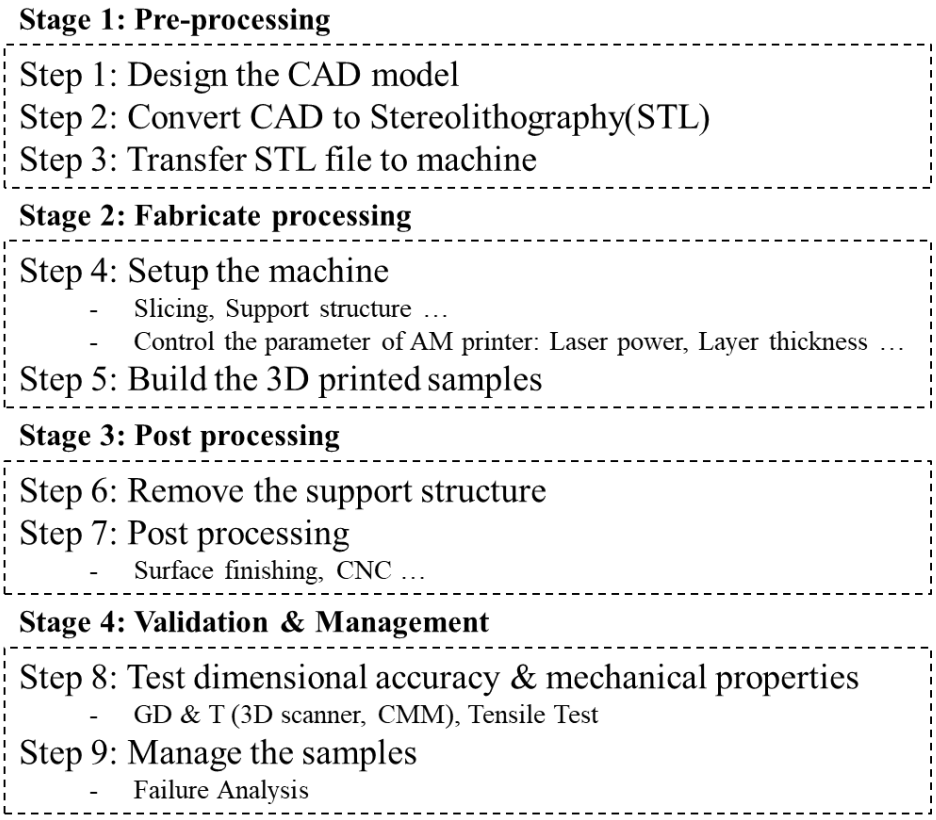

Figure 2-1 The flow chart of Additive manufacturing process

In the pre-processing stage, a CAD model is created and then converted into an STL file. The STL format is a format developed by 3D Systems Inc in 1989, which consists of a solid model with

triangular faces. The STL format is commonly used in the AM industry (Moodleah, Bohez, & Makhanov, 2016). I then move the STL file to the 3D printer.

The next step, fabricate processing, can be divided into a machine setting process and a sample production process. The machine setting process can be divided into slicing operation, support structure, and AM printer parameter setting. There is a difference between printers, so there are some cases where the sample layout, support structure and the slicing of the STL file for printing are set before being transferred to the printer. But this does not affects the following steps. Then, 3D printed samples are built up and made.

After fabricate processing, post-processing is needed. Basically, most of the 3D printing methods require support structures, so the process of removing them is needed. In the case of printed samples, the surface is rough, and some raw materials remain, depending on the manufacturing method. Thus, this material is removed, and the surface of the samples is treated. In some cases, heat treatment is used to adjust the strength, and Computerized Numerical Control (CNC) is used to adjust tolerance.

Finally, in order to use 3D printing samples in industry, it is necessary to verify and manage manufactured parts. The verification process requires measurement using a Coordinate-measuring machine(CMM) or 3D scanner for GD & T verification, followed by a tensile test for measuring the material properties of 3D printed parts.

2.2 The classification of AM

Recently, emphasis in the AM community has moved towards rapid manufacturing for end-use parts. AM refers to a set of technologies used to produce end-use parts directly from 3D CAD models by additively building them in layers (Goodridge, Tuck, & Hague, 2012). The American Society for Testing and Materials (ASTM, 2012) has standardized and classified AM technologies into seven main categories: 1) photopolymer vat, 2) material extrusion, 3) powder bed fusion, 4) directed energy deposition, 5) sheet lamination, 6) material jetting, and 7) binder jetting. The definition of each process is shown in Table 2-1. The seven categories above can be divided into liquid-type materials, solid-type materials and powder-type materials (Kruth, 1991). Powder-type material is used in binder jetting and powder bed fusion. Vat photopolymerization and material jetting use a liquid-type material. Material extrusion and sheet lamination use a solid type material. AM technologies have been used for a long time in rapid prototyping applications. Other terms commonly used for AM include Additive Fabrication (AF), Direct Digital Manufacturing (DDM), Layer Manufacturing (LM), Solid Free Form Fabrication (SFF), Rapid Manufacturing (RM), Additive Layered Manufacturing (ALM), and 3D printing (3DP) (ASTM, 2012; Gao et al., 2015).

Examples of AM technologies using powder-type materials include Selective Laser Sintering (SLS), Selective Laser Melting (SLM), Electron Beam Melting (EBM), Direct Metal Deposition (DMD) and 3 Dimensional Printing (3DP). They differ in the bonding mechanism, laser source, and material. In AM methods which use powder-type material, the parts are produced through a laser source or binding source that is selectively applied to build each layer (Guo & Leu, 2013). Among the AM production methods using powder bed fusion type technology, SLS, SLM, and EBM are similar. Powder bed fusion type AM technology allows complex 3D objects to be built by selectively fusing together successive layers of powdered materials. The component production is made according to a 3D CAD file, typically in an STL file format. The model file is then sliced into discrete layers, where each slide represents a cross-section of the part.

Table 2-1 The classification of additive manufacturing (ASTM, 2012)

Categories	*Definition*	*Processes*
Material extrusion (ME)	"an additive manufacturing process in which material is selectively dispensed through a nozzle or orifice"	Fused Filament Fabrication (FFF)
Material jetting (MJ)	"an additive manufacturing process in which droplets of build material are selectively deposited"	Polyjet; Multi Jetting Modeling (MJP)
Binder jetting (BJ)	"an additive manufacturing process in which a liquid bonding agent is selectively deposited to join powder materials"	3 Dimensional Printing (3DP)
Sheet lamination (SL)	"an additive manufacturing process in which sheets of material are bonded to form a part"	Laminated Object Manufacturing (LOM)
Vat photopolymerization (VP)	"an additive manufacturing process in which liquid photopolymer in a vat is selectively cured by light-activated polymerization"	Stereo Lithography Apparatus (SLA); Digital Light Processing (DLP)
Powder bed fusion (PBF)	"an additive manufacturing process in which thermal energy selectively fuses regions of a powder bed"	Selective Laser Sintering (SLS); Selective Laser Melting (SLM); Electron Beam Melting (EBM)
Directed energy deposition (DED)	"an additive manufacturing process in which focused thermal energy is used to fuse materials by melting as they are being deposited"	Direct Metal Deposition (DMD)

2.2.1 Selective Laser Sintering (SLS)

SLS is one of the most popular processes in AM that uses powder bed fusion technology. Researchers and practitioners have recently studied and discussed the pros and cons of the SLS process and its material requirements (Bourell, Watt, Leigh, & Fulcher, 2014; Despa & Gheorghe, 2011; Goodridge et al., 2012; Soe et al., 2013).

The schematic principle of the SLS process is illustrated in Figure 2-2. The SLS process works as follows: Initially, the feedstock powder is loaded into heated delivery chambers and the part bed temperature is heated to just below the melting temperature to minimize the required laser energy and resulting part distortion during cooling. Next, a thin layer of powder is spread over the build area and a computer-controlled laser scans over this area to heat and consolidate the powder particles in specified areas corresponding to a given cross-sectional slide of the CAD model. Unlike the full melting in the SLM process, this phase change uses partial melting (Guo & Leu, 2013). Next, the build platform (the platform on which the part is built) goes down a little by the predetermined layer thickness value (e.g., 0.1 millimeters) and another layer of powder is spread over the previously sintered layer. The procedure then repeats for all layers that involve the part until the whole part has been fabricated. Finally, the heaters are turned off and the part bed slowly cools. The powder in each layer that has not been fused by the laser remains in place to support the subsequent layers. Once the part and surrounding materials in the build chamber, i.e. the part cake, are cooled below the glass transition and oxidation temperatures, they are removed from the SLS machine. The part is then removed from the part cake and the loose powder is brushed off such that any unfused powder can be reused in future builds. Unlike some other AM processes, SLS does not require support structures because the part being fabricated is surrounded by unsintered powder.

Table 2-2 Pros and cons of SLS process

Advantages	Disadvantages
1. High strength and durability 2. Able to be produced without support structures (Polymer) 3. Recyclability of powder that has not been sintered 4. Variety of powders available for use	1. Must allow time for cooling 2. Cleaning required after production for powders that have not been sintered 3. The possibility of deformation due to various factors

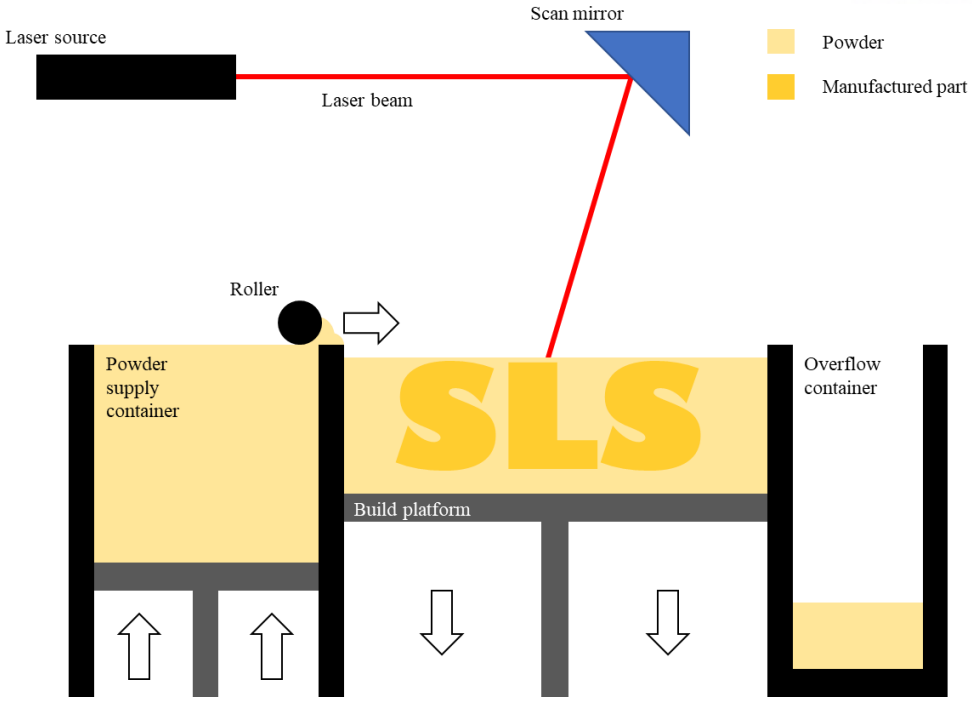

Figure 2-2 The schematic of Selective Laser Sintering

The pros and cons of SLS based 3D printers have been discussed in the literature (Bourell et al., 2014; Despa & Gheorghe, 2011; Han, 2013). As seen in Table 2-2, when compared to other 3DP methods, SLS technology can create products of superior mechanical properties with higher recyclability of materials. SLS is used extensively in the engineering industries, such as the automotive, mechanical, and aerospace sectors. In contrast to some other methods, SLS does not require support structures and can reuse powder that has not been sintered. It can also produce parts from a wide range of powder materials. On the other hand, some disadvantages have been noted involving the cooling time requirement, powder cleaning, and possible deformation. I address the deformation issue in this research. Other limitations to SLS include part size, manufacturing speed, and process control (Bourell et al., 2014).

2.2.2 Selective Laser Melting (SLM)

Recently, a lot of attention has been given to metal AM methods, among which SLM 3d printing is the most commonly used. Materials used in SLM include aluminum, titanium, and iron. The SLM process is very similar to the SLS process, as shown in Figure 2-3. The difference is that a high-power laser is used to dissolve metal powder to make each layer. Unlike SLS, SLM needs a support structure because it uses metal, so it is difficult to fabricate due to thermal deformation, and dross formation occurs on the surface of the overhang when fabricated without a support structure. To mitigate this dross formation phenomenon, a support structure is used (Sidambe, 2014; Zhang & Attar, 2016).

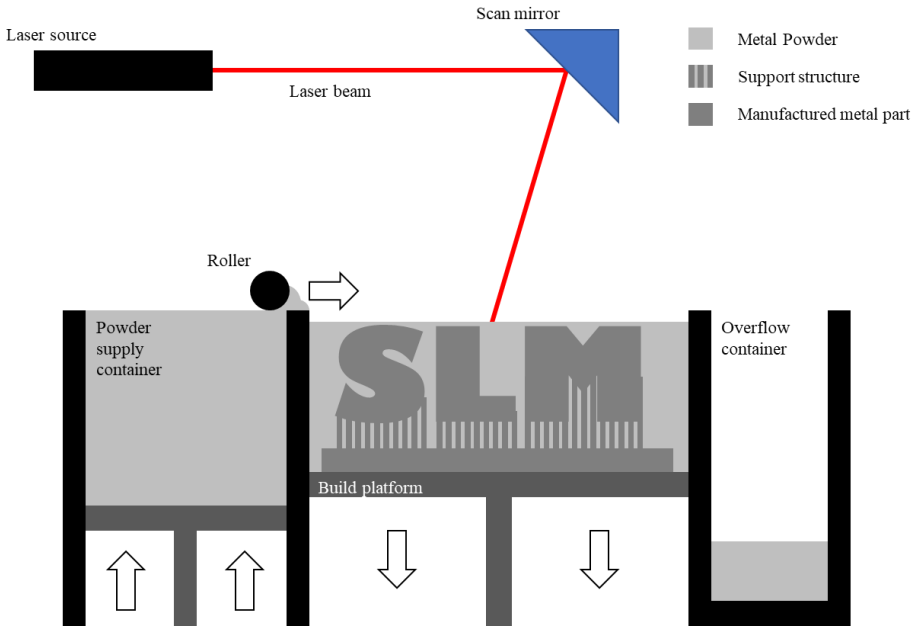

Figure 2-3 The schematic of Selective Laser Melting

Table 2-3 Pros and cons of the SLM process

Advantages	Disadvantages
1. High material properties and high density 2. Good dimensional accuracy 3. Recyclability of powder that has not been melted 4. Variety of powders available for use	1. Needs strong support structures 2. Needs post processing to cut the support structures

The advantages and disadvantages of SLM are shown in Table 2-3. SLM boasts high dimensional accuracy and is manufactured by melting, so it has excellent material properties and high density. However, as described above, a support structure is required for production, and therefore, work and tools for removing the support structure are required (Gao et al., 2015).

2.2.3 Electron Beam Melting (EBM)

EBM is similar to the other powder bed fusion-type AM technologies, as shown in Figure 2-4. However, there is a difference in using an electron beam instead of a laser, which makes it possible to manufacture narrower parts. The material is usually made of titanium or titanium alloy, so it has good rigidity and it is possible to make high-density parts through the EBM method, so it is also used in the medical field (Parthasarathy, Starly, Raman, & Christensen, 2010; Sidambe, 2014).

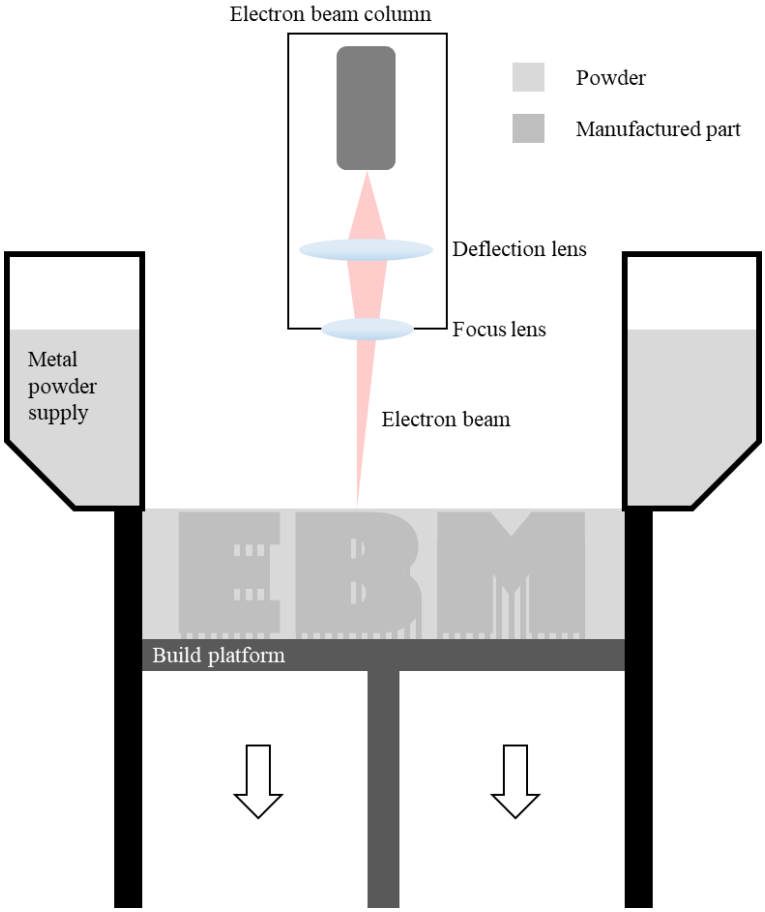

Figure 2-4 The schematic of Electron Beam Melting

The advantages and disadvantages of EBM are shown in Table 2-4. Through EBM, we can produce very high-density products with good mechanical properties. However, there are not many types of materials available, and x-ray rays are emitted at the time of manufacture. Also, post-processing is needed because of the rough surface finish and lack of precision. Nevertheless, the reasons for using EBM are that it is desirable to have less thermal deformation and a smaller support structure through material pre-heating compared to SLM (Alexandrea, 2017; Lindhe & Harrysson, 2000).

Table 2-4 Pros and cons of EBM process

Advantages	Disadvantages
1. High density and good mechanical properties 2. Smaller support structure 3. Reduce the deformation	1. Possible to use limited material 2. X-rays emitted 3. Need a lot of post-processing

2.3 Deformation problem in AM

A large amount of research is needed to solve the deformation problems that exist in products made using the SLS process. Several researchers have studied these deformation issues in 3DP parts (Bourell et al., 2014; Goodridge et al., 2012; Islam, Boswell, & Pramanik, 2013; Mercelis & Kruth, 2006; Soe et al., 2013; Wu, Brown, Kumar, Gallegos, & King, 2014). Bourell et al. point out that while insufficient heating can create porosity and particle coring, excessive heating can potentially degrade mechanical properties and dimensional accuracy in SLS (Bourell et al., 2014). Goodridge et al. suggest that surface finish, tolerances, and process repeatability issues have been overlooked and there is a definite need for greater consistency and systemic control in SLS (Goodridge et al., 2012). Wu et al. found that the peeling-up phenomenon at products' edges can also affect deformation issues (Wu et al., 2014).

Dimensional accuracy due to contraction and bending problems in the SLS type 3D printers have been researched in recent research (X. Chen, Zhou, & Li, 2010; Despa & Gheorghe, 2011; Hopkinson & Sercombe, 2008; Islam et al., 2013; Islam & Sacks, 2016; S. Singh et al., 2012; Soe, 2012; Wu et al., 2014). Dimensional accuracy of component parts denotes the degree of agreement between the produced dimensions and its design specification, which is the most critical feature to confirm dimensional repeatability of produced parts. Islam et al. researched the dimensional accuracy of parts fabricated by 3DP and discussed differences in linear dimensions and in hold diameter. They researched the effects of these errors on dimensional accuracy and found that size errors are associated with the 3DP process. In particular, the dimensions of the 3DP parts' x-y planes were found to always be shorter, while the heights in the z-direction were always longer than those of the original CAD file (Islam et al., 2013). Soe et al. reviewed the topic of the contraction of laser sintering in the z-direction and found that the contraction is non-linear and linked to thermal inconsistencies in the build chamber (Soe et al., 2013). Hopkinson and Sercombe researched the effect of sample height, sample position and build direction on the contraction during indirect SLS. The authors found that errors in the z-direction are more pronounced than in-plane (x and y) errors due to a phenomenon called z-growth, whereby the heat from the laser penetrates beyond the downward facing surface to bond unwanted particles (Hopkinson & Sercombe, 2008). Soe later investigated the factors affecting the bending of samples fabricated by SLS and found that the bending is dependent upon certain input parameters, including part processing parameters, the position of the part in the build chamber, part geometry, part orientation and the type of materials used (Soe, 2012). Recently, Islam and Sacks found that in contrast to a convex curvature issue widely reported in the literature, a concave curvature producing a flatness error can also be found. The authors hypothesize that the bending error is caused by layer interaction during and after the printing process (Islam & Sacks, 2016).

Bourell et al. suggest that the part bed temperature in the SLS process is one factor that affects dimensional accuracy. According to the authors, if the part bed temperature is too high, melting of low molecular weight regions can result in poor dimensional accuracy (Bourell et al., 2014). On the other hand, if the temperature is too low it can cause high part porosity. Residual stresses are one of the key issues in 3DP that impact deformation issues. Fernlund et al.'s study shows that the main factor of deformation comes from residual stresses in composite materials used in the heating process (Fernlund et al., 2003). Mercelis and Kruth studied the SLS and SLM processes and found that residual stresses impact dimensional stability, in which its magnitude and shape depend on diverse factors, such as material properties, sample height, the laser scanning strategy, and the heating conditions (Mercelis & Kruth, 2006). Despa and Gheorghe address the contraction issue and part accuracy. The authors suggest that contraction can be used as a measure to determine the accuracy of the products (Despa & Gheorghe, 2011). Goodridge et al. affirm that it is common practice to use a standard test piece to measure contraction. Then, a set of material scale factor can be applied to subsequent builds to compensate for contraction and to maintain dimensional accuracy. The authors note that while this is useful, applying scale factor ignores the fact that contraction is linked to geometry and build parameters, which are not just constant figures. They found that while increasing the scan speed and scan spacing may increase contraction, increasing the layer thickness, laser power, part bed temperature, and delay time may decrease contraction. Further, the part density, surface quality, and accuracy of the fabricated parts have all been found to increase with decreasing particle size (Goodridge et al., 2012).

Many 3DP manufacturers acknowledge deformation and dimensional inaccuracy issues and provide a general scale factor with the STL file to manage the volumetric contraction of printed samples. Thus, understanding how an STL file works is also important as it is widely used for AM technologies. The STL's surface is represented by an unordered list of triangles. A 3D surface normal is defined and followed by three coordinates that define the vertices of the triangle in three dimensions. Gardan suggests that the STL file creation process is inaccurate and the smaller the triangles are, the closer to reality it is. Additionally, the slicing process also introduces inaccuracy to the file because the algorithm replaces the continuous contour with discrete stair steps (Gardan, 2015; R. Singh & Singh, 2017). Chen et al. suggest that there is a lack of analytical models to predict deformation patterns in the literature and it has become difficult to conduct a dimensional calibration process for SLS 3D printers (X. Chen et al., 2010).

2.4 Analytic model of deformation in SLS or SLM

Many studies on powder bed fusion additive manufacturing, such as SLS and SLM, in which the powder is melted by a laser beam focus on formulating the deformation model to predict deformation using the constitutive equation. The most important thing when creating a deformation model is the strain value. Fundamentally, the strain consists of the following: elastic strain, vapor-elastic strain (or plastic strain) and thermal strain. In addition, there is also a sintering strain for the sintering process (Gasik & Zhang, 2000; Kim, Gillia, & Bouvard, 2003; C. Li, Liu, Fang, & Guo, 2017; Y. Li et al., 2018; J. Song, Gelin, Barrière, & Liu, 2006; Y. Song, Li, Zhou, Lai, & Ye, 2011).

Sintering strain is used in conventional manufacturing simulation rather than SLS. To date, there has not been enough sintering strain and stress-related research in SLS. Sintering stress is a stress generated between powder particles assuming a certain size and shape of powders. In this process, the strain rate is calculated through the viscosity of the material. Stress is calculated considering surface tension and powder size (Olevsky, 1998; Shinagawa, 1996)

The method using residual stress is widely used to predict the deformation of SLM. Residual stress is determined by elastic strain, plastic strain, and thermal strain. Basically, a residual stress calculation in laser welding is used to calculate the residual stress in the sample manufacturing process using SLM. At this time, the residual stress is absorbed by the laser, and the plastic deformation occurs as it expands, and as the heat cools, the sample shrinks. Currently, the upper part (laser irradiated part) contracts, so the bending deformation occurs. At this time, the thermal expansion coefficient and elastic modulus are the most important influences (Gasik & Zhang, 2000; Y. Li et al., 2018; Liu, Yang, & Wang, 2016; Mercelis & Kruth, 2006). On the other hand, the related research has not been conducted in SLS. In the case of SLS, nylon 12 is usually used as a material and SLS fabricates samples without a supporting structure and plate. In addition, in the case of nylon material, it is difficult to measure residual stress. Therefore, it is difficult to calculate the effect of self-weight of nylon material due to the small elastic modulus and the absence of the support plate compared with the SLM samples. In addition, the sintering method has a higher pore ratio than the melting method. Therefore, there are many difficulties in research due to high uncertainty.

2.5 Mechanical properties of AM

2.5.1 Energy density

In the case of additive manufacturing methods using lasers, there are various parameters that affect parts. To comprehensively determine the effect of these parameters, various studies have used the concept of energy density. The parameters included in energy density are slightly different in each paper, as shown in Table 2-5. Laser power and scan speed are common parameters. In addition, parameters such as hatching space, layer thickness, scan space, and spot diameter affect energy density. However, in the SLS 3D printer used in this experiment, we cannot control the scan speed, spot diameter, hatching space or scan space. In this study, the energy density was controlled using layer thickness and laser power (Gu & Shen, 2009; Nelson, 1993; Steen, 2010; Vandenbroucke & Kruth, 2007).

There are many existing studies on the relationship between energy density and density or porosity of production parts. As the energy density increases, the density of the 3D printed parts also increases (Caulfield, McHugh, & Lohfeld, 2007; Sing, Wiria, & Yeong, 2018; Tontowi & Childs, 2001). According to Beal, the energy density affects the shape of the sintered polymer part. Energy density and resulting material density are in direct proportion (Figure 2-5) (Beal, Paggi, Salmoria, & Lago, 2009). However, at very high energy densities, density tends to decrease (Caulfield et al., 2007).

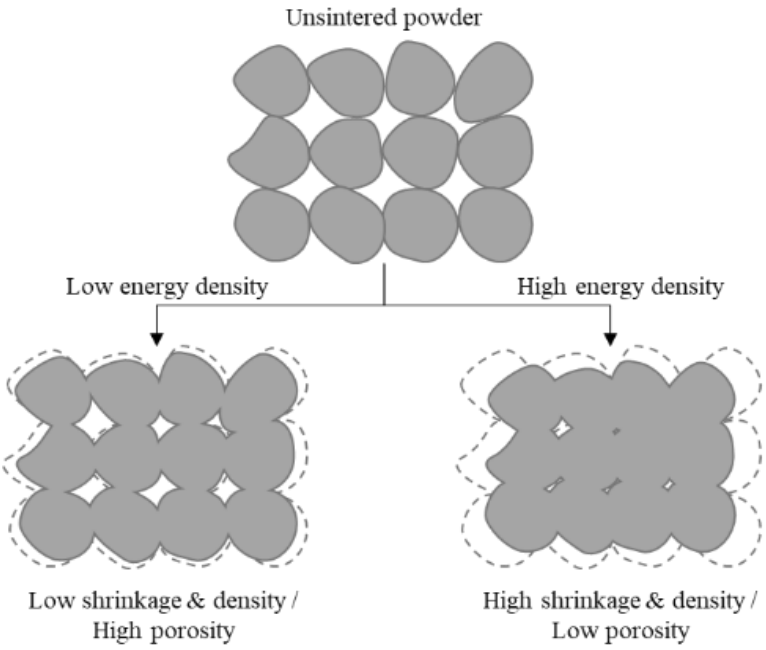

Figure 2-5 The relationship between energy density and porosity (Beal et al., 2009)

Table 2-5 Definition of Energy Density of each study

Author	Equation	Unit	Note
(Gu & Shen, 2009)	$ED = \frac{LP}{SS}$	J/mm	**2-1**
(Vandenbroucke & Kruth, 2007)	$ED = \frac{LP}{SS \times HS \times t}$	J/mm^3	**2-2**
(Nelson, 1993)	$ED = \frac{LP}{SS \times S}$	J/mm^2	**2-3**
(Steen, 2010)	$ED = \frac{LP}{SS \times d}$	J/mm^2	**2-4**

where:

- ED = *Energy density*
- LP = *Laser power*
- SS = *Scan speed*
- t = *Layer thickness*
- HS = *Hatch spacing*
- S = *Scan spacing*
- d = *Spot diameter*

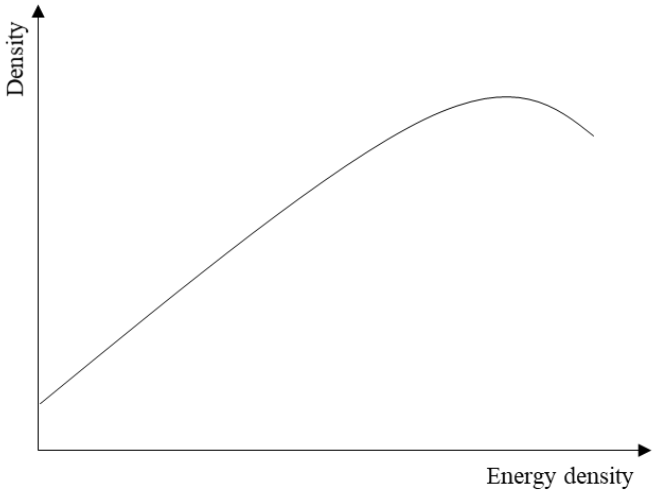

Figure 2-6 The graph of density according to energy density (Caulfield et al., 2007)

2.5.2 Elastic modulus

Some studies have investigated the relationship between porosity and temperature elastic modulus. Table 2-6 shows the elastic modulus results for studies related to porosity. Although there is a difference in the formula for each study, elastic modulus decreases as the porosity rate increases (German, 1984; L. J. Gibson & Ashby, 1999; Palchik, 1999; Sevostianov, Kováčik, & Simančík, 2006; J. Wang, 1984).

Table 2-6 The relationship between elastic modulus and porosity rate

Author	Equation	Note
(Sevostianov et al., 2006)	$E = E_f(1-P)^{\xi}$	**2-5**
(Palchik, 1999)	$E = \sigma_c \frac{1-P}{C_{Palchik}}$	**2-6**
(L. J. Gibson & Ashby, 1999)	$E = E_f C_{GibsonP}(1-P)^{k_{GibsonP}}$	**2-7**
(German, 1984)	$E = E_f(1-P)^{k_{German}}$	**2-8**
(J. Wang, 1984)	$E = E_f e^{-(C_{Wang1}P + C_{Wang2}P^2)}$	**2-9**

where:

- E = *Elastic modulus*
- E_f = *Elastic modulus of the fully dense material*
- P = *Porosity rate*
- ξ = *Parameter value which is calculated by the spheroid aspect ratio and Poisson ratio.*
- C = *Coefficient value*
- k = *Coefficient value*
- σ_c = *Uniaxial compressive strength*

The equations expressing the relationship between elastic modulus and temperature are shown in Table 2-7. At high temperatures, both formulas show a linear relationship between temperature and elastic modulus. Elastic modulus decreases with increasing temperature. Since the sintering process occurs near the glass transition temperature, it is assumed that the temperature and elastic modulus

have a linear relationship in this experiment (L. J. Gibson & Ashby, 1999; Wachtman, Tefft, Lam, & Apstein, 1961).

Table 2-7 The correlation between elastic modulus and temperature

Author	Equation	Note
(L. J. Gibson & Ashby, 1999)	$E = E_0(1 - C_{GibsonT}\frac{T}{T_m})$	**2-10**
(Wachtman et al., 1961)	$E = E_0 - C_{Wachtman}Te^{-\frac{T_0}{T}}$	**2-11**

where:

- E = *Elastic modulus*
- E_0 = *Elastic modulus at absolute zero*
- T = *Temperature*
- T_m = *The melting temperature*
- T_0 = *The specific temperature*
- C = *Coefficient value*

2.5.3 Properties nylon 12 samples fabricated by SLS

Elastic modulus equations for the properties of SLS nylon 12 samples were developed based on the density. Research on modulus and elongation at fracture point according to yield stress and energy density has also been conducted. From the results obtained, it is clear that the parts fabricated by the SLS process have elastic modulus inversely proportional to pore ratio and Poisson's ratio proportional to the energy density. In addition, it is worth noting that the elastic modulus and the Poisson's ratio of samples differ depending on the layout direction (Ramos-Grez, Amado-Becker, José Yañez, Vargas, & Gaete, 2008; Starr, Gornet, & Usher, 2011).

2.6 Compensation model in AM

Many methods of minimizing the distortion using the deformation compensation model through deformation prediction have been studied in AM (Huang, 2016; Huang et al., 2014; Huang et al., 2015; S. Jin et al., 2017; Luan & Huang, 2015; S. Song et al., 2014; Tong et al., 2003; Tong et al., 2008; A. Wang et al., 2017). With regard to AM, two general approaches to improve the accuracy of the process in question exist. While the first approach, error avoidance, seeks to remove the cause of an error (e.g., slicing technique improvement, support structure generation, tool path planning, process parameter tuning, or build orientation optimization); the second approach, error compensation, strives to cancel the effect of an error without removing the error source (Tong et al., 2003; Tong et al., 2008). Most previous research on AM accuracy improvement falls into the error avoidance category. However, even the best-tuned system still currently produces parts with systematic errors and error compensation is needed to further reduce errors.

Tong and colleagues propose a change to CAD design to compensate for contraction by using a polynomial regression model to analyze the contraction in the x, y, and z directions separately. The confounding effects of all errors of the stereolithography (SLA) and the fused deposition modeling (FDM) processes are mapped into a virtual parametric machine error model in their study (Tong et al., 2003; Tong et al., 2008). Studies into modifying support structures so as to mitigate bending deformation in SLM were already conducted by Liu et al. (Liu et al., 2016). Paul and colleagues proposed a method to estimate the error for metal powder based AM using thermal deformation and geometric models (Paul & Anand, 2015; Paul, Anand, & Gerner, 2014). Huang and colleagues have recently established a novel approach to modeling and predicting part deviations caused by contraction deformation and derive an optimal compensation plan to achieve dimensional accuracy using the polar coordinates system (r, ɵ, z) (Huang, 2016; Huang et al., 2014; Huang et al., 2015; Luan & Huang, 2015). They analyzed the in-plane (x and y) shape deformation and illustrated their approach for the cylindrical shapes in the SLA process (Huang et al., 2015). They extended their previous study to both polygon-shaped and arbitrary freeform shaped deviations in the SLA process(Huang et al., 2014; Luan & Huang, 2015). Based on the previous work in in-plane geometric deformation, Jin et al. extended the methodology to the out-of-plane (z) geometric error prediction for the SLA process (Y. Jin, Qin, & Huang, 2015). Huang then presented the minimum area deviation (MAD) and minimum volume deviation (MVD) criteria to define a compensation policy for 2D and 3D shape deformation for the SLA process, respectively (Huang, 2016). Besides the SLA process, some of them presented a strategy for error compensation in the FDM processes (S. Song et al., 2014; A. Wang et al., 2017) based on the model developed by Huang et al (Huang et al., 2015). Their model was then validated using circular plates.

2.7 Research on the deformation issue of traditional manufacturing

To date, many researchers have investigated the compensation and the calibration methods of traditional manufacturing and have proposed models to predict deformation patterns (T.-C. Chen, Chang, Hung, Lee, & Wang, 2016; Fernlund et al., 2003; Vyroubal, 2011; H. Wang & Huang, 2007). Fernlund et al. summarized existing compensation methods for bending deformation and explained the method of predicting and reducing bending deformation by using moment (Fernlund et al., 2003).

Casting also causes distortion in the contraction process. Jin et al. studied ceramic shell deformation. The types of deformation are largely divided into linear expansion and shrink and bending, and the causes are classified based on the types of deformation. In that study, roasting temperature and soaking time were used as operational displacements and the contraction lengths in the x and y directions were measured. As a result of the analysis of variance (ANOVA), each manipulated displacement had a significant effect, the roasting temperature had an especially great influence (S. Jin et al., 2017).

Wang et al. studied deformation and contraction in investment casting. Specifically, they studied ring-to-ring structure. Both inner and outer diameters contracted compared to the original. Wax pattern thickness was linear compared with the pattern thickness, meaning it will be possible to predict future deformation. Based on this, an appropriate tooling allowance can be set in the product design (Donghong Wang, Dong, Zhu, Shu, & Li, 2018).

Chen et al. suggest an anti-deformation compensation model based on the prediction of deformation of the curing process. The deformation is predicted by the curing process simulation and thermal stress analysis using Computer Aided Engineering (CAE) technology (X. Chen et al., 2010).

According to Jin et al. (S. Jin et al., 2017), AM part deformation can be divided into two parts; deformation by contraction, deformation by bending and I also follow this definition. In the case of the product manufactured using the SLS method, the difference of contraction rate according to part bed temperature and cooling time is similar to the casting method. However, this contraction rate can be easily mitigated by adjusting the scale factor in the instrument software. The bending deformation that occurs due to the difference in the manufacturing method is more severe. However, there is a lack of analytical models to predict the bending deformation patterns of AM products and it becomes difficult to conduct the dimensional compensation process for SLS 3D printers. Thus, I use this basis to develop a systematic dimensional compensation model in this research. This study aims to analyze the causes of AM part deformation; to provide a systematic compensation framework, and to validate it by studying the dimensional deformation patterns of 3D printed vehicle parts in the SLS platform.

2.8 Summary

The causes of deformation in SLS and SLM processes are diverse. The majority of the studies on the SLM process focused on the bending deformation of the residual stress produced during the heating and cooling process due to the laser heat. However, little work has been done regarding polymer printing using SLS, apparently due to the difficulty in measuring the residual stress of the polymer material. In comparison to SLM, SLS generates more pores, making it nearly impossible to apply the full density. Therefore, it is difficult to know the exact value because the physical properties, such as the thermal expansion coefficient and thermal conductivity elastic modulus, are affected by the pores (Zeng, Li, Fen-Chong, & Dangla, 2012). Hence, the SLM deformation model cannot be adapted to calculate the deformation in the SLS process. As a solution, a different approach to deformation is taken; one which uses the densification process. A thorough search of energy density concepts and elastic modulus deformation was done to investigate the density and the necessary elements for the deformation; the density increases with increasing energy density while elastic modulus decreases with increasing temperature or porosity rate. Based on this, an analysis of the cause of bending deformation and contraction will be discussed in Chapter 2.

As a result of investigating existing deformation minimization methods for improving the dimensional accuracy of samples, there are methods of producing deformations in a direction that minimizes deformation based on the predicted results and methods of making them larger as contraction. However, these methods are not suitable for solving the problem of bending deformation, which is the biggest problem in SLS fabrication samples. This is because there is a limit in reducing the bending deformation by changing the manufacturing orientation, and the bending deformation cannot be reduced by the shape size deformation. To solve this problem, I propose a compensation model which intensively mitigates the bending deformation in Chapters 3 and 4.

3. Analysis of deformation

Because of its design freedom, Additive Manufacturing (AM) has attracted attention from a variety of industries as a key manufacturing technology (Ko, Moon, & Hwang, 2015). Particularly in the automobile industry, AM has been studied for various applications such as building prototypes for assembly tests, tooling applications in production lines, and the direct manufacturing of actual parts. Selective Laser Sintering (SLS) is one of the most popular AM methods in the automotive industry because it allows the use of high-strength engineering plastics and unlimited design freedom due to it not needing support structures (Choi, 2014; Han, 2013). However, due to deformation problems in SLS, careful control of the production process and additional post-processing are frequently required to satisfy the dimensional requirements of the fabricated parts for industrial applications (Paul et al., 2014). For the effective control of the AM parameters during production, the operator is required to change parameters such as the laser power, the scanning speed, the layer thickness and the hatching distance, based on their experience.

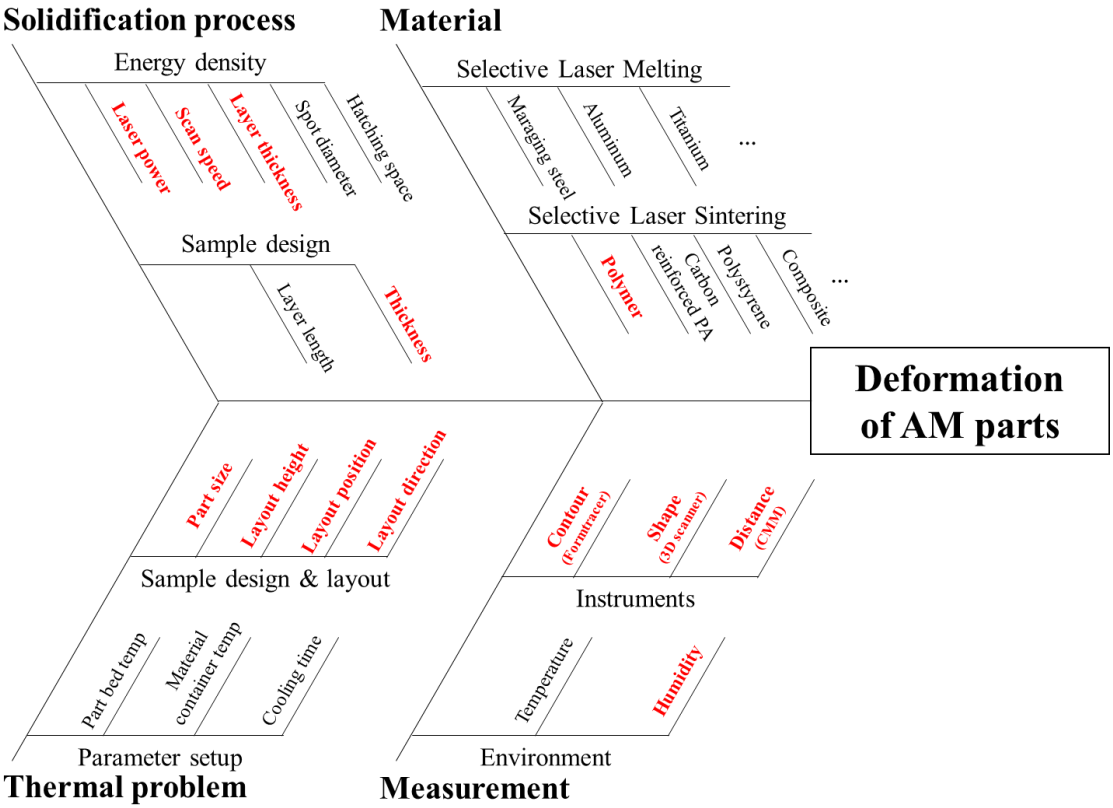

Figure 3-1 Fishbone diagram: input parameters affecting the deformation of AM parts

The factors affecting the deformation of the AM parts fabricated by the PBF method are summarized in Figure 3-1 based on Chapter 2. The elements to be covered in Chapter 3 are shown in red as follows. In Chapter 3, I describe the analysis of the deformation factors in SLS. The experiment

was divided into the deformation occurring in the sintering process, the deformation occurring in the cooling process and the deformation caused by the environment. During the sintering process, the powder-like material solidifies and the gap between the materials decreases. In this study, the sintering process is assumed to be a contraction process, and this contraction phenomenon is theoretically analyzed by using the Euler-Bernoulli beam equation. The related studies are described in Chapter 2. According to these previous studies, density is related to energy density. Thus, the degree of sample deformation was analyzed in relation to energy density-related parameters such as laser power, scan speed, and layer thickness. And, in cases where deformation occurred in the cooling process, the degree of deformation according to the shape and arrangement position was analyzed assuming that the temperature difference occurs depending on the shape of the sample or the arrangement position. I also analyzed the deformation factors of the part exposure environment after manufacturing. In brief, I confirm that size variation occurs due to humidity because SLS generates many unwanted pores during part production. In this study, the deformation of AM parts was analyzed by both bending deformation and contraction in the diameter or length of the product, unlike previous studies using just length and diameter (Hopkinson & Sercombe, 2008; Islam et al., 2013; Soe et al., 2013).

3.1 Theoretical analysis of deformation of AM parts (powder-bed fusion)

3.1.1 Theoretical analysis of deformation during the sintering process

As described in Section 2.4, energy density and density are in direct proportion. The contraction rate differs depending on energy density. To find the stress caused by this contraction phenomenon, the Hooke's law was used as in Eq. (3-1)(Beer, Jr. Johnston, DeWolf, & Mazurek, 2008).

$$\sigma_s = E(T, \rho)\epsilon_s \quad \textbf{3-1}$$

$$E_T(\rho) = C_T \times 1.192 \times 10^8 \times e^{3.116\times10^{-3}\rho} \quad \textbf{3-2}$$

$$SF_x(1 + \epsilon_{xs}) = 1 \quad \textbf{3-3}$$

where:

- *T = Temperature*
- σ_s *= Contraction stress*
- ϵ_s *= Strain of length by densification*
- ρ *= Density*
- *SF = Scale factor*
- C_T *= Compensation coefficient of temperature*

To find the stress value using Eq. (3-1), strain values and elastic modulus should be determined. For elastic modulus values, data from literature survey are used (Ramos-Grez et al., 2008). In addition, the contraction occurs at high temperatures in the sintering process. To compensate for the change in elastic modulus due to temperature, the elastic modulus is calculated using the C_T coefficient, as shown in Eq. (3-2). For the strain value in the x and y-directions, I used the scale factors of the 3D printer machine. The 3D printer device used in this experiment is sPro60 (SLS), and the scale factors in the x and y-directions are 3.32% and 3.324%. Eq. (3-3) calculates the x-direction strain using the scale factor in the x direction. When applying 3.32%, the strain in the x direction is -0.0318.

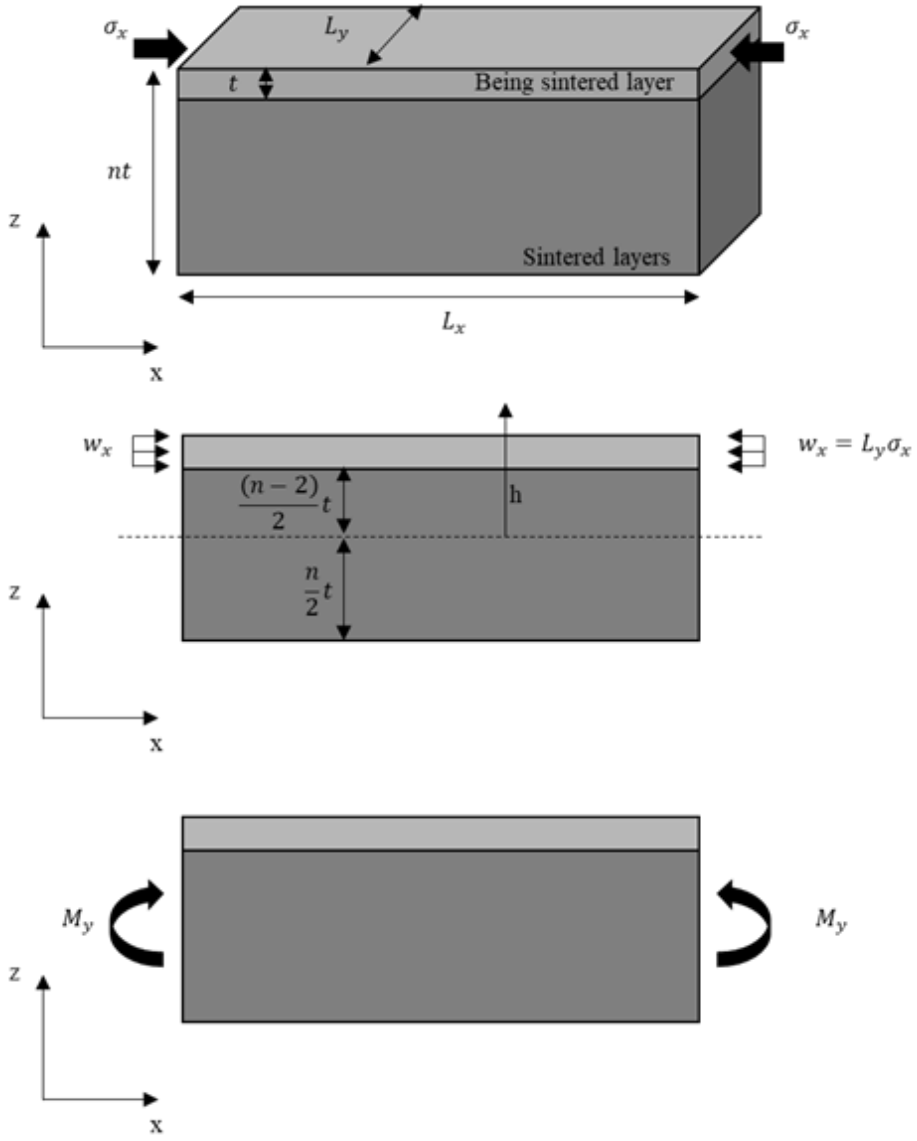

Figure 3-2 Bending moment calculation procedure through the densification process

Elastic modulus is affected by temperature and porosity rate as shown in Section 2.4. I used the sPro60 SLS machine for sintering during the densification process The temperature of the process chamber was adjusted to 174°C. The porosity rate, which affects the elastic modulus, can be obtained using the density of the material and the density of the powder and the part using Eq. (3-4). The density of the material means the density when there are no pores.

$$P(porosity\ \ rate) = 1 - \frac{\rho}{\rho_{fully\ \ dense}} \quad \textbf{3-4}$$

$$M_x = \int_0^{\frac{n}{2}t} w < h - \frac{(n-2)}{2}t >^0 h\, dh = \frac{n-1}{2}wt^2 = \frac{n-1}{2}L_y\sigma_x t^2 \quad \textbf{3-5}$$

The stress in each direction can be obtained by applying Eq. (3-2) and (3-3) to Eq. (3-1). The bending moment due to this stress can be obtained using Eq. (3-5). In the case of w in Eq. (3-5), only the layer in the densification process is applied as shown in Figure 3-2.

$$M_x = E_{part} I \frac{d^2 z}{dx^2} \quad \textbf{3-6}$$

$$z = \frac{M_x}{2E_{part} I_x} x^2 + \frac{C_1}{E_{part} I_x} x + \frac{C_2}{E_{part} I_x} \quad \textbf{3-7}$$

The bending moment obtained from Eq. (3-5) can be applied to the Euler-Bernoulli Beam equation (Eq. (3-6)) to calculate how much deformation appears, as shown in Eq. (3-7) (Beer et al., 2008). The porosity of a part can be obtained by applying the density of the part to Eq. (3-4). The part temperature is maintained at a building platform temperature of 160°C for the P770. Therefore, the sintered layers are calculated at 160°C.

$$I_{nx}(Inertia\ \ of\ \ x-bending\ \ moment\ \ at\ \ nth\ \ layer) = \frac{1}{12} L_y (nt)^3 \quad \textbf{3-8}$$

$$a_{nx} = \frac{M_{nx}}{2E_{part} I_{nx}} = \frac{n-1}{4E_{part} I_{nx}} L_y \sigma_x t^2 = \frac{3(n-1)}{E_{part} L_y n^3 t^3} L_y \sigma_x t^2 = \frac{3(n-1)\sigma_x}{E_{part} n^3 t} \quad \textbf{3-9}$$

The value of the moment of inertia can be obtained using Eq. (3-8) for a rectangular parallelepiped shape. If I substitute it with the value of the bending moment in the coefficient value of Eq. (3-7), the coefficient value can be obtained as in Eq. (3-9).

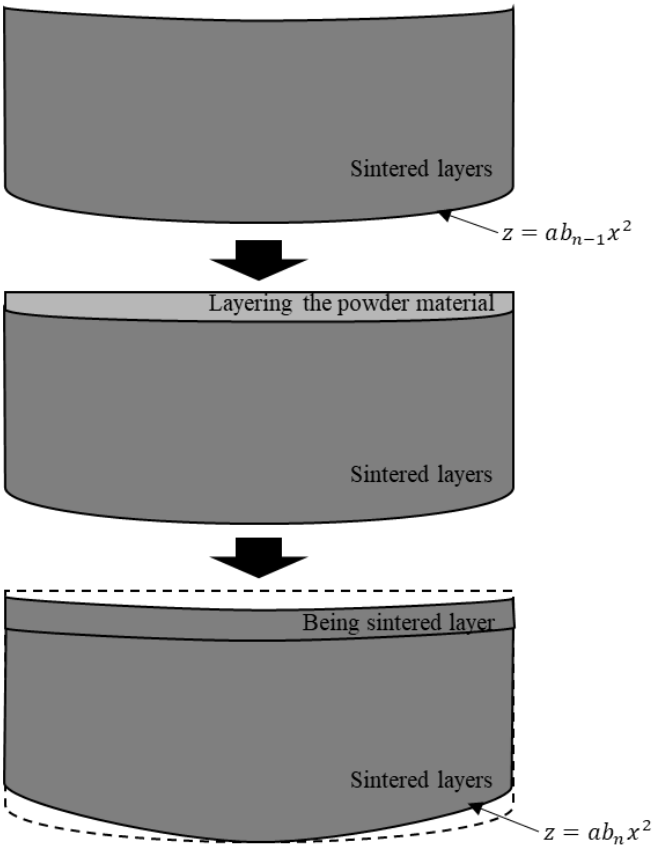

Figure 3-3 Bending deformation in the multi-layer situation

Figure 3-3 shows the phenomenon that occurs in a multi-layer part using the deformations that appear in the single layer densification process described above. The reason for using only the coefficient of x^2 in Figure 3-3 is that the curvature of the banding can be obtained by EI / M.[28] The degree of bending of the upper and lower surface differ depending on the manufacturing method. In the case of the lower surface, additional deformation occurs as a layer is added as shown in Eq. (3-10). In addition, to compensate for the temperature difference due to the position of the part placement, the instrument calibration function K is added. The function K is different for each 3D printer device. In the case of sPro60 used in this experiment, the degree of deformation varies depending on the height of the part arrangement, and a function related to the arrangement height is used.

$$ab_{nx} = a_{nx} + ab_{(n-1)x} = \sum_{i=1}^{n} a_{ix} = \sum_{i=1}^{n} \frac{3(i-1)\sigma_x}{E_{part} i^3 t} \qquad \textbf{3-10}$$

The coefficient values of x^2 can be measured using a quadratic regression model using surface height values. Therefore, the degree of bending deformation in the mathematical modeling process is represented by the coefficient value of x^2 instead of the curvature.

3.1.2 Experiment plan

According to the mathematical model (Eq. (3-10)), deformation occurs through the solidification process. In particular, as the difference in density between the powder and the part increases, the deformation of the 3DP part increases. Therefore, I tried to verify the difference of strain according to energy density. The properties of this test are shown in Table 3-1. The material is PA2200. The scan space is 0.15 mm; the laser spot is 0.5 mm, and the scan speed is 6000mm/s. Figure 3-4 shows the sample designs used in this experiment. The width of the samples is 10mm, the length is 120mm and the height is designed to be 5mm, 10mm, and 15mm respectively.

Table 3-1 Verification test properties

Parameters	Experimental Setting
Machine	sPro60 (3Dsystems)
Material	PA2200
scan spacing	0.15mm
Process chamber	174℃
Building platform	160℃
Spot diameter	0.5mm
Scan speed	6000mm/s

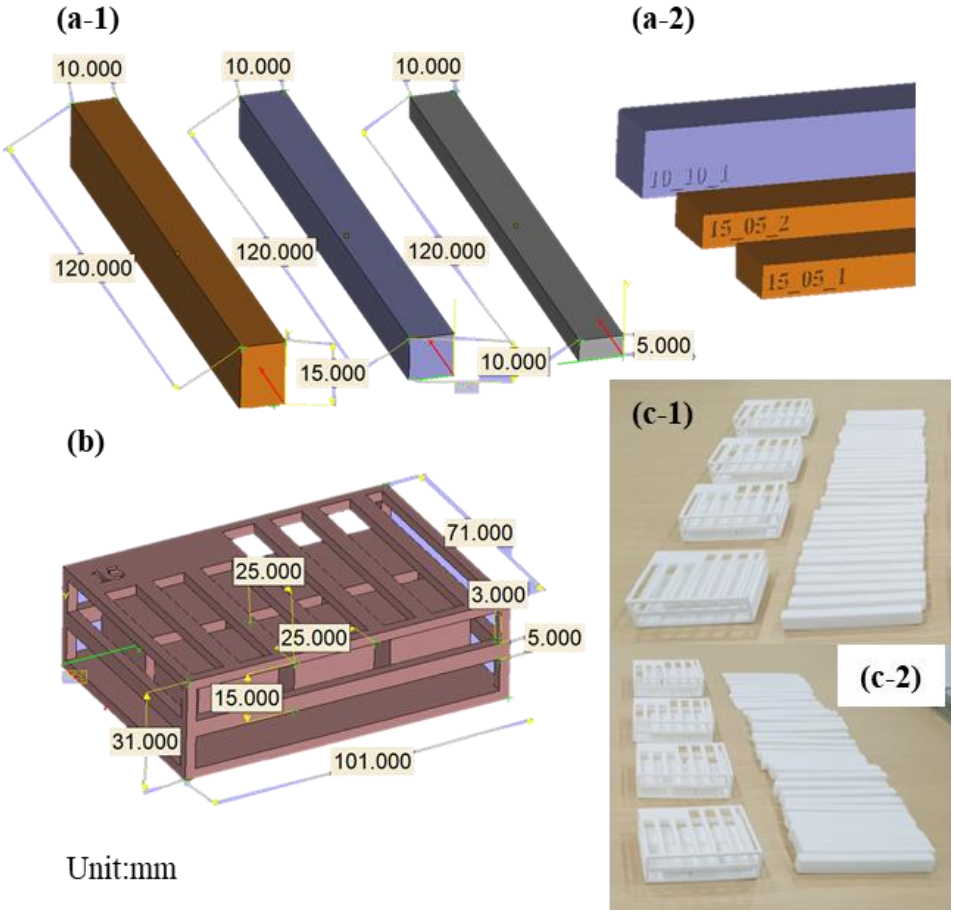

Figure 3-4 (a-1): Verification samples design for measuring the bending deformation (a-2): Labeling of the bending deformation samples (b): Verification sample designs for measuring the density of each energy density (c-1): Samples of 0.15mm layer thickness (c-2): Sample of 0.1mm layer thickness

As noted in Chapter 2, the parameters used to calculate energy density are different for each study, but all of them use the laser power and layer thickness parameters. In addition, according to the mathematical model of Section 3.1, the part thickness also affects the deformation, so it is added as a manipulation variation. Therefore, the manipulation variations used in this experiment are part thickness, laser power, and layer thickness. Four pieces were fabricated for each operation variation value; two of them were arranged at the base, the others at 40mm. A total of 72 samples were fabricated. The bottom surface of the fabricated samples was measured using Formtracer® equipment (Mitutoyo 2015). Second-order regression analysis was performed on the measured surface tracing data. The second-order coefficient of the second-order regression model is the value of the bending curvature, which is used to analyze the correlation between the energy density and the degree of bending.

Table 3-2 Moderator variable

Batch height (mm)	Layer thickness (mm)	Laser power (W)	Part thickness (mm)
0	0.1	8	5
			10
			15
		10	5
			10
			15
		15	5
			10
			15
	0.15	10	5
			10
			15
		15	5
			10
			15
		25	5
			10
			15
40	0.1	8	5
			10
			15
		10	5
			10
			15
		15	5
			10
			15
	0.15	10	5
			10
			15
		15	5
			10
			15
		25	5
			10
			15

3.1.3 Verification result

The ANOVA results for density and each manipulated displacement are shown in Table 3-3. Layer thickness and laser power are closely related to density. These values are variables used in energy density calculations. The relationship between energy density and apparent density is shown in Figure 3-5. As can be seen, the density increases with increasing energy density, which is similar to that seen in Figure 2-6. The energy density was calculated using laser power, scan speed, hatch space, and layer thickness, as shown in Eq. (3-11). In addition, I confirmed that there is a significant influence on the production layout height. From looking at the results, it appears that the cooling rate differs from the other positions because it is the uppermost part in the cooling process, not the sintering process.

$$ED = \frac{LP}{SS \times HS \times t} \quad \textbf{3-11}$$

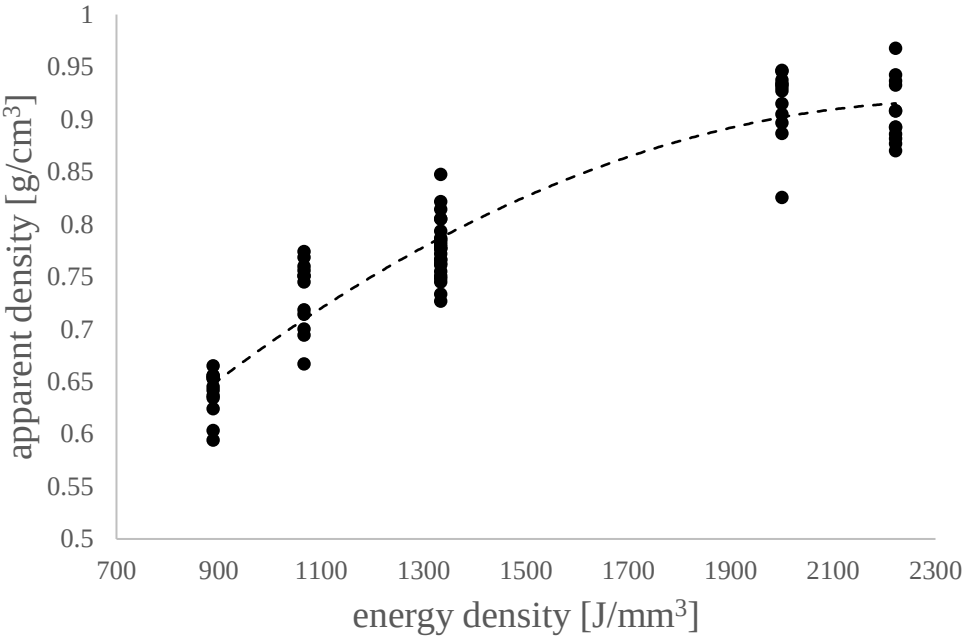

Figure 3-5 The relationship between energy density and apparent density

Table 3-3 ANOVA result of apparent density

Source	*DF*	*Adj SS*	*Adj MS*	*F-Value*	*P-Value*
Layer thickness (t)	**1**	**0.296844**	**0.296844**	**518.82**	**0.000**
Laser Power (LP)	**1**	**0.171502**	**0.171502**	**299.75**	**0.000**
Sample thickness (T)	2	0.001166	0.000583	1.02	0.370
Height of layout (h)	**1**	**0.002814**	**0.002814**	**4.92**	**0.032**
Error	42	0.02403	0.000572		
Lack-of-Fit	18	0.011192	0.000622	1.16	0.36
Pure Error	24	0.012838	0.000535		
Total	47	0.496357			

R-sq: 95.16% R-sq(adj): 94.58% R-sq(pred): 93.68%

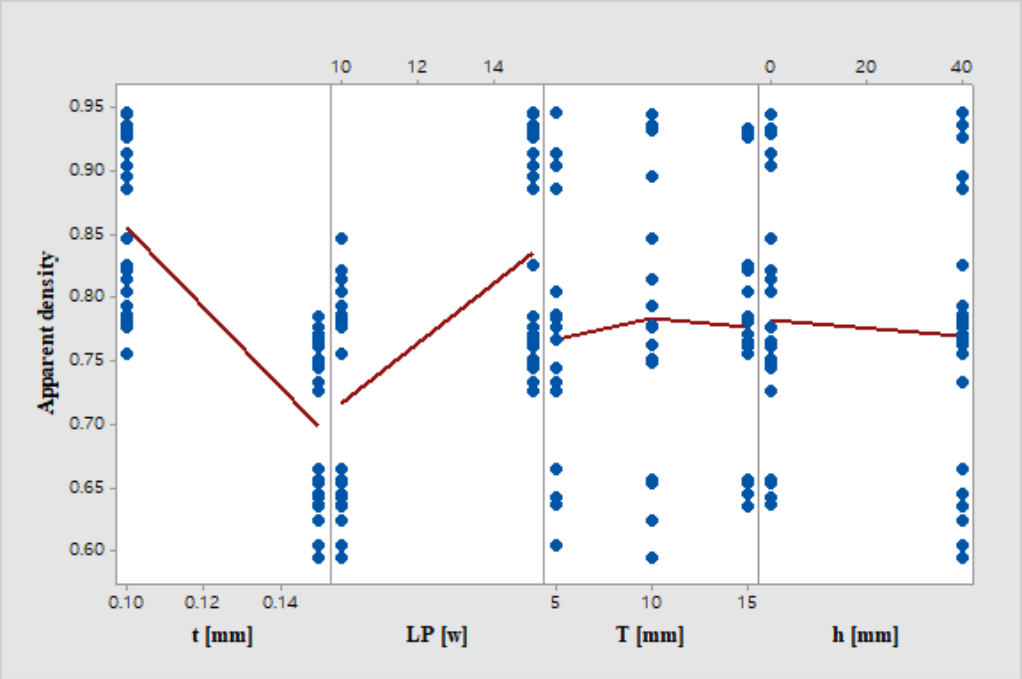

Figure 3-6 The plot of the apparent density of 3D printed part for each parameter

Table 3-4 shows the results of the ANOVA analysis for the degree of part deformation. Figure 3-7 is a graph showing the degree of deformation for each parameter. Table 3-4 and Figure 3-7 show that the layer thickness, the thickness of the part, and the height of the part placement are related to the degree of 3D printed part deformation. However, it is difficult to find a significant correlation between the laser power and the degree of deformation. Laser power increases the density of the part as well as the increase in elastic modulus, which cancel each other out. Thus, the laser power is not a variable that has a significant effect. In addition, as shown in Figure 3-8 and Table 3-4, in the case of the bending deformation, the effect of the interaction is significant as well as the effect of the single parameter. This is because the cause of the bending transformation is complicated.

Table 3-4 ANOVA result of bending deformation (x100000)

Source	*DF*	*Adj SS*	*Adj MS*	*F-Value*	*P-Value*
Layer thickness (t)	**1**	74.25	74.25	**12.25**	**0.001**
Laser power (LP)	1	4.14	4.14	0.68	0.414
Sample Thickness (T)	**2**	64.54	32.27	**5.33**	**0.010**
Height of layout (h)	**1**	1590.45	1590.45	**262.48**	**0.000**
*t*LP*	1	14.41	14.41	2.38	0.132
t*h	**1**	137.03	137.03	**22.61**	**0.000**
LP*T	**2**	41.02	20.51	**3.38**	**0.046**
*LP*h*	1	7.92	7.92	1.31	0.261
T*h	**2**	85.06	42.53	**7.02**	**0.003**
t*LP*h	**1**	113.16	113.16	**18.68**	**0.000**
Error	34	206.02	6.06		
Lack-of-Fit	10	71.65	7.16	1.28	0.296
Pure Error	24	134.38	5.6		
Total	47	2337.99			

R-sq: 91.19% R-sq(adj): 87.82% R-sq(pred): 82.44%

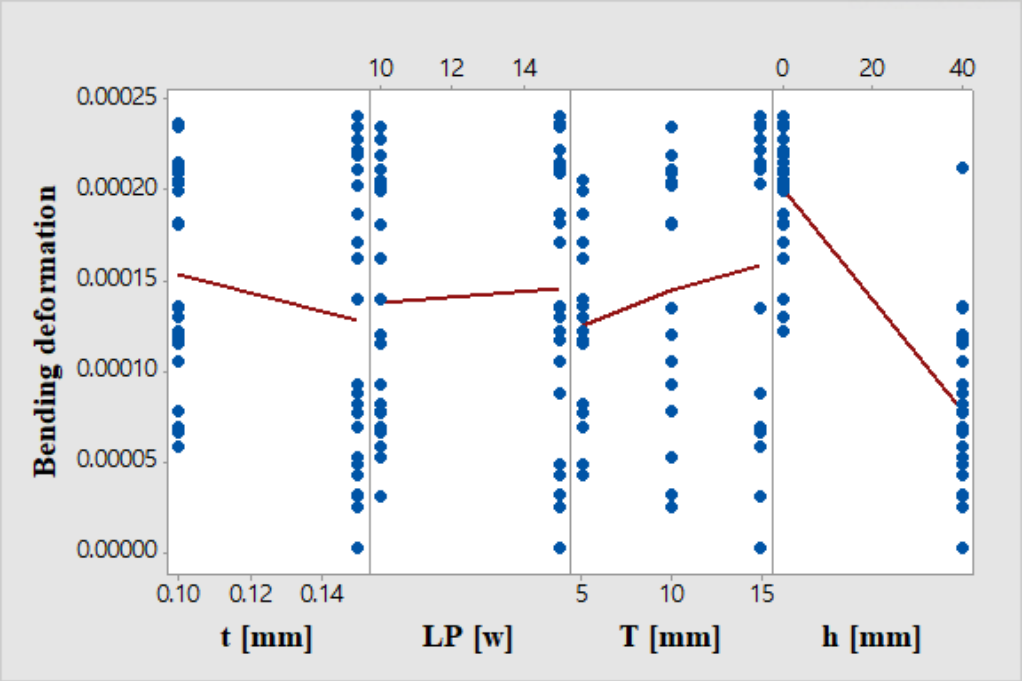

Figure 3-7 The plot of deformation of 3D printed part for each parameter

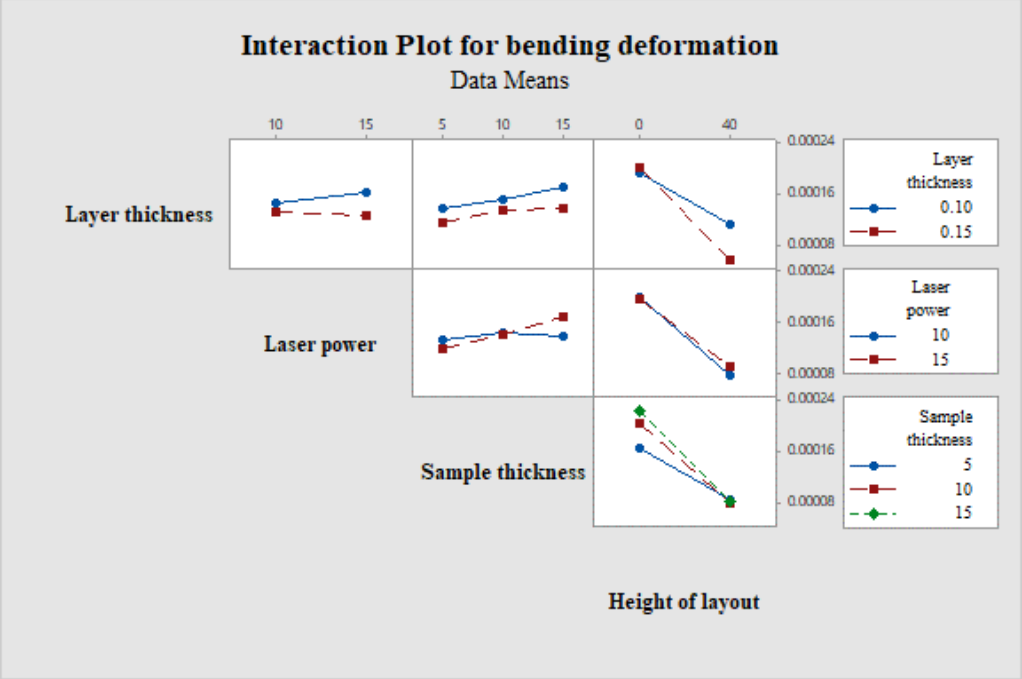

Figure 3-8 The interaction plot for bending deformation

The flow of analytic model of deformation is as Figure 3-9. First, the coefficient value was obtained according to the height of layout and the stress coefficient value was generated in the sintering phenomenon from the bending deformation data. And density value was obtained through density according to energy density. Using these values, I predicted the bending deformation and compared

with actual data. As a result, it can be confirmed that the actual data values were similar with predictive value.

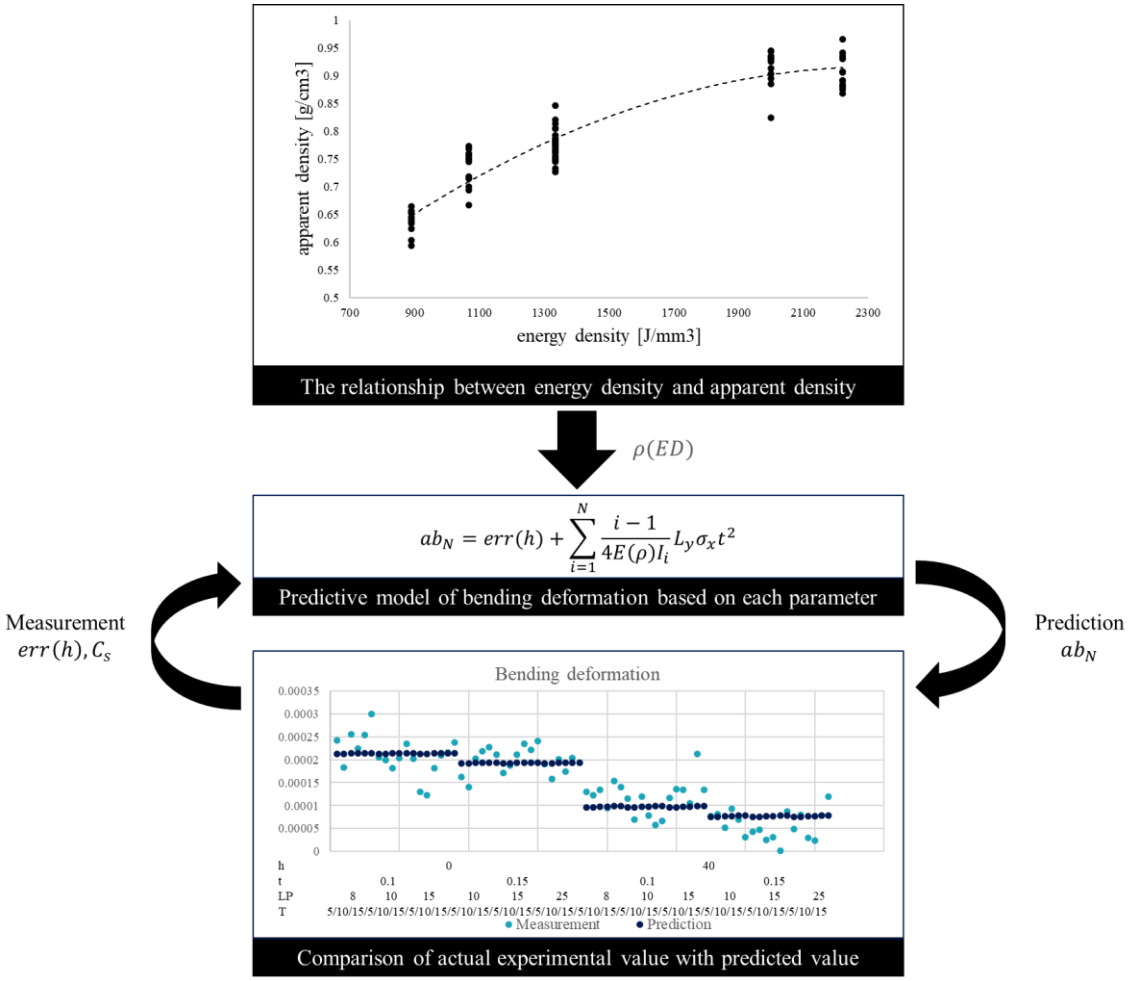

Figure 3-9 The flow of analytic model of deformation

3.2 Experimental analysis of deformation in AM parts

According to the existing studies described in Chpater2, the cause of deformation of AM samples is thermal deformation and residual stress. These problems are difficult to approach theoretically. Especially in the case of thermal deformation, temperature control method and thermal distribution are different for each AM machine, and the deformation pattern and degree of deformation are different for each AM machine. In particular, the time required for cooling and the distance from the heat source differs depending on the design of each AM machine. In this study, the bending deformation and the length contraction experiment were performed according to the manufacturing layout and sample design.

3.2.1 Analysis results of contraction patterns

There are many studies on the degree of contraction compared to thermal distribution and machine setup parameters, such as laser power or layer thickness and energy density, as described in Chapter 2. In addition, there are many studies on the direction of sample placement. However, the number of studies on the difference in the contraction rate according to the sample shape and layout height is insufficient. Therefore, I tried to investigate this in this study. The reason for this lack of research is that 3D printers generally require support structures except for SLS, so no other part is placed above another part. In SLS, however, no support structure is required, and another part can be placed above the first part to fabricate many parts in one layout. Currently, this research is insufficient, so it is difficult to fabricate a large number of parts in one layout. To analyze the contraction rate due to the production layout height and the part height, I designed a sample as shown in Figure 3-10. This experiment was designed as shown in Table 3-5.

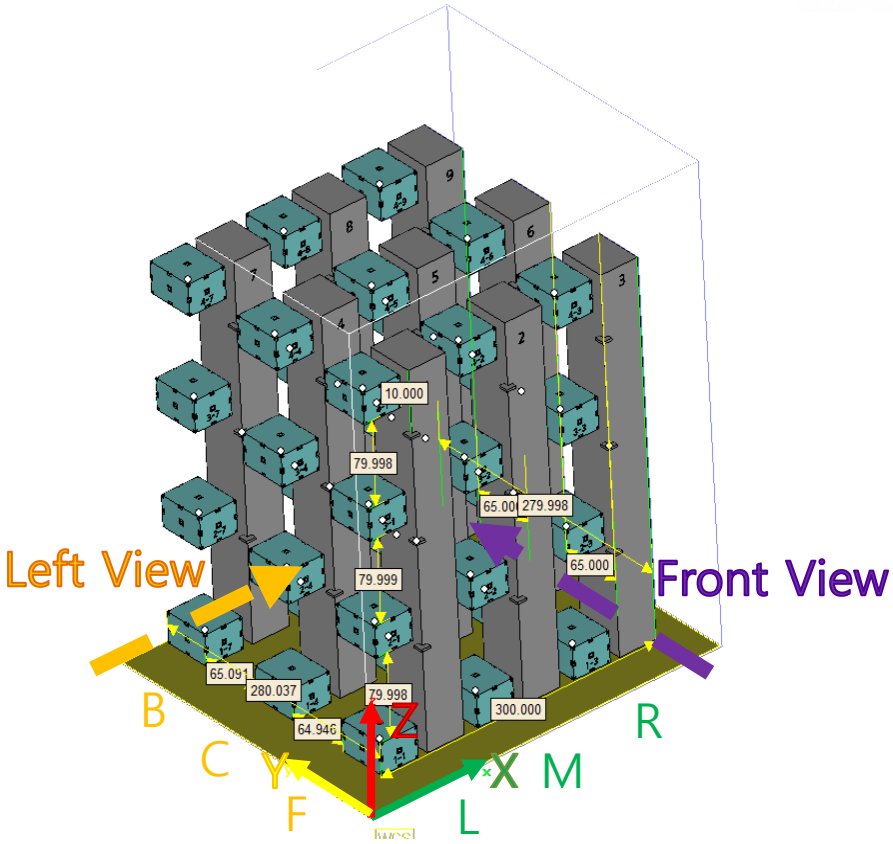

Figure 3-10 The layout of contraction rate test

Table 3-5 Experiment setup

Parameters	Experimental Setting
Machine	sPro60 (3D systems)
Layer thickness	0.1 mm
Laser power	
Inner side	10 W; for part building
Outer side	4 W; for curing
Laser scan speed	6 m/s
Build chamber temperature	171 – 174 degrees Celsius (℃)
Material	Duraform PA (Plastic/ PA12)
Sample size	
Long	40mm * 50mm * 330mm
Short	40mm * 50mm * 30mm

The measurement results were as follows. In the case of the length of the x-direction, the ANOVA result is shown by Table 3-6. The CAD data value of x-length is 40 mm. The factors with significant effect are the y-axis position and measurement points of the sample. The samples closer to the

window of sPro60 are longer, and the samples far from the window of sPro60 are shorter. The closer the measurement position of each sample is to the glass of sPro60, the longer the measurement data is. According to the measurement height of the sample, the central part is shorter and the end part is longer. The shape of the sample is in the form of an hourglass (Figure 3-11).

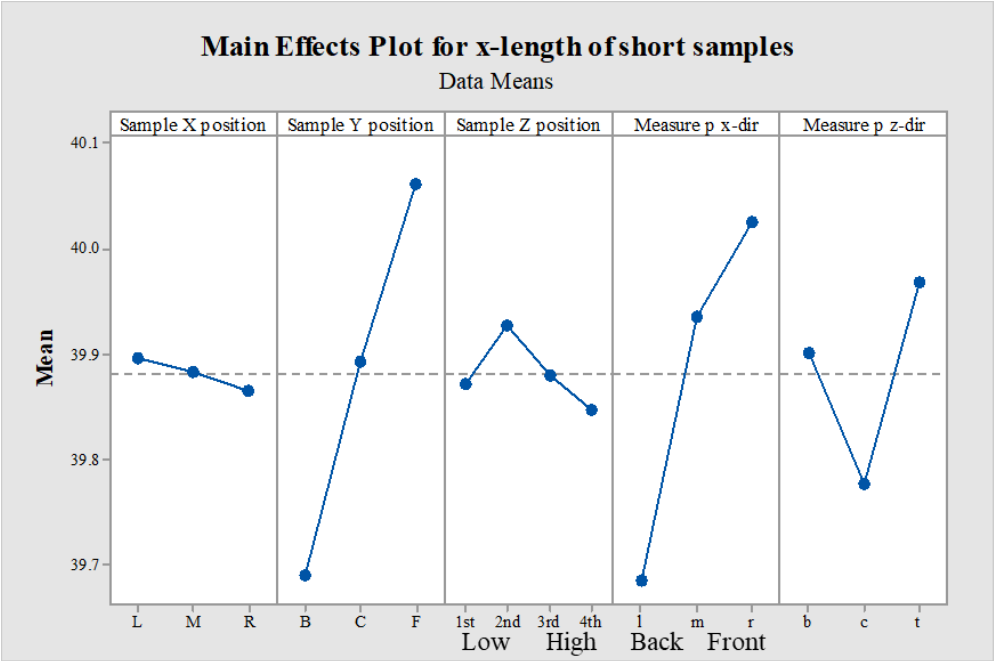

Figure 3-11 Main effects plot for x-length of short samples

Table 3-6 ANOVA result of x-length of short samples

Source	*DF*	*Adj SS*	*Adj MS*	*F-Value*	*P-Value*
Sample X position	2	0.0557	0.02785	0.62	0.538
Sample Y position	2	7.4558	3.7279	83.13	0
Sample Z position	3	0.2755	0.09182	2.05	0.107
Measurement point x direction	2	6.7418	3.37088	75.17	0
Measurement point z direction	2	2.0492	1.02462	22.85	0
Error	312	13.9911	0.04484		
Total	323	30.5691			

R-sq: 54.23% R-sq(adj): 52.62% R-sq(pred): 50.64%

In the case of the length of the y-direction, the ANOVA result is shown by Table 3-7. The CAD data value of x-length is 50 mm. The y-length results are generally similar to the x-length results. However,

there is a significant difference depending on the arrangement of x-position, and the middle portion is longer in the same layer. Results tend to be shorter overall compared to the CAD data (Figure 3-12).

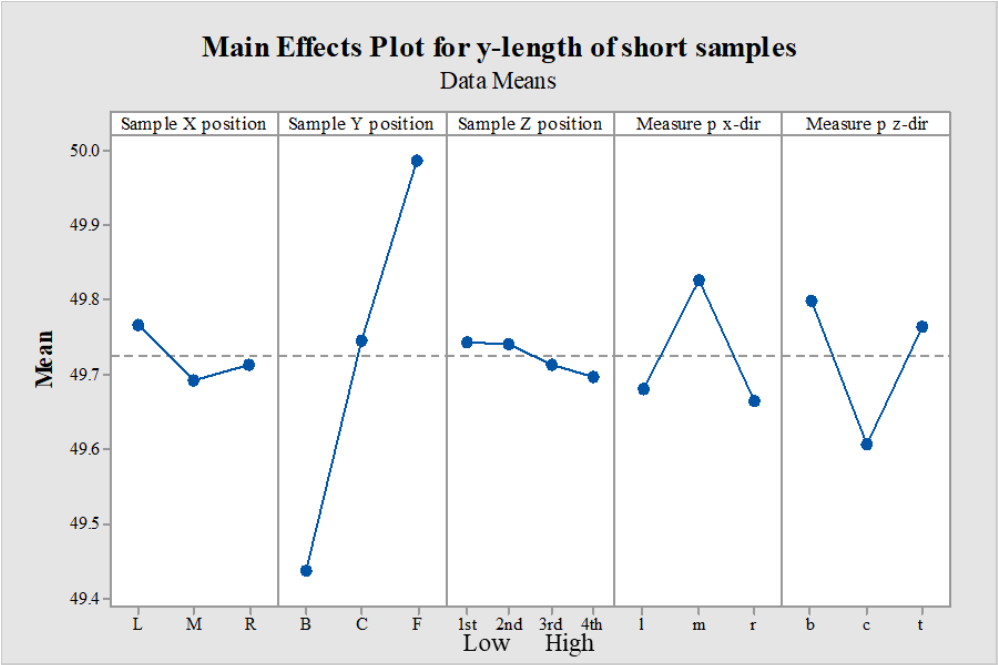

Figure 3-12 Main effects plot for y-length of short samples

Table 3-7 ANOVA result of y-length of short samples

Source	*DF*	*Adj SS*	*Adj MS*	*F-Value*	*P-Value*
Sample X position	2	0.3056	0.15278	5.96	0.003
Sample Y position	2	16.4837	8.24183	321.65	0
Sample Z position	3	0.1295	0.04316	1.68	0.17
Measurement point x direction	2	1.7447	0.87236	34.05	0
Measurement point z direction	2	2.2984	1.14921	44.85	0
Error	312	7.9945	0.02562		
Total	323	28.9564			

R-sq: 72.39% R-sq(adj): 71.42% R-sq(pred): 70.23%

In the case of the length of the z-direction, the ANOVA result is shown by Table 3-8. The CAD data value of x-length is 30 mm. Factors with significant effects are the sample y- and z-position and measurement points of the sample. As with the x-length and y-length results, the samples closer to the window of sPro60 are longer, and the samples far from the window of sPro60 are shorter. In addition, the longer the z-length is placed in the upper part, the shorter it is arranged in the lower part. The

results of the measurement points are equally concave in the middle, which is the result of bending deformation (Figure 3-13).

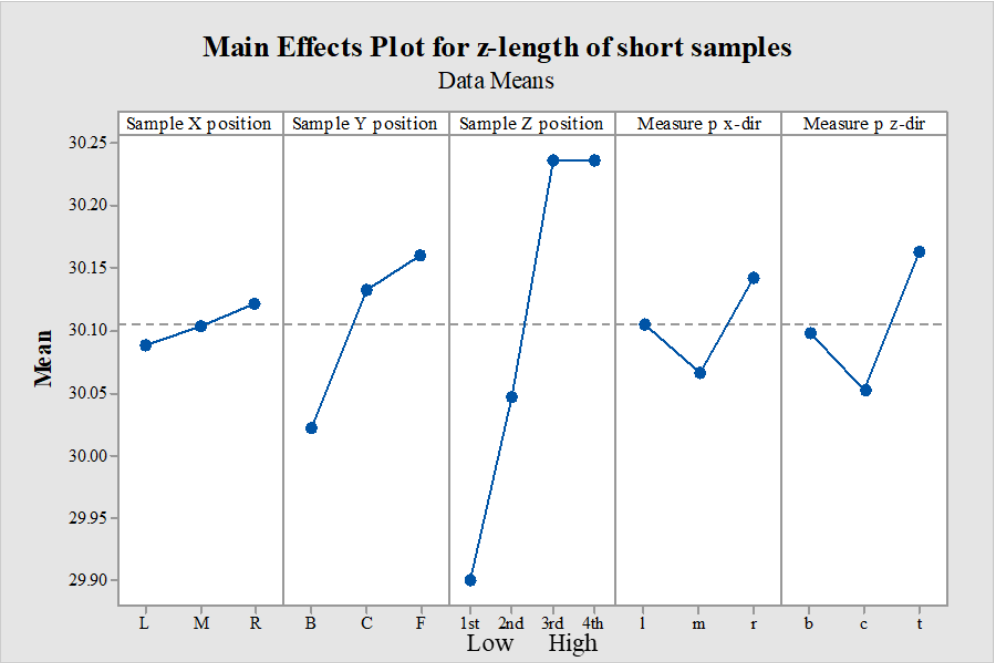

Figure 3-13 Main effects plot for z-length of short samples

Table 3-8 ANOVA result of y-length of short samples

Source	*DF*	*Adj SS*	*Adj MS*	*F-Value*	*P-Value*
Sample X position	2	0.0583	0.02913	1.18	0.309
Sample Y position	2	1.1617	0.58084	23.48	0
Sample Z position	3	6.5113	2.17042	87.73	0
Measurement point x direction	2	0.3151	0.15755	6.37	0.002
Measurement point z direction	2	0.6778	0.3389	13.7	0
Error	312	7.7187	0.02474		
Total	323	16.4428			

R-sq: 53.06% R-sq(adj): 51.40% R-sq(pred): 49.38%

In the case of the long samples, the ANOVA result is shown in Table 3-8 and Table 3-9. The CAD data value of x-length is 40 mm and the CAD data value of y-length is 50mm. The results of the long sample showed a significant influence on the position of the y-axis similar to the results of the short sample, and the tendency was also the same. And the effect on the measurement result according to

the measurement position was similar. However, the measurement results for height were short at both ends (Figure 3-14, Figure 3-15).

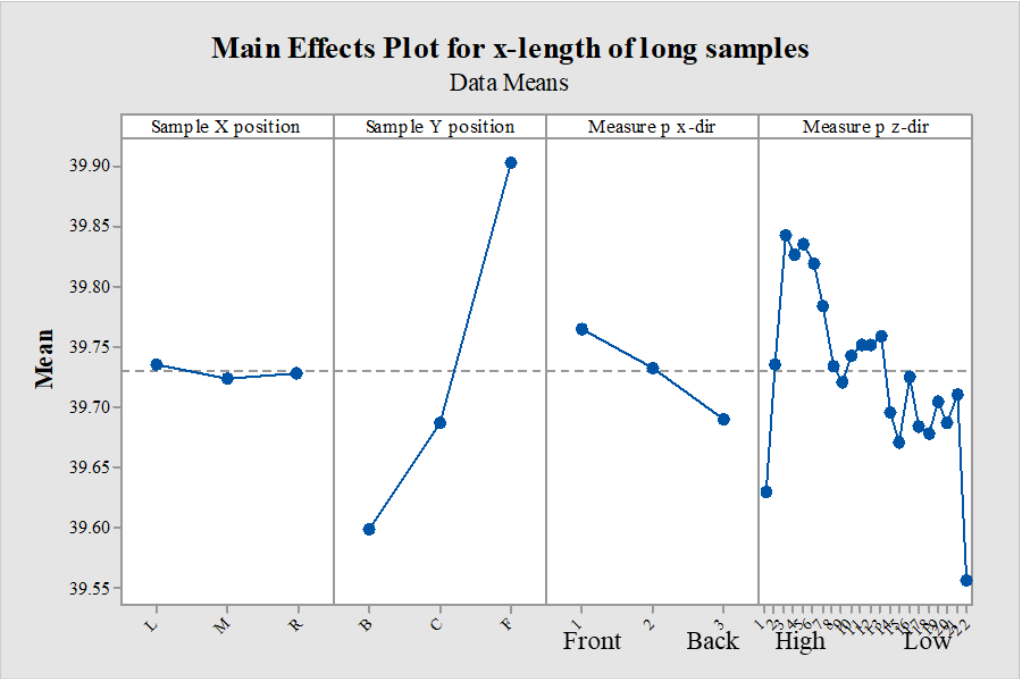

Figure 3-14 Main effects plot for x-length of long samples

Table 3-9 ANOVA result of x-length of long samples

Source	*DF*	*Adj SS*	*Adj MS*	*F-Value*	*P-Value*
Sample X position	2	0.0127	0.00633	0.37	0.694
Sample Y position	2	9.6597	4.82987	279.32	0
Measurement point x direction	2	0.559	0.27952	16.17	0
Measurement point z direction	21	2.6506	0.12622	7.3	0
Error	566	9.7869	0.01729		
Total	593	22.6689			

R-sq: 56.83% R-sq(adj): 54.77% R-sq(pred): 52.45%

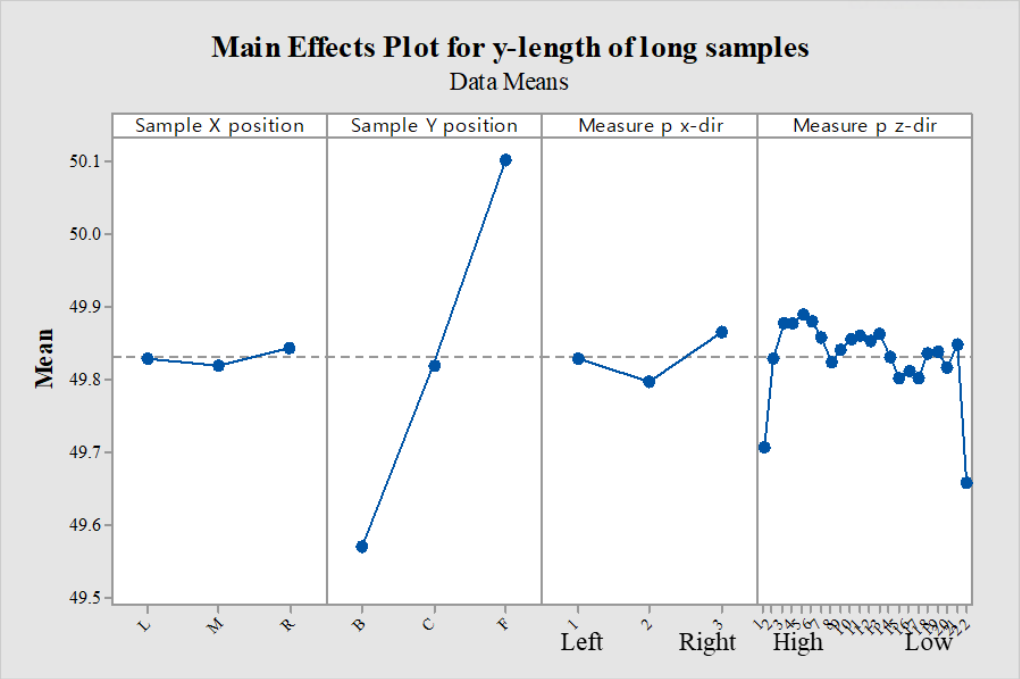

Figure 3-15 Main effects plot for y-length of long samples

Table 3-10 ANOVA result of y-length of long samples

Source	*DF*	*Adj SS*	*Adj MS*	*F-Value*	*P-Value*
Sample X position	2	0.0651	0.0326	3.49	0.031
Sample Y position	2	28.1916	14.0958	1511.47	0
Measurement point x direction	2	0.4375	0.2188	23.46	0
Measurement point z direction	21	1.6744	0.0797	8.55	0
Error	566	5.2785	0.0093		
Total	593	35.6471			

R-sq: 85.19% R-sq(adj): 84.49% R-sq(pred): 83.69%

All samples were strongly influenced by the y-axis location, and the closer to the window of sPro60 the more likely the samples would be longer. This phenomenon is expected to occur as the part is closer to the window and less contraction due to the lower temperature than the opposite direction. And all samples tended to be shorter as they were placed at the bottom. It is confirmed that the error occurred in the calibration process of the scale factor value.

3.2.2 Analysis results of bending deformation patterns by layout positions

The part sample was constructed in the x, y, and z-axes, as shown in Figure 3-15, (a), while Figure 3-16 (b) shows the part samples in different locations in the part bed to observe the deformation pattern of the samples based on their location. By using Magics developed by Materialise Inc., a part bed size applicable to the SLS machine (sPro60 SD) was chosen. The Magics software can handle the STL CAD model and can allocate samples automatically based on the 3D printer type. Four samples at the lower locations (L) (i.e., (L, 1), (L, 2), (L, 3), and (L, 4)) and another four at the upper locations (U) (i.e., (U, 5), (U, 6), (U, 7), and (U, 8)) are defined in the Figure 3-16 (b). The specific parameters in the SLS process and details about the material for the experiment are listed in Table 3-11.

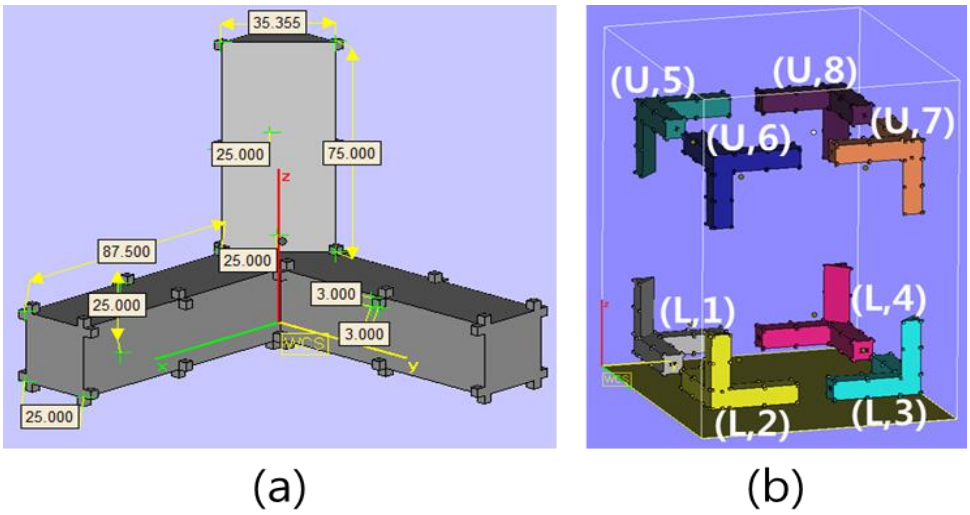

Figure 3-16 a) The CAD part sample, b) Arrangement of samples in the printing bed

Table 3-11 SLS process setting for an experiment

Parameters	Experimental Setting
Machine	sPro60 HD (3D systems)
Layer thickness	0.1 mm
Laser power	
Inner side	10 W; for part building
Outer side	4 W; for curing
Laser scan speed	6 m/s
Build chamber temperature	171 – 174 degrees Celsius (°C)
Material	Duraform PA (Plastic/ PA12)

After each sample part was fabricated, it was measured using the Formtracer® equipment (Mitutoyo) so that numerical data of surface deformations could be obtained (Figure 3-17). Figure

3-17 (a) illustrates the part sample on the Formtracer®. Figure 3-17 (b) and (c) shows how the top (T) and the bottom (B) face of each sample was measured, respectively. Observational data of the printed parts shows that bending was found in the printed parts at the lower location more than at the upper location. The bending in printed parts at the lower location was significant such that these parts do not level properly with a flat surface. Figure 3-18 specifically compares the lower part (L, 2) and the upper part (U, 6) in both the x and y directions. It is clear that the lower part (L, 2) has more significant bending deformation than the upper part (U, 6).

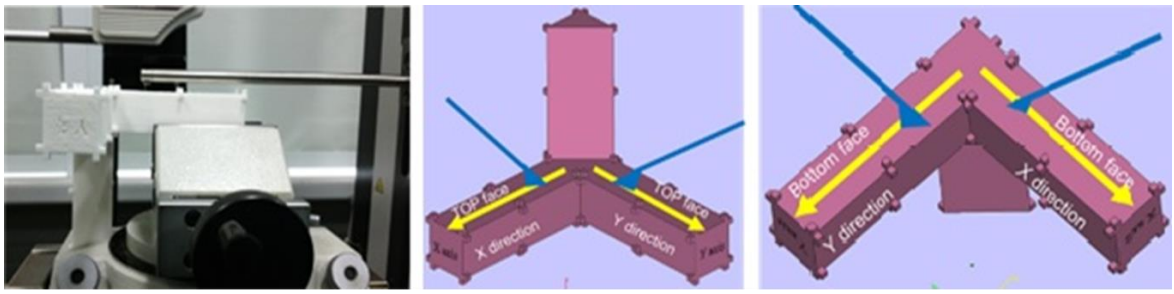

(a) (b) (c)

Figure 3-17 a) Measurement on the Formtracer®, b) Top face measuring, and c) Bottom face measuring

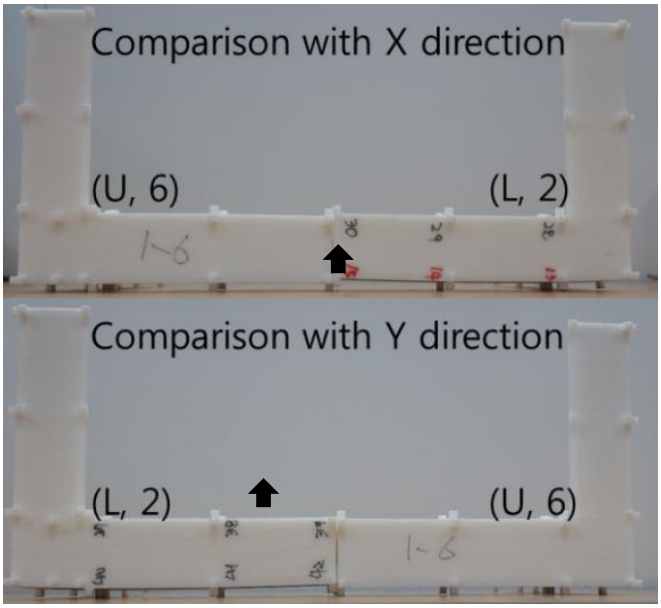

Figure 3-18 Comparison of bending deformation between the upper and lower positions

After measuring all eight samples and after the bending deformation data was obtained, a quadratic function was formulated through a regression model analysis. This quadratic function represents the pattern of bending deformation at both the top and bottom faces for each of the eight samples. The R-square (R^2) value measuring how close the data were to the fitted regression line was found to be

approximately 99%. Thus, it can be seen that the quadratic function is estimated as a statistically reliable representation of the bending deformation of the printed samples. The quadratic regression models for both x and y directions are shown in Table 3-12 for the two samples (L, 4) and (U, 7). In addition, the extent of bending deformation is evaluated using the gradient of the quadratic function 'a' while the coefficients 'b' and 'c' are not compared. This is due to the fact that the coefficients 'b' and 'c' are changed by the method of measurement. I note that the high value of the quadratic function 'a' means that the surface has more curved deformation.

Table 3-12 Example of the quadratic regression model

X and Y Directions	**Form of Quadratic**	
Part in x direction	$Z = \boldsymbol{a}X^2 + bX + c$	
Part in y direction	$Z = \boldsymbol{a}Y^2 + bY + c$	
Example	**Quadratic regression**	**R^2**
X direction Bottom of (L,4)	$Z = 0.000398X^2 - 0.02861X + 10.38$	99.6%
Y direction Top of (U,7)	$Z = 0.000051Y^2 - 0.00981Y - 10.99$	98.7%

I further compare the R^2 values for linear, quadratic, and cubic functions to see which function represents the bending decomposition the best (Table 3-13). The quadratic and cubic regression models' R^2 values are all higher than 93%, while the linear regression model has relatively low R^2 values to guarantee a good fit for the deformation patterns. This comparison implies that the percentage of data variance can be better explained using either the quadratic or the cubic regression function. Further observations show that the deformation patterns of the 3D printed parts are convex downward due to the vertical residual stresses that exist between sintering layers. Thus, the quadratic regression model was used as the fitting function for the SLS based 3D printed parts' deformation in this study.

Table 3-13 R^2 Value of each regression model

			R^2 (%)		
Sample	Direction	Surface	Linear	Quadratic	Cubic
(L,1)	X	Top	90.5	99.4	99.5
		Bottom	37.2	99.5	99.7
	Y	Top	0.8	94.1	94.2
		Bottom	2.1	99.3	99.4
(L,2)	X	Top	2.0	94.1	94.5
		Bottom	74.9	99.9	99.9
	Y	Top	1.7	94.7	95.2
		Bottom	48.7	99.5	99.6
(L,3)	X	Top	90.0	99.3	99.4
		Bottom	62.1	99.7	99.8
	Y	Top	91.8	99.6	99.6
		Bottom	68.0	99.8	99.9
(L,4)	X	Top	0.8	93.0	93.1
		Bottom	56.3	99.6	99.7
	Y	Top	93.8	99.7	99.7
		Bottom	63.2	99.8	99.9

To evaluate the pattern of the bending deformation, a box plot analysis was conducted for all eight-part samples between the lower (L) and the upper (U) locations of the part bed, between the top (T) and the bottom (B) faces of each part, and between the x- and y- directions (Figure 3-19). For example, XBL represents the quadratic coefficient *'a'* in the x-direction for the part measured at the bottom face and located at the lower location of the part bed. I note that the part samples located in the lower location of the part bed not only show a significant difference in the bending deformation between the top and bottom faces, they also show a greater extent of bending than the upper section. That is, it can be observed that the coefficient *'a'* for parts at the lower locations (i.e., XTL, XBL, YTL, and YBL) was found to be higher than the others, where the bottom surface is the highest (i.e., XBL and YBL).

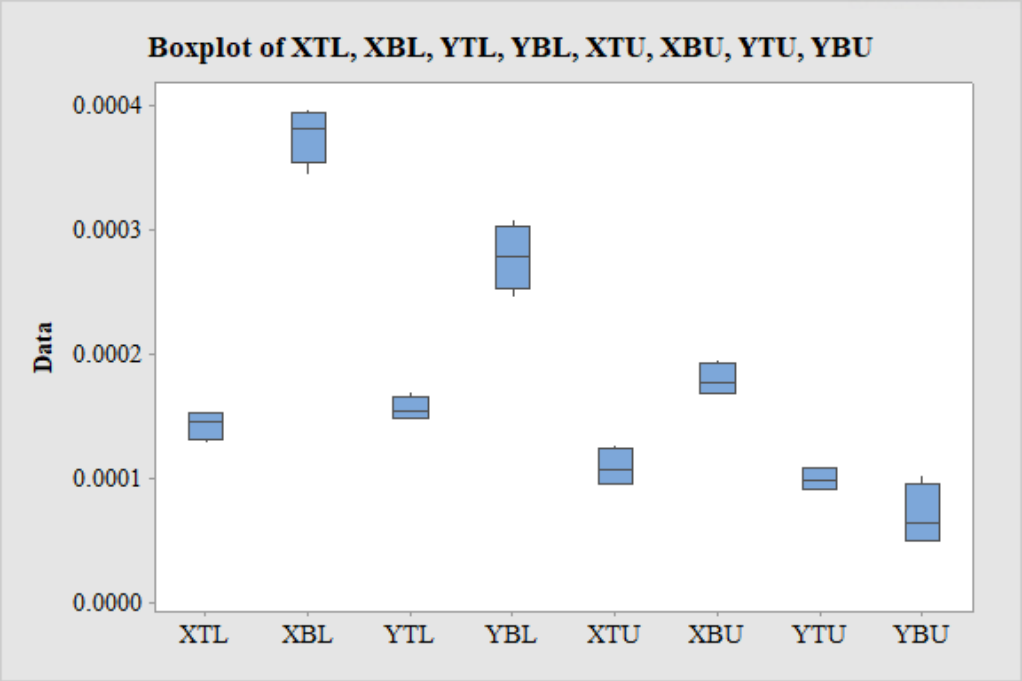

Figure 3-19 Boxplot of quadratic coefficient 'a' of a regression model of sPro60 samples

As can be seen in Figure 3-20, the deformation is more severe, although there is a difference in the degree when the location is low. In the case of the surface, the lower surface shows more deformation. In addition, the deformation of x-direction is more severe than the deformation of y-direction. ANOVA for each element is shown in Table 3-14. As a result, there is a significant difference in not only the surface but also the location and the direction. However, there is a significant difference in the interaction effect. This is considered to be caused by the complicated phenomenon of bending deformation. Normality was confirmed by a residual plot (Figure 3-22). However, it was confirmed that the randomness was insufficient in the Versus order or Versus fits graph. Since these parts were made in one batch, there is no order randomness.

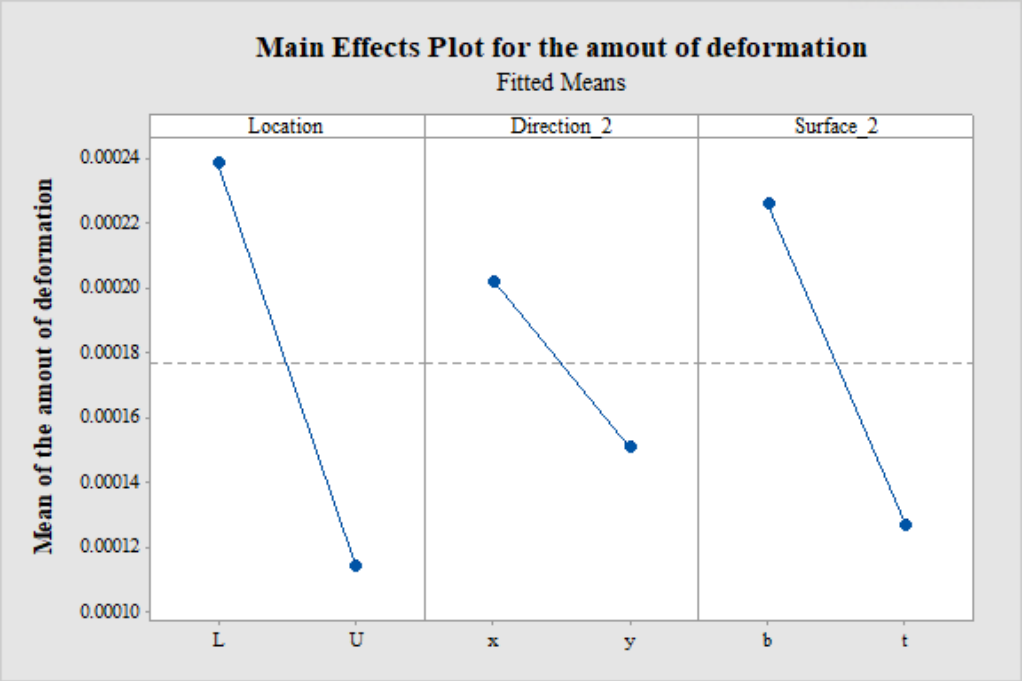

Figure 3-20 Main effects plot for the amount of deformation for sPro60

Table 3-14 ANOVA for the amount of deformation for sPro60

Source	*DF*	*Adj SS*	*Adj MS*	*F-Value*	*P-Value*
Location	1	123132	123132	394.22	0
Direction	1	20961	20961	67.11	0
Surface	1	78309	78309	250.71	0
*Location*Direction*	1	570	570	1.82	0.19
*Location*Surface*	1	48750	48750	156.08	0
*Direction*Surface*	1	22419	22419	71.78	0
*Location*Direction*Surface*	1	63	63	0.2	0.657
Error	24	7496	312		
Total	31	301700			

R-sq: 97.52% R-sq(adj): 96.79% R-sq(pred): 95.58%

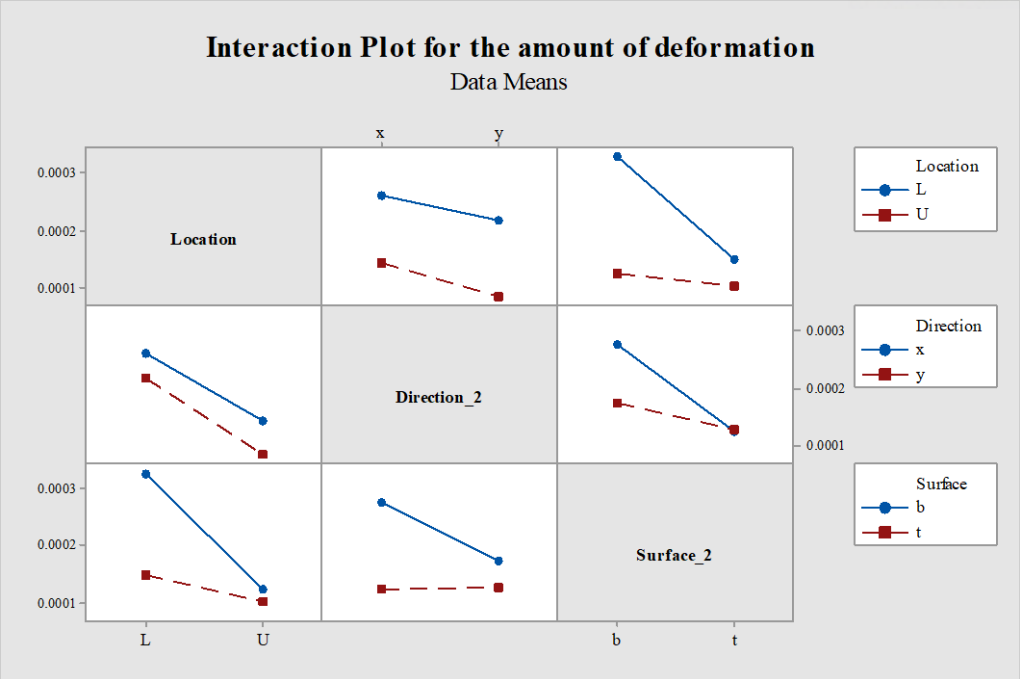

Figure 3-21 Interaction plot for the amount of deformation for sPro60

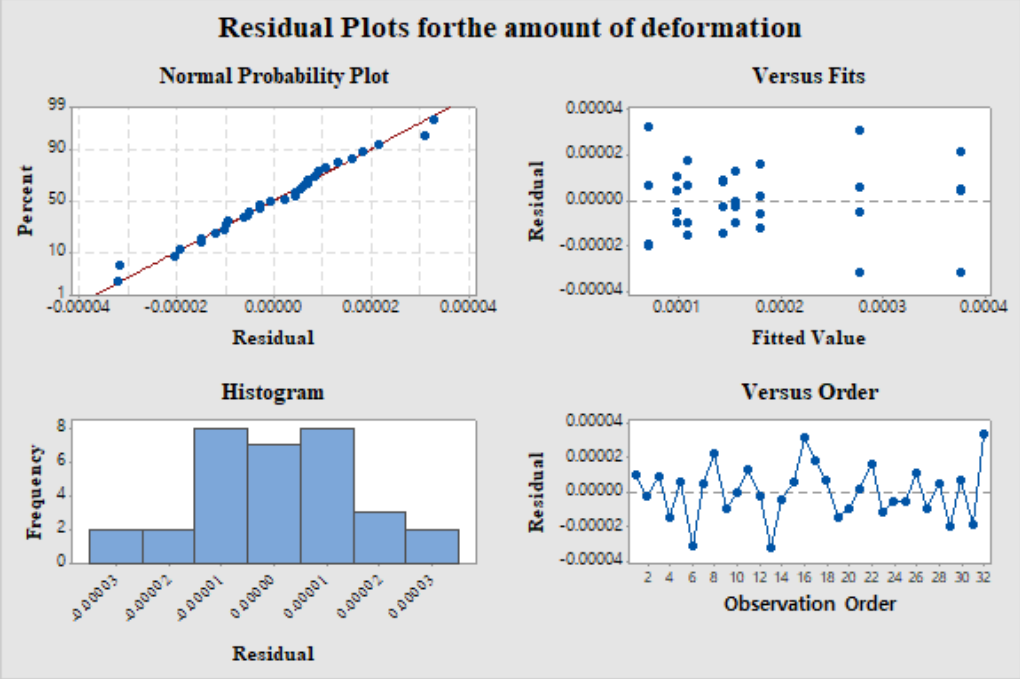

Figure 3-22 Residual plots for the amount of deformation for sPro60

3.2.3 Analysis results of deformation patterns depend on sample design and layout

The results of the previous analysis show that the degree of deformation varies depending on the location. In this experiment, I tried to find out if the same phenomenon occurs in other 3D printer machines by making a similar layout. In addition, to understand the degree of deformation according to the sample design as well as the position, additional experiments were carried out as follows.

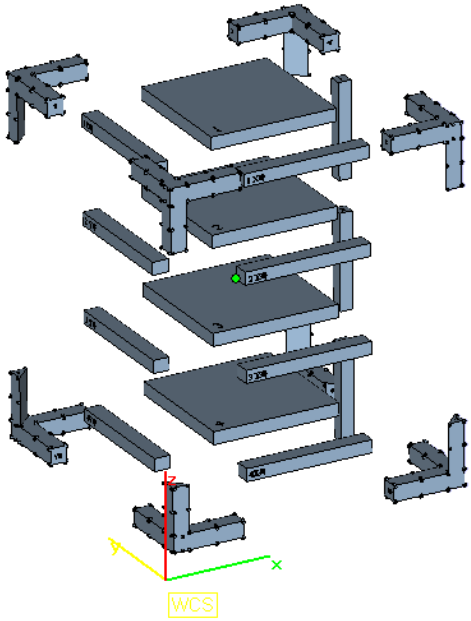

Figure 3-23 sPro230 deformation pattern test layout

In order to grasp the shape changes in various shapes and various positions, the parts were fabricated as shown in Figure 3-23 using a GMK 3D Printer (sPro230). In particular, I examined the difference in the degree of bending according to the x-direction and the direction of y, the difference in the bending degree when the cross section is widened, and the length difference according to the arrangement height. The analysis of the results was largely divided into the analysis of the same parts as in Section 3.2.2 and the analysis of bars and plates. The size of the bar was 20mm x 25mm x 200mm and the plate size was 20mm x 200mm x 200mm. As shown in Table 3-15, the laser power was set higher than the laser power of sPro60 and the scan speed was set faster. I analyzed the same parts that I made in Section 3.2.2 to analyze the differences in 3D printer machines.

Table 3-15 Experiment parameter

Parameters	Experimental Setting
Machine	sPro230 (3D systems)
Layer thickness	0.1 mm
Laser power	
Inner side	53 W; for part building
Outer side	18 W; for curing
Laser scan speed	10.16 m/s
Build chamber temperature	173 degrees Celsius (°C)
Material	Duraform PA (Plastic/ PA12)

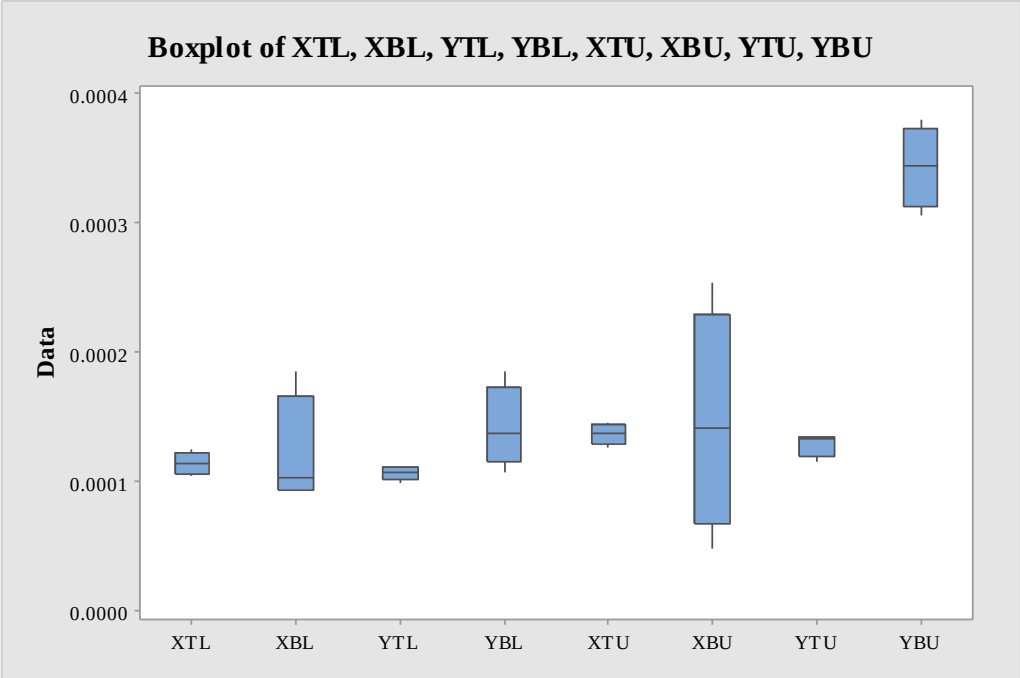

Figure 3-24 Boxplot of quadratic coefficient 'a' of a regression model of sPro230 samples

The tendency for the fabricated parts to be convex downward, the deformation at the bottom surface to be larger and the standard deviation of the degree to be larger, were found to be the same even if the devices were different. However, unlike sPro60, the deformation of samples made at the top was found to be larger (Figure 3-25).

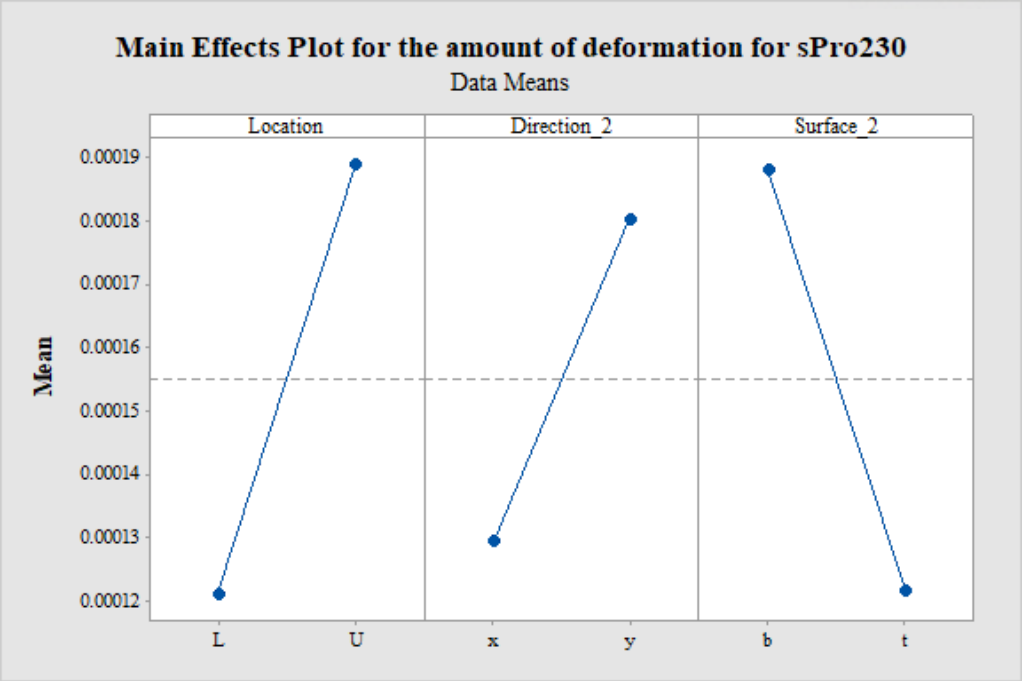

Figure 3-25 Main effects plot for the amount of deformation for sPro230

Compared with the sPro60 machine, the sPro230 has a large batch volume meaning a greater load on the bottom section. Thus, samples located at the bottom of the sPro230 are less likely to be affected by to the weight of the powder and the sample. Moreover, the thermal deformation is smaller than that fabricated from the sPro60. This is because, in the sPro60, the heat source is only on the upper part and the part bed plate, whereas in the sPro230 the heat source is also on the part bed wall. Therefore, the temperature difference by height is small in the case of sPro230.

Table 3-16 ANOVA for the amount of deformation (x100,000) for sPro230

Source	*DF*	*Adj SS*	*Adj MS*	*F-Value*	*P-Value*
Location	1	36856	36856	25.93	0
Direction	1	20706	20706	14.57	0.001
Surface	1	35378	35378	24.89	0
*Location*Direction*	1	15664	15664	11.02	0.003
*Location*Surface*	1	16653	16653	11.72	0.002
*Direction*Surface*	1	27495	27495	19.34	0
*Location*Direction*Surface*	1	15664	15664	11.02	0.003
Error	24	34115	1421		
Total	31	202532			

R-sq: 83.16% R-sq(adj): 78.24% R-sq(pred): 70.06%

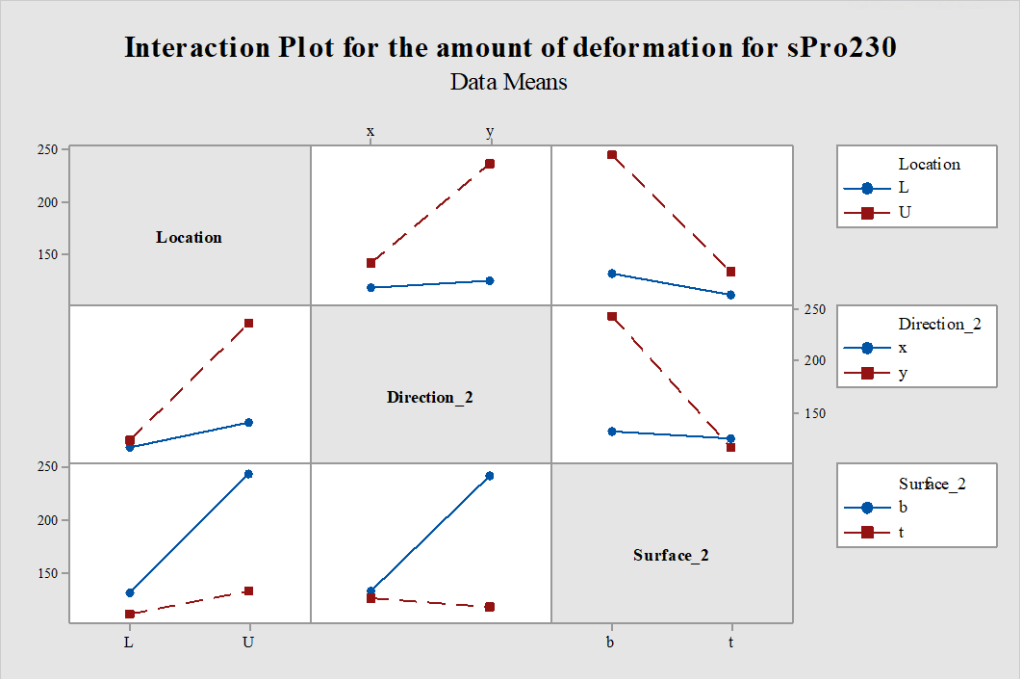

Figure 3-26 Interaction plot for the amount of deformation for sPro230

The samples of sPro230 were the same as the samples of sPro60. ANOVA for each element is shown in Table 3-16. As a result, there was a significant difference in not only the surface but also the location and the direction. The effect of interaction was also significant, especially in the case of the sample made at the upper part, where the bending deformation is prominent in the bottom surface of the y-axis direction (Figure 3-26). Normality was confirmed by a residual plot (Figure 3-27). However, it was confirmed that the randomness was insufficient in the Versus order or Versus fits graph. Since these parts were made in one batch, there was no order randomness.

Through the main effects plots (Figure 3-28) of the bar and plate data of sPro230, it was confirmed that the difference between the sample shape and the top and bottom surfaces affected the deformation. In the case of the sample shape, the plate bended more than twice as much as the bar. And the upper surface was more severely bended - twice as much as the lower surface. ANOVA results of the plate data and sPro230 are shown in Table 3-17. As a result, it was confirmed that there was a significant difference between sample shape and face position. Normality was confirmed by a residual plot (Figure 3-29). However, it was confirmed that the randomness was insufficient in the Versus order or Versus fits graph. Since these parts were made in one batch, there was no order randomness.

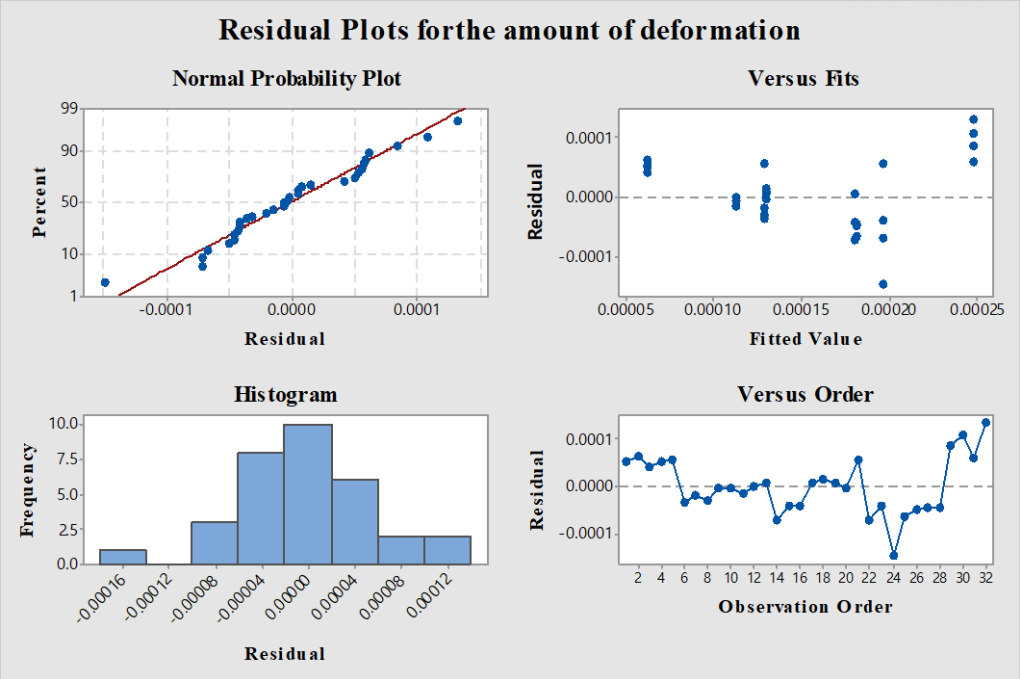

Figure 3-27 Residual plots for the amount of deformation for sPro230

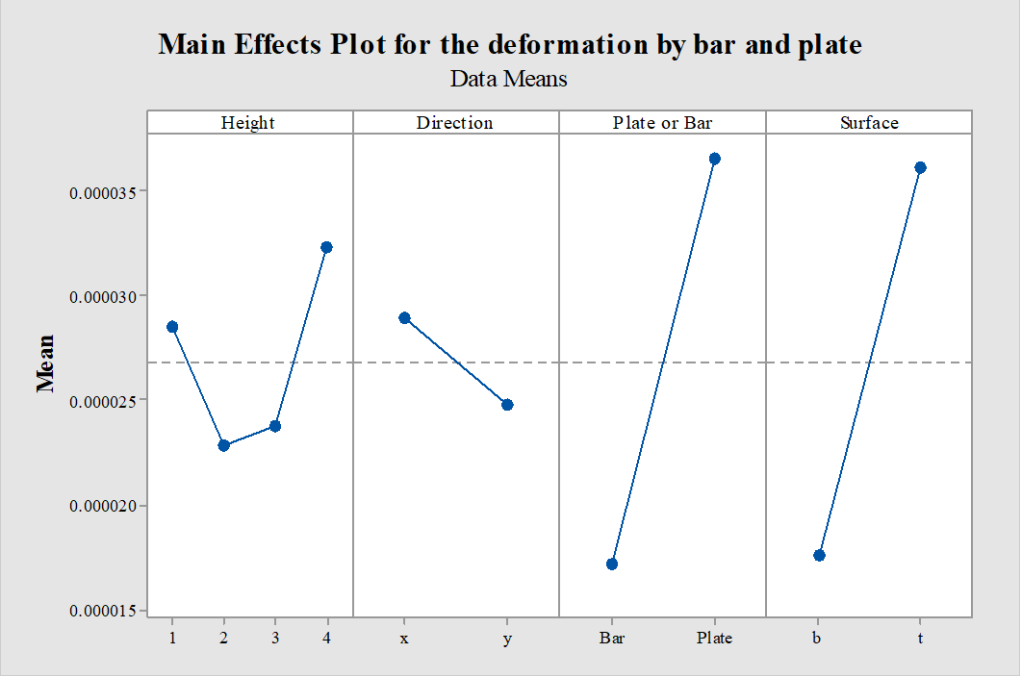

Figure 3-28 Main effects plot for the amount of deformation by bar and plate for sPro230

In addition, the difference in sample contraction rate according to the batch height was confirmed. The data is shown in Figure 3-30. As the layout was placed at the top, it could be seen that the height was smaller than the CAD data.

Table 3-17 ANOVA for the amount of deformation (x100,000) by bar and plate for sPro230

Source	*DF*	*Adj SS*	*Adj MS*	*F-Value*	*P-Value*
Height	3	4.647	1.549	2.55	0.078
Direction	1	1.382	1.382	2.28	0.144
Plate or Bar	1	30.323	30.3226	49.98	0
Surface	1	27.658	27.6582	45.59	0
Error	25	15.166	0.6067		
Total	31	79.176			

R-sq: 80.84% R-sq(adj): 76.25% R-sq(pred): 68.62%

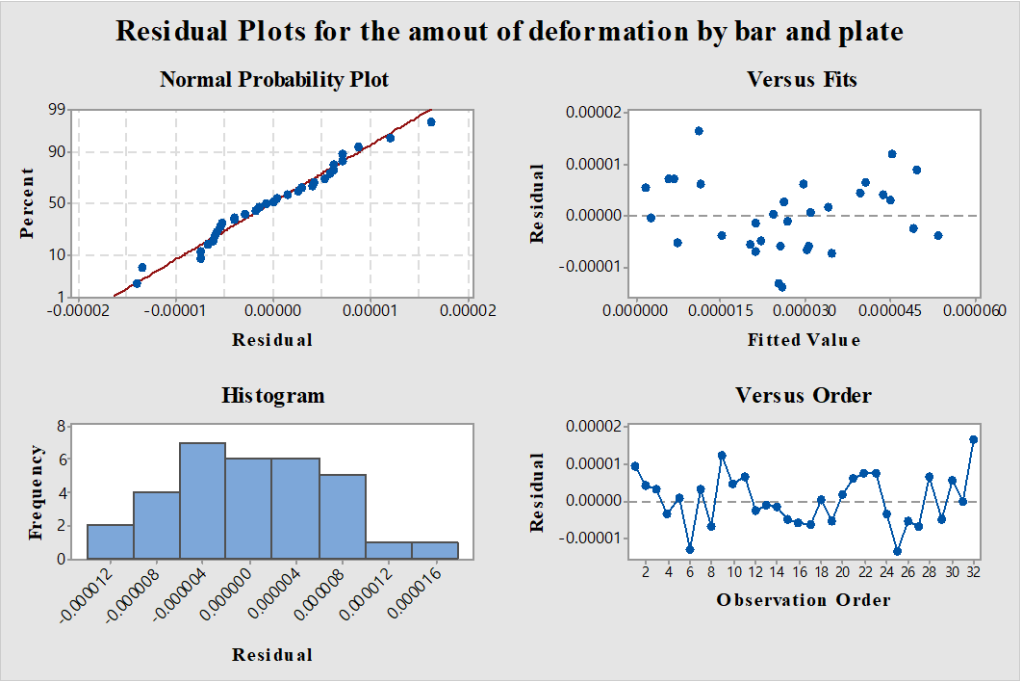

Figure 3-29 Residual plots for the amount of deformation by bar and plate for sPro230

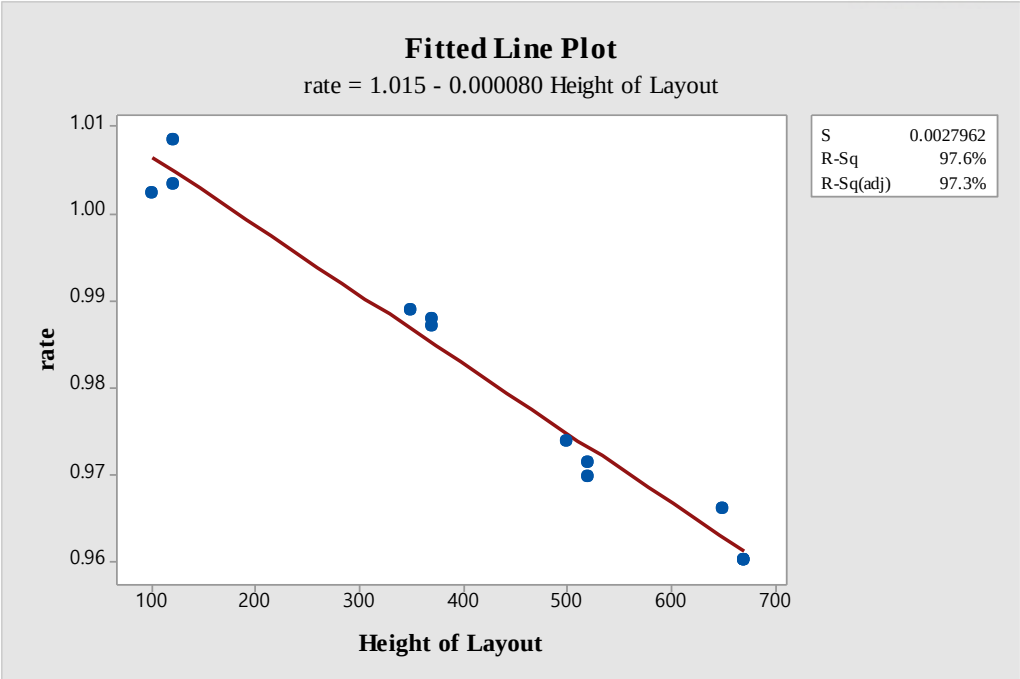

Figure 3-30 Linear regression model of z-rate vs height of the layout

3.3 The effect of humidity for 3D printed samples

The measurement data of company and the measurement data of UNIST are different. So I tried to find the cause of this discrepancy. Then the porosity rate of SLS printed samples is high, so humidity affect to dimension of SLS printed samples (Cadoni, Labibes, Albertini, Berra, & Giangrasso, 2001; Gou et al., 2015; X. Li et al., 2003). Therefore, the subsequent experiment was conducted to analyze the effects of humidity.

3.3.1 3D printed parts using the SLS process

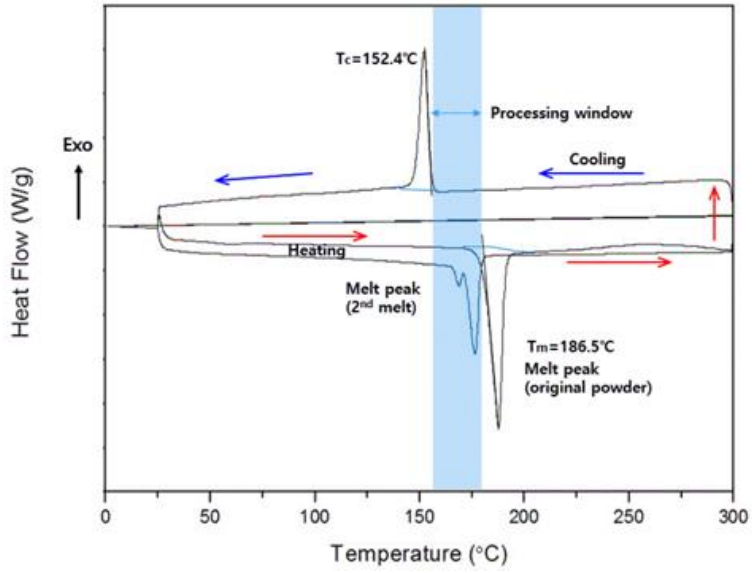

Figure 3-31 DSC curve for PA12 powder

SLS process parameters depend on the thermal properties of the powder material, such as melting and recrystallization temperatures. Using differential scanning calorimetry (DSC), I confirmed the thermal properties of polyamide 12 (PA12) powder, a common material in the SLS process. Figure 3-31 illustrates the heating and cooling cycles of the PA12. The melting peak was 186.5°C, PA12 underwent an endothermic phase transition from solid to liquid, and a recrystallization peak was observed at 152.4°C, indicating that PA12 exhibits an exothermic phase transition from liquid to solid. The range between the melt and the recrystallization peak was determined to be the processing window of the PA12 powder for the SLS process.

Figure 3-32 shows the shape of the PA12 powder using a scanning electron microscope (SEM) at magnifications of 500 and 3000 times. Powder particles showed various shapes, but most were potato-shaped. The longest diameter was observed not to exceed 100μm and this affected the layer thickness of the 3D printed samples and increased the workspace during the printing process.

To verify their properties, 3D printed samples were fabricated using PA12 powder, with a 3D Systems sPro60 printer. Considering the material properties, the laser power was 9 W and the layer

thickness was 100 μm. Based on DSC characterization results, I set the powder bed temperature to 160 ° C to avoid local contraction and partial deformation. As can be seen in Figure 3-33, there were three samples that are designed in a hexahedral shape. The sample sizes were 60 mm x 30 mm x 30 mm for x-, y-, and z-directions. As a reference point for dimension measurement, several rectangular bumps were engraved on each side.

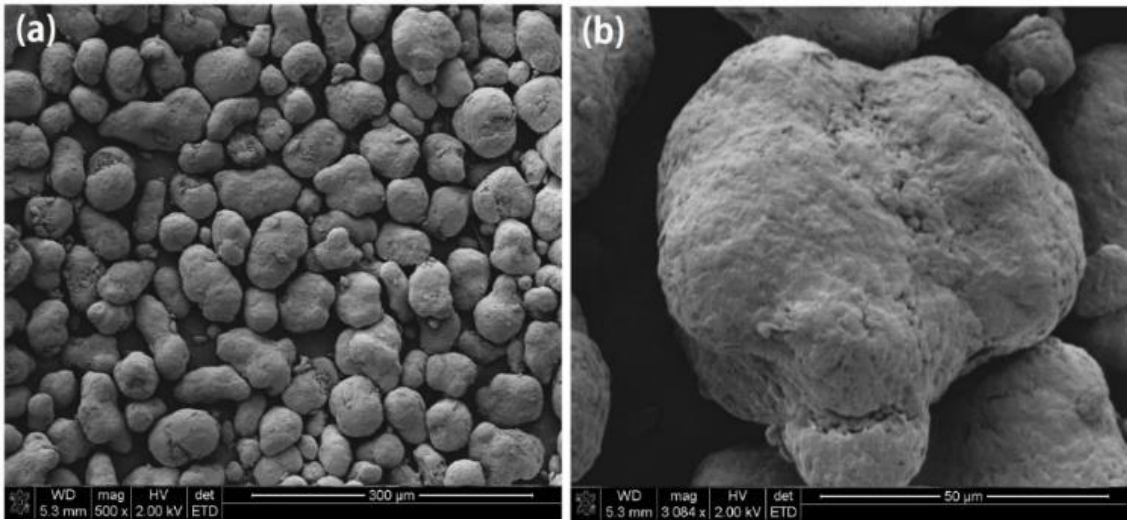

Figure 3-32. PA12 powder morphology with multiple magnifications

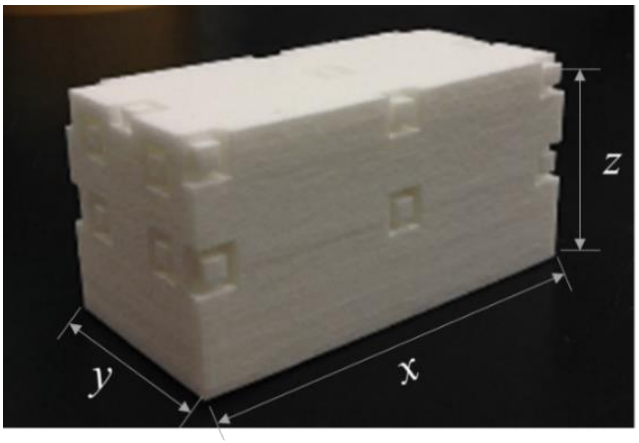

Figure 3-33. Dimensions for each direction of the SLS part

Figure 3-34 shows the appearance of the sintered PA12 powder on the surface and middle of the sample part. The middle view was obtained by dividing the sample in half and observing the interface. It was observed that more powder particles on the surface were fused than in the middle. The morphology observed in the middle was more porous than the morphology observed on the surface. In addition, some spherical particles were found on the sintered surface, confirming that the powder particles did not completely dissolve. This could have been the result of the indirect irradiation of the laser to the particles, and gases generated during the sintering process. During melting and

recrystallization, the chamber temperature and the processing time per layer must not have been high or long enough for gases to escape out of the molten polymer.

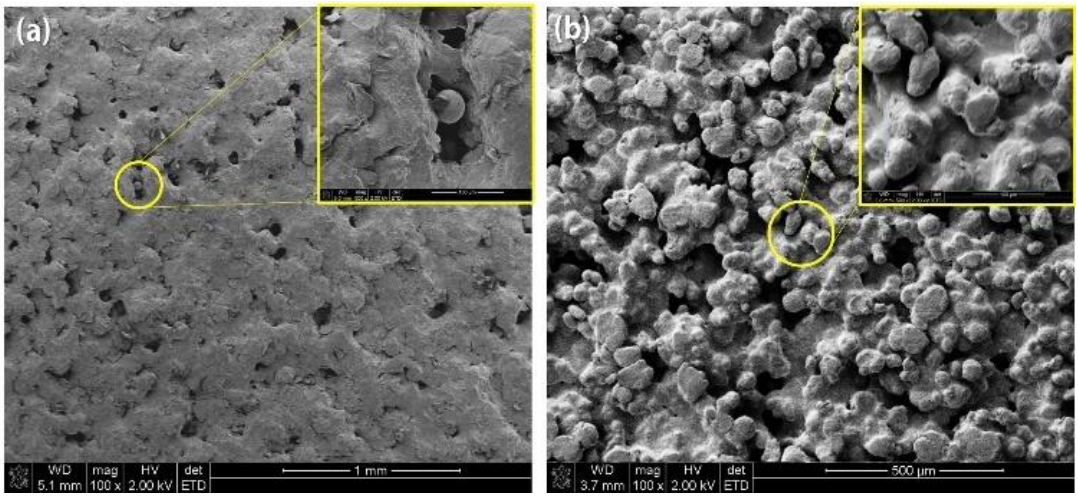

Figure 3-34. The microstructure of a sintered sample (a) at the surface and (b) in the middle

Due to their porous structure, 3D printed parts can be exposed to moisture and become deformed. As shown in Figure 3-35, the deformation of 3D printed parts was observed over time. Many researchers have identified the loss of mechanical strength due to deformation and water absorption of 3D printing components (Haffane, Benameur, & Vergnaud, 1997; Lassila, Nohrström, & Vallittu, 2002; J. Park, Tari, & Hahn, 2000; Suwanprateeb, 2007; Xing & Jiang, 2003). The following section discusses experimental studies to test the dimensional stability of 3D printed components in response to changes in the humidity of environmental conditions.

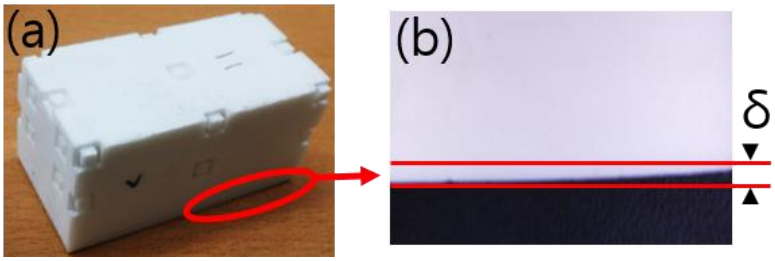

Figure 3-35. Deformed 3D printed part with the passage of time

3.3.2 Experiment: effect of humidity on 3D printed parts

Humidity cycling was performed to investigate the effect of humidity on the dimensional stability of 3D printed parts. According to ASTM-D6207, the highest humidity is 95 ± 5% RH and the lowest humidity is 15 ± 5% RH. Thus, the humidity conditions of this experiment were set to cycle from 20% to 90% RH. Given the control limits of the ESPEC ARS-0390 environmental chamber used in this experiment, the ramp up and down time was determined to be 1 hour. The residence time at the highest and lowest RH levels was 12 hours, which is enough time to sufficiently saturate and dry the sample. A complete humidity cycling profile is shown in Figure 3-36.

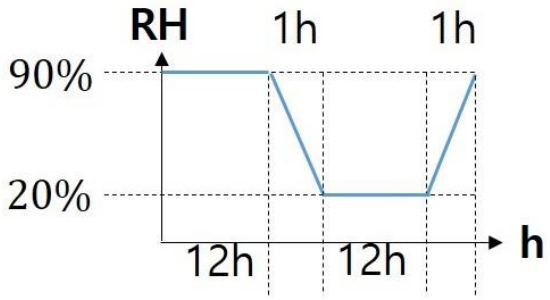

Figure 3-36. RH cycle profile

Strain gauges were attached to both the top and bottom of the sample to measure part deformation during the humidity cycle as shown in Figure 3-37. Strain values were recorded every minute during the humidity cycle. Strain gauge values of five humidity cycles were recorded. Figure 3-38 shows the strain history of the sample with respect to the humidity level during the humidity cycle. It was observed during all humidity cycles that the strain value had a positive correlation with humidity. There was a change between specimens, but the strain history of each cycle was almost the same except for the first cycle, which is regarded as the stabilization period of the environmental chamber and the specimen. Therefore, the strain history of the first cycle was excluded from the following analysis.

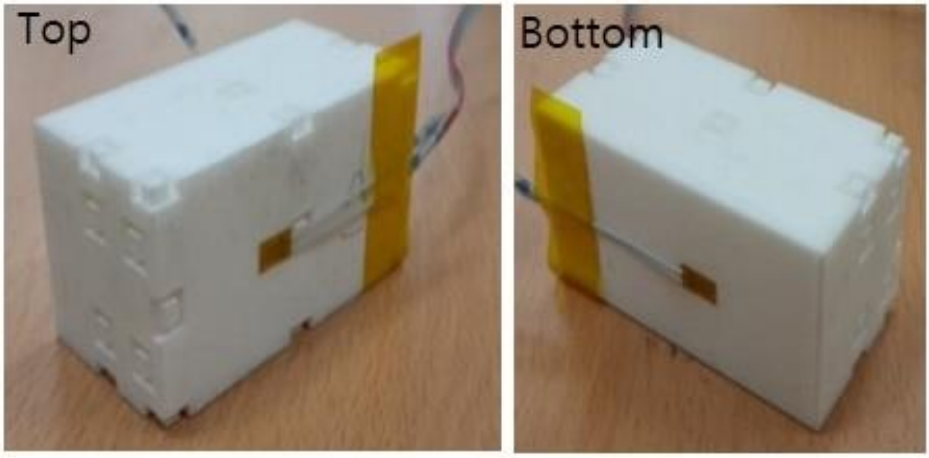

Figure 3-37. Samples with strain gauges

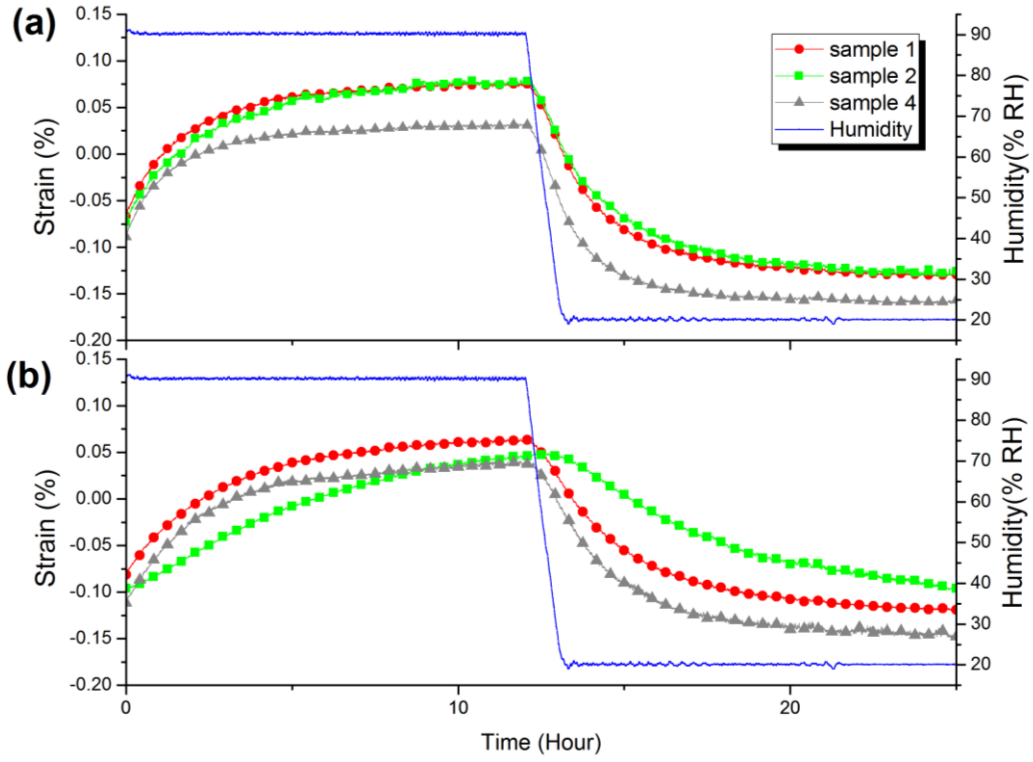

Figure 3-38. Strain history during a humidity cycle (a) at the top surface and (b) at the bottom side

Figure 3-39 shows the hysteresis loops of the top and bottom strain values of Sample 1. Changes in RH and strain values were consistent across multiple humidity cycles, indicating that the strain was in an elastic regime. It was found that the proximity of the top surface to the water outlet of the environmental chamber causes the top surface to expand and contract more than the bottom surface.

The highest and lowest strain values were recorded at 0.08% and -0.13%, respectively. Assuming that the RH levels of the test conditions are generally observable in normal use conditions, the results of this experiment indicate that the shape of the 3D printed parts may be inconsistent during field use.

3.3.3 Discussion

AM technology is widely used in the automotive industry, specifically the use of SLS in prototyping for assemblability testing. AM technology is also used for tool making and concept car manufacturing. In addition, due to the high design flexibility, the use of AM in the production of discontinued automotive parts for repair, or custom automobiles is becoming more and more popular. Dimensional requirements and conditions of use for 3D printed parts must be taken into account for the manufacture and use of additives in the automotive industry.

Figure 3-40 shows the average daily humidity distribution at the data station of the Korea Meteorological Administration in 2015. The lowest recorded average humidity was 20.9% RH in March and the highest in July at 93.6% RH. In the summer, June to August, daily deviations were as high as 55% RH. These statistics indicate that dimensional variations due to humidity differences found in the experiment can occur under normal conditions of use.

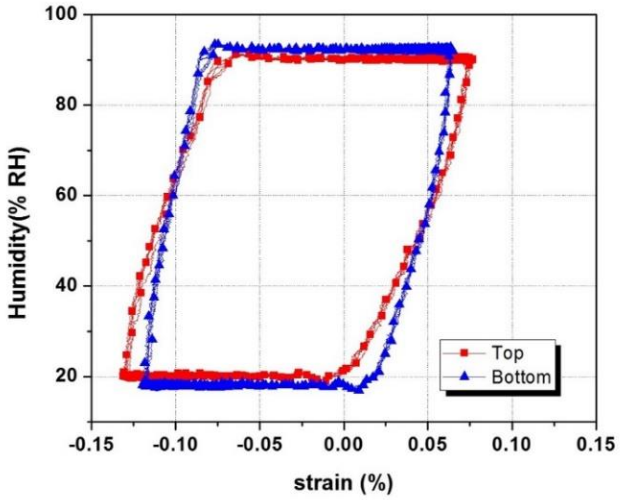

Figure 3-39. RH vs. strain hysteresis loop during humidity cycling

Automotive parts suppliers generally set the maximum dimensional tolerance of each part to ± 0.5 mm in relation to the original design. If so, assuming there is a door trim assembly created by the SLS process, as shown in Figure 3-41, the maximum RH difference in local RH record data is approximately 73%, resulting in a variation from 0.05% to -0.15%. If the distance between the two holes in Figure 3-41 (b) should be 300mm and given the same geometric tolerance of ± 0.5mm in dimensional accuracy and ± 0.5mm in position accuracy, then the dimensional change would be 0.15mm and -0.45mm, respectively. The overall displacement is 0.6 mm beyond the specification, compared with the typical 0.5 mm RMS displacement error.

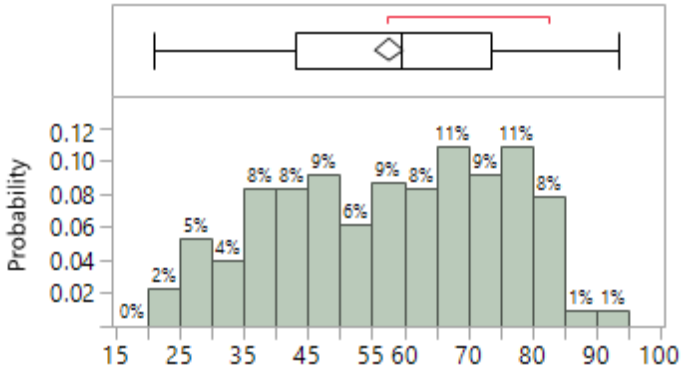

Figure 3-40. RH distribution in 2015

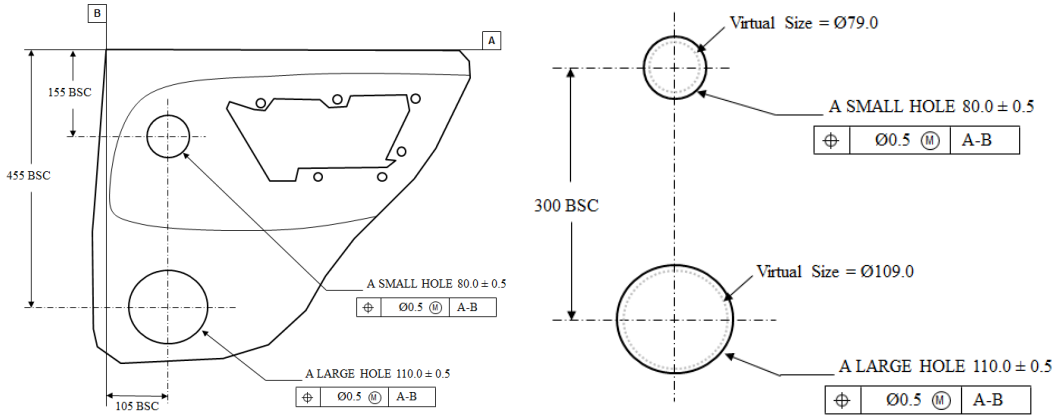

(a) ***(b)***

Figure 3-41. An example of dimensional specifications of (a) a sample door trim design, and (b) its geometric dimensions and tolerances

As can be seen in Figure 3-41 (b), the probability of having a good part under the dynamic environment of the specified RH change can be calculated by Eq. (3-12), taking into account the inspection criteria between holes in the MMC (maximum material condition).

$$P\{Good\ \ Part\} = \prod_{all}[P\{Good\ \ dimension\} * P\{Good\ \ Location\}] \qquad \textbf{3-12}$$

Suppose that a 0.05% strain variation reduces the probability of having up to 1% of an excellent dimension or position characteristic of a part. The probability of having a good part through the four features (two-position and two-dimensional requirements) is calculated to be between 89% and 96% in the% change from -0.15% to 0.05%. As a result, displacement changes in the SLS components may cause residual stresses between the joints, which may adversely affect the performance, life, quality, and reliability of assembly components due to humidity changes. In other words, in engineering applications, 3D printing components made with SLS require careful consideration of humidity conditions.

3.4 Summary

In this section, I examine the factors affecting the sample bending deformation, which are the layer thickness and the laser power. The thicker the layer, the less variation due to deformation. The laser power exercises influence the material's density. Depending on the placement, 3D printer used, and sample design, differences in bending deformation appear. Meaning, the higher the shrinkage ratio in the z-direction, the greater the bending deformation is.

This research also examined the effect of humidity changes on 3D printed parts. Multiple 3D printed sample parts have been produced using an SLS 3D printer with the PA12 powdered material. Humidity cycling tests have been conducted while monitoring the stain history of the 3D printed sample parts with respect to changes in the humidity levels. The test results demonstrated a change in humidity from 20 % RH to 90 %. RH yielded a total %-strain change of 0.2 %. A survey of RH history showed that the minimum and the maximum RH in a year was recorded as low as 20.9 % and as high as 93.6 %, respectively; and the humidity change could, as an example, result in the violation of the dimensional requirement of a door trim assembly design specification. Thus, careful consideration in terms of dimensional stability due to humidity levels is required for 3D printed parts from the design stage to field application.

The parameters mentioned above are related to the physical properties of the causes of deformation and there are many factors that must be modified in 3D printer equipment, which is costly. However, there is a great difficulty in realizing the necessity of costly modification of the 3D printer equipment. Therefore, in this study, the compensation model is used as a method to improve the accuracy of 3D printed products. And the compensation model related research is investigated as described in Chapter 2. However, those compensation models were developed focusing on the shrinkage instead of the bending deformation occurring in SLS or SLM. Herein, a compensation model to mitigate the bending deformation, even when there is no support structure, as in the SLS process, is proposed in Chapter 3.

4. Deformation Compensation Framework

Many auto part manufacturers in the automotive industry have recognized AM technologies as a promising method for their pre-production stages and have attempted to operate various types of 3D printers in their design, research, and development (R&D), and production processes. In contrast to the traditional method with constraints in the geometric design of auto parts, AM can provide almost perfect design freedom for parts (Edwards, O'Conner, & Ramulu, 2013). Therefore, automotive companies around the world have recognized the significance of AM technologies and are attempting to utilize high-performance 3D printers in their design and R&D processes. However, the application of 3D printing technology is considered limited to only the prototyping phase in the design process due to low cost-effectiveness and difficulty in controlling dimensional stability.

The most commonly used 3D printers are SLA and SLS. The SLS method is found to be superior in fabricating car parts with high mechanical properties and is used more extensively in the automotive industry (Choi, 2014; Han, 2013). However, one limitation of the SLS printing process is an issue in dimensional errors from thermo-mechanical deformation, such as contraction and expansion. These dimensional errors result from numerous control variables and the complicated deformation pattern. Thus, it is relatively difficult to mitigate these dimensional errors from the SLS process. Although the printer manufacturers have suggested that the quality of 3D printed samples can be better controlled by placing them at the center of the printer with only two-thirds of the entire space, these recommendations increase operation time and the total operating costs.

In Chapter 2, an analysis of the factors of transformation is provided. While relative humidity is not a problem in the manufacturing process, the laser power, and the layer thickness affect the physical properties and the laser power, and the layer thickness are not handled in the industrial field. Discussed in Section 3.1, the positional effects are greater than the laser power or the layer thickness effects. Therefore, for the compensation model framework presented in this chapter, I will focus on the sample design and bending deformation depending on the position of the sample placement. A model is developed to approximate the deformation of the sample and to compensate the CAD model during the pre-printing process so that the deformation of the sample is minimized.

4.1 Pre-Experiment

4.1.1 Experiment plan

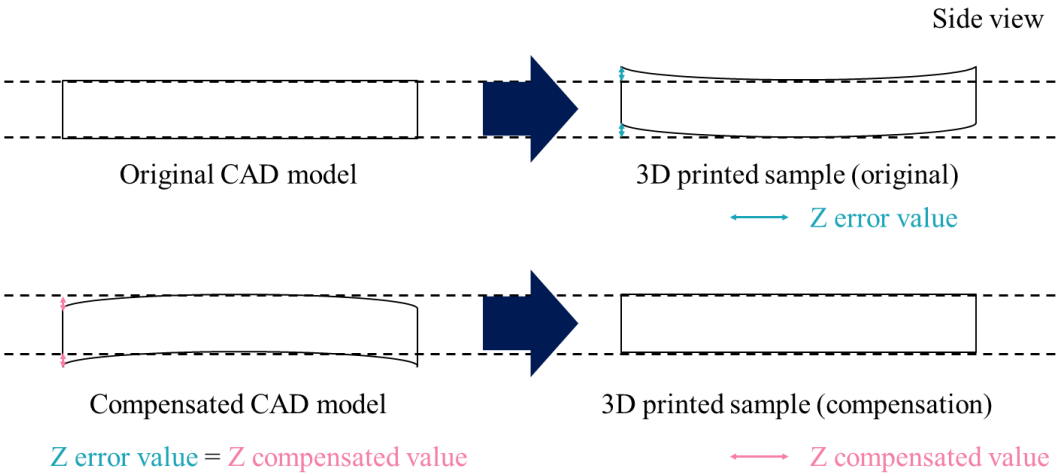

Figure 4-1 An illustration of the proposed compensation

The main idea of the dimensional compensation method is shown in Figure 4-1. Generally, the printed part is deformed in the direction in which the bottom surface is convex. I modified the CAD files to match the degree of this deformation so that the samples could be made closer to the original model. In this section, I try to verify the effectiveness of this method by revising the CAD file based on the measured data of the part after manufacturing the part.

Table 4-1 SLS process setting for an experiment

Parameters	Experimental Setting
Machine	sPro60 HD (3D systems)
Layer thickness	0.1 mm
Laser power	
Inner side	10 W; for part building
Outer side	4 W; for curing
Laser scan speed	6 m/s
Build chamber temperature	171 – 174 degrees Celsius (°C)
Material	Duraform PA (Plastic/ PA12)

The samples fabricated in this section are the same parts as those described in Section 3.2.2 and the manufacturing method is the same as in Section 3.2.2 as shown in Table 4-1. However, as described above, the CAD file was modified based on the results measured in Section 3.2.2. The compensation model is as in Eq. (4-1).

$$Zo = Zi - \left(YCB - \frac{YCB - YCT}{Ts}Zi\right) \times \left(Yi - CPYB + \frac{CPYB - CPYT}{Tl}Zi\right)^2 - \left(XCB - \frac{XCB - XCT}{Ts}Zi\right) \times \left(Xi - CPXB + \frac{CPXB - CPXT}{Tl}Zi\right)^2 \quad \textbf{4-1}$$

where:

- *Xi, Yi, Zi: x, y, z value of vertex data of original CAD data:*
- *(X or Y) C (B or T): The second-order coefficient a value of quadratic regression model* $(a(x\ or\ y)^2 + b(x\ or\ y) + c = Z)$ *of bottom surface (B) or top surface (T)*
- *T (l or s): The long section height value (Tl) and the short section height value (Ts) of Figure 4-2 (a)*
- *CP (X or Y) T: The (X or Y) coordinate value of the plane center of the triangular part of Figure 4-2 (b)*
- *CP (X or Y) B: The (X or Y) coordinate value of the surface of the form of Figure 4-2 (c)*

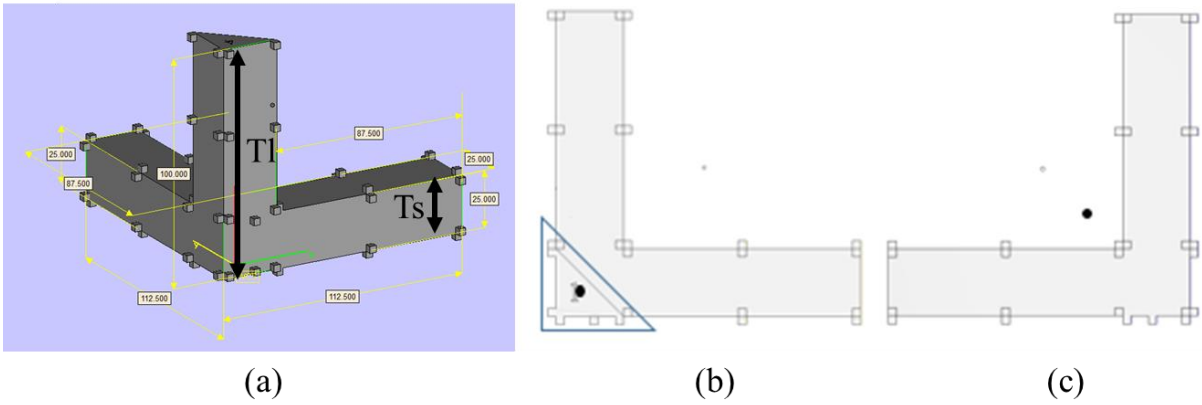

(a) (b) (c)

Figure 4-2 Parameters required for calculating the curvature center of the sample

The dimensional compensation model is largely divided into the compensation of the bending deformation found in the YZ plane and the compensation of the bending deformation found in the XZ plane, and the compensation equation of each plane is the same. $\left(YCB - \frac{YCB-YCT}{Ts}Zi\right)$ and $\left(XCB - \frac{XCB-XCT}{Ts}Zi\right)$ are formulas assuming linear changes in the second order coefficient according to the height change through the second order coefficient data of the quadratic regression model measured in Section 3.2.2. Therefore, the value corresponding to XCB or YCB measured in Section 3.2.2 on the bottom surface (height (Z = 0)) becomes the count value, and the value on the top surface becomes the count value on the top surface height. Thus, the deformation is compensated to a value as measured on each surface. $\left(Yi - CPYB + \frac{CPYB-CPYT}{Tl}Zi\right)^2$ and $\left(Xi - CPXB + \frac{CPXB-CPXT}{Tl}Zi\right)^2$ show the change of centers of curvature in each layer. In addition, I assume that the center of gravity of each section moves linearly with height and therefore I are able to derive the dimension correction model.

The compensation model was applied to four samples with a pronounced bending tendency in Section 3.2.2. The compensation model was applied to the original CAD modeling STL file to derive

the modified STL file. Figure 4-3 (a) shows the STL file to which the compensation model of the sample (B, 2) was applied. In order to fabricate the modified STL file equal to the initial experimental conditions, the compensated samples in the printer were placed in the same position as shown in Figure 4-3 (b).

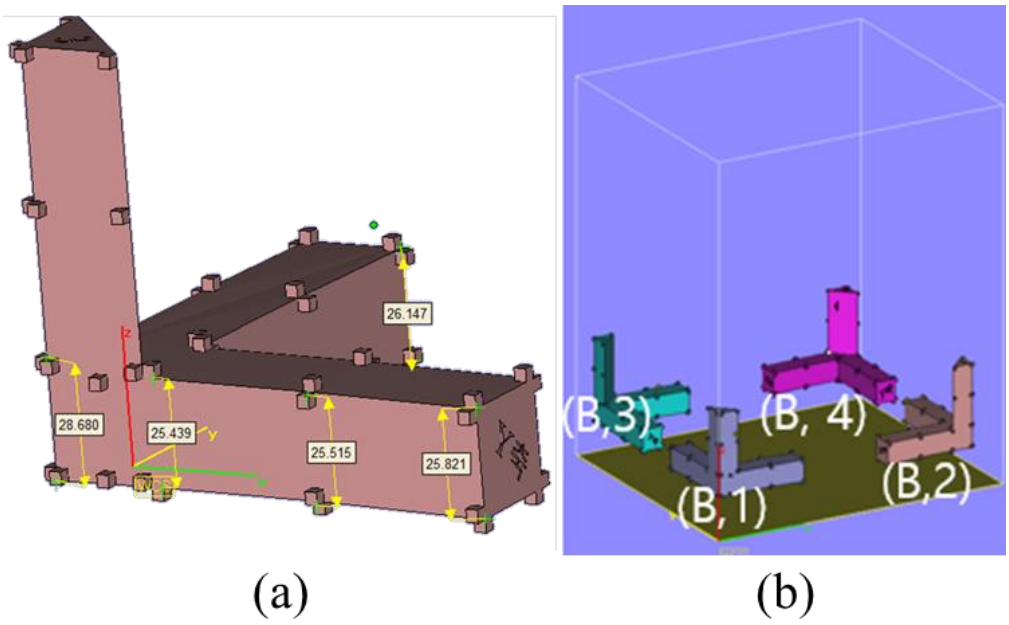

Figure 4-3 (a): Compensated CAD data (b): Layout of compensated samples

4.1.2 Result

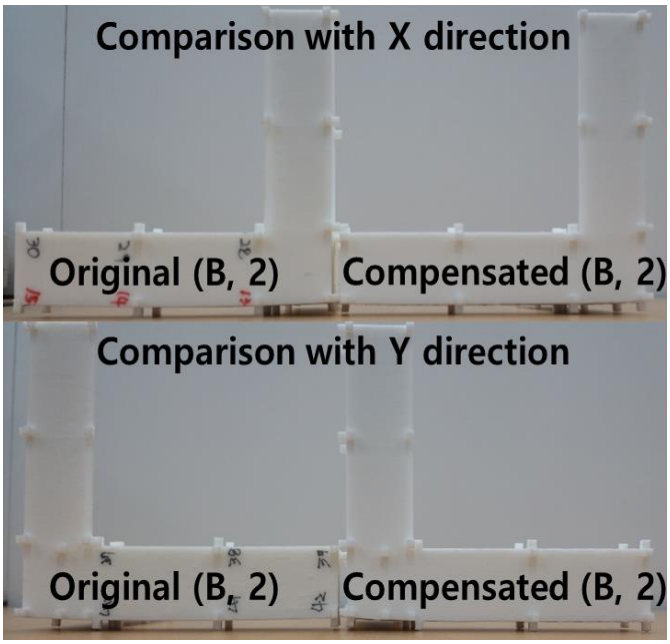

Figure 4-4 Comparison with before and after compensation

Table 4-2 The second-order coefficient of the quadratic regression model

Direction	*Surface*	*Original*	*Compensation-1*	*Compensation-2*
x	**t**	0.000153	0.000062	0.000088
x	**t**	0.000141	0.000064	0.000085
x	**t**	0.000152	0.000065	0.000103
x	**t**	0.000129	0.000087	0.000081
x	**b**	0.000382	0.000107	0.000142
x	**b**	0.000345	0.000085	0.000134
x	**b**	0.000381	0.000224	0.000103
x	**b**	0.000398	0.000178	0.000068
y	**t**	0.000147	0.000074	0.000059
y	**t**	0.000156	0.000065	0.000034
y	**t**	0.000170	0.000046	0.000051
y	**t**	0.000154	0.000050	0.000061
y	**b**	0.000246	0.000057	0.000156
y	**b**	0.000273	0.000064	0.000116
y	**b**	0.000284	0.000114	0.000083
y	**b**	0.000309	0.000082	0.000139

The compensation model compensates the bending in the opposite direction of the deflection of the X and Y axes of each sample, as shown in Figure 4-4. As a result of visual comparison between the compensation sample and the original sample, the bottom surface of the original sample floated without touching the floor, but the bottom surface of the compensation sample was in contact with the floor.

The four compensated samples were measured by a shape measuring machine (Mitutoyo Formtracer CS-3100), and the quadratic regression model was derived based on that data. The coefficients of the second order of the quadratic regression model were tabulated as follows in Table 4-2. The original data is the data from Section 3.2.2, compensated samples were fabricated twice to perform the reproducibility test, samples of compensation-1 were fabricated in November 2015 and samples of compensation-2 were fabricated in December 2015.

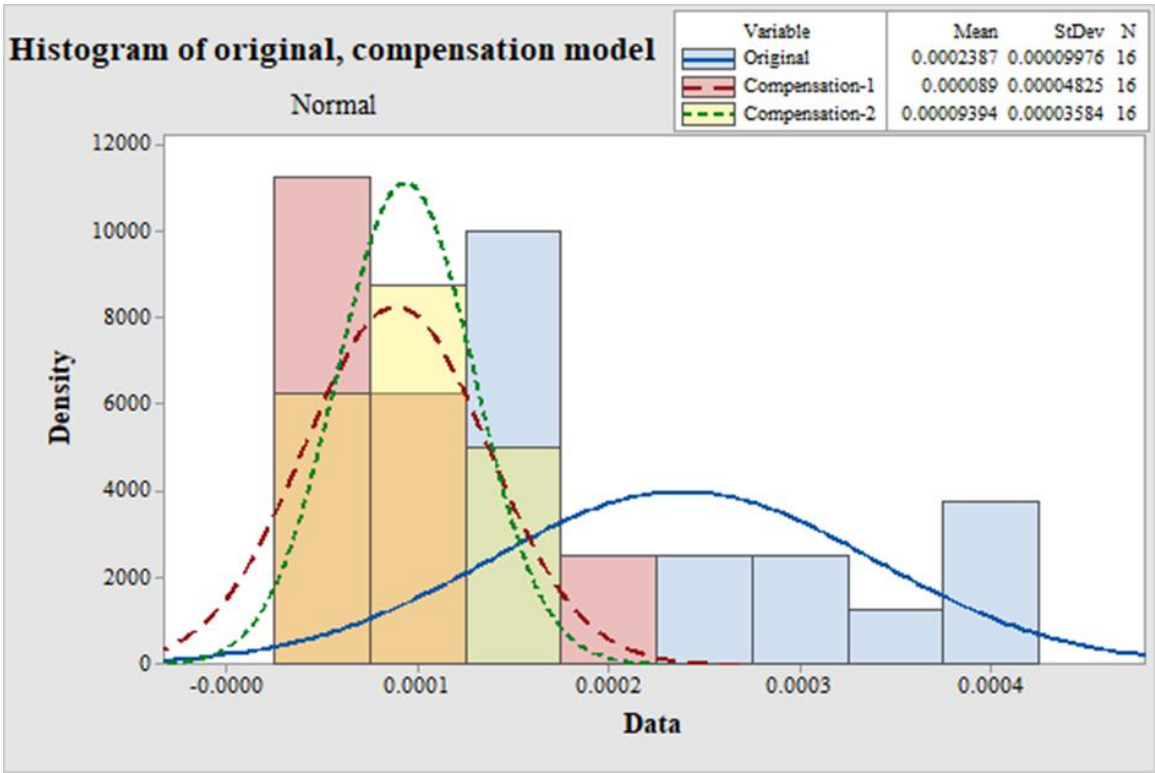

Figure 4-5 Histogram of the second-order coefficient of the quadratic regression model: for original, compensation-1, compensation-2

Table 4-3 The result of paired t-test

Paired t-test	*P-value*
Original vs Compensation-1	0.000
Original vs Compensation-2	0.000
Compensation-1 vs Compensation-2	0.739

As shown in Table 4-3, the results of the paired t-test showed significant differences between the samples made using the original CAD data and the samples made using CAD data with compensation. On the other hand, no significant difference was found between the samples made using the compensated CAD data.

In order to observe the degree of dimensional deformation in the X axis, Y axis, and Z directions according to the arrangement in the SLS 3D printer, samples of the three-axis direction column were fabricated and the data of the deflection deformation was obtained as the second-order coefficient of the quadratic regression model. Compensated samples were fabricated under the same conditions by applying the compensation model to correct the CAD file in the opposite direction in anticipation of the bending deformation of the original CAD file of the sample. The compensation effect was verified by 2-sample paired T-tests before and after compensation. As a result, it was confirmed that the bending deformation can be reduced to about 1/4 of that of the samples using the original CAD data.

4.2 Compensation framework

4.2.1 Schematic Compensation Flow Process

The schematic compensation flow process for dimensional deformation of SLS based 3DP parts is discussed in this section (Figure 4-6). Initially, the CAD models are designed for part geometry and measurement (Step 1). Then, they are arranged within the layout of SLS 3DP part bed (Step 2). After the SLS machine finishes fabricating the product(s), they are measured using the Formtracer® scanner and the deformations, such as bent sides or bending patterns, are analyzed and recorded (Steps 3-5). Next, this numerical data is analyzed using the regression model and the results are used as the basis for the compensation model (Steps 6-7). The original 3D CAD model is then compensated by substituting the coordinates of the regression model into this model and it is reproduced by arranging it within the printer as previously done (Steps 8-9). Finally, the modified samples are measured with the Formtracer® again and compared with the data recorded from the original part (Steps 10-11).

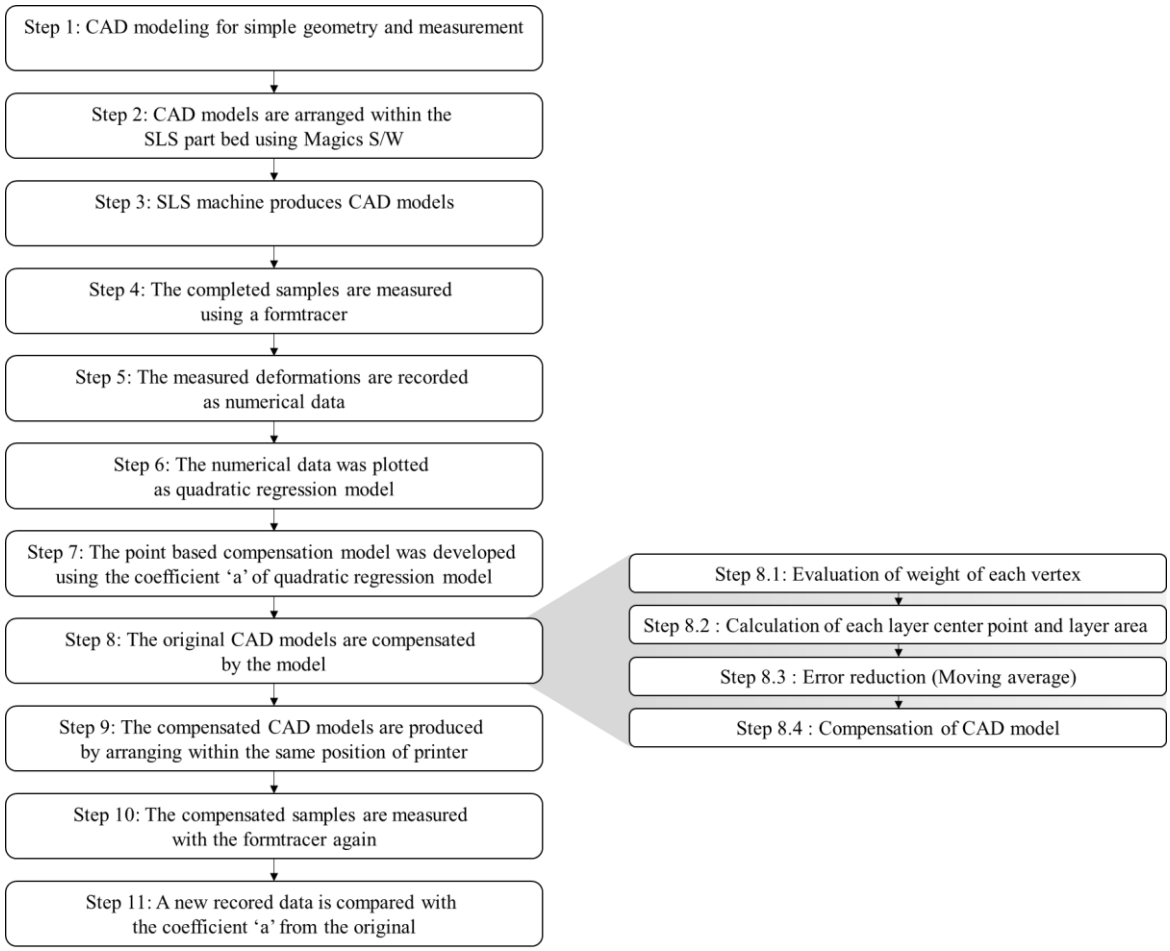

Figure 4-6 Compensation framework flow process for dimensional deformation

Assumption

- Process building parameters are assumed to be under control first in the study. That is, the bending deformation pattern still exists and thus the error compensation is needed and can be applied through changes to the CAD models.
- The layer area used in the compensation model is assumed to be approximated based on the weight value of each layer, the volume of the part sample, and the layer thickness. That is, the density of the vertices used in the analysis depends on the density of triangles of the STL file.
- The bending deformation is found to be convex and thus is assumed (found) in the SLS platform, which follows the polynomial regression form (e.g., quadratic) in the analysis. However, other technological platforms will need further validation.
- A medium-to-large sized part with typical complexity is assumed and thus tested in the study. That is a miniature scaled part and /or with a high number of holes needs to be further validated. Additionally, a part with specific geometric features, such as thin plates, rods, or highly curved surfaces is left for further investigation.

4.2.2 Regression Model for Representing Deformation Patterns

I discuss the general quadratic regression model and the proposed compensation model in Section 4.2.2. The schematic compensation framework is illustrated in Figure 4-1. As the 3D printed samples are found to have convex bending deformations, it is important to modify the CAD model based on the z-directional error value so that these convex deformations can be estimated, and the compensated part has better dimensional accuracy. A quadratic regression model is used for this purpose in the x and y coordinates as follows. While Eq. (4-2) illustrates the general quadratic regression model for the part based on the bending deformation in the x-direction, Eq. (4-3) similarly shows the model in the y-direction. I note that the coefficient *'a'* controls the degree of curvature of the function such that $a > 0$, implying that the curvature is upward, while $a < 0$ suggests a downward curvature. Additionally, a larger magnitude of coefficient *'a'* suggests that a sharply curved shape appears. The coefficients *'b'* and *'c'* then control the location of the symmetry and the height of the curvature, respectively.

Curvature in the x-direction $$Z_x = a_x X^2 + b_x X + c_x \quad \textbf{4-2}$$

Curvature in the y-direction $$Z_y = a_y Y^2 + b_y Y + c_y \quad \textbf{4-3}$$

The quadratic function in the standard form (Eq. (4-2) and (4-3)) is then transformed to the vertex form so that the centroid or the center of mass of each function can be used. Thus, the curvature in the z-direction representing the bending deformation is simplified to capture both the curvature in the x and y directions as shown in Eq. (4-4). While the second-order coefficient *'a'* explicitly presents the

direction of the curvature, the first-order coefficient *'b'* and coefficient *'c'* are implicit in the transformed equation.

Curvature in the z-direction $a_x \times (Xi - LCPX)^2 + a_y \times (Yi - LCPY)^2$ **4-4**

Next, the point-based compensation model can be developed based on the bending pattern of dimensional deformation as shown in Eq. (4-5). I note that Eq. (4-5) holds true for both the convex ($a > 0$) and concave ($a < 0$) pattern of bending deformation.

$$Z_0 = Z_i - \{a_{xl} \times (X_i - LCPX)^2 + a_{yl} \times (Y_i - LCPY)^2\} \quad \textbf{4-5}$$

where:

- *Zo: Vertex data of the Z values for the compensated CAD file,*
- *Xi, Yi, Zi: Vertex data of the X, Y, and Z values of each vertex i for the original CAD file,*
- *$LCPX$: The X value of the centroid of each layer,*
- *$LCPY$: The Y value of the centroid of each layer.*

The model for compensation of the dimensional deformation from the bending pattern is applied to both the x and y directions, where the corresponding coefficients are substituted into the proposed model. The center of curvature is calculated using the centroid of each layer. In this model, the layer centroid X (LCPX) and the layer centroid Y (LCPY) are used as the center of curvature. They are calculated using Eq. (4-6) and (4-7). The LCPX and LCPY for each layer are calculated based on all the *n* vertices associated with total triangles under consideration (i.e., all triangles in a layer in this case). I note that the $\left\lceil \frac{i}{3} \right\rceil$ symbol is used to represent the ceiling of $\frac{i}{3}$ (i.e., the smallest integer greater than or equal to $\frac{i}{3}$) so that the same weight will be applied to each triangle. For example, w_1 will be applied to all vertices i = 1, 2, and 3 associated with the first triangle and so on.

$$LCPX = \frac{\sum_{i=1}^{n} x_i * w_{\left\lceil \frac{i}{3} \right\rceil}}{\sum_{i=1}^{n} w_{\left\lceil \frac{i}{3} \right\rceil}} \quad \textbf{4-6}$$

$$LCPY = \frac{\sum_{i=1}^{n} y_i * w_{\left\lceil \frac{i}{3} \right\rceil}}{\sum_{i=1}^{n} w_{\left\lceil \frac{i}{3} \right\rceil}} \quad \textbf{4-7}$$

where

- *x_i and y_i: X and Y values of the vertex data for each vertex i,*
- *w_i: The weight associated with each vertex i.*

I further discuss the compensation steps (Steps 8.1 – 8.4 (Figure 4-6)) as follows. First, the weight of each vertex is calculated using the formula for calculating the triangle area. Second, the center point (centroid) of each layer and layer area are calculated. Third, the moving average is calculated for smoothing the overall surface of the part and for reducing the stair-stepping error (staircase effect). Fourth, the CAD model is compensated using the layer centroid, the layer area, and the height of each layer. In the compensation model, each layer l is divided by the height value (i.e., z value) and the center point in the layer l is the average value of the x and y values with associated weights for each point. The weight w is used because the STL file is composed of different triangles and these triangles have different sizes, which make the density of vertices different. Thus, I used the concept of weight to account for this aspect. The weight for any triangle i is calculated by the vector cross product (Eq. (4-8)). Since the STL file format provides information with three-vertex data, I can obtain the two-vector data using Eq. (4-9) and (4-10). Figure 4-7 illustrates the three-vertex data (t_{3i-2}, t_{3i-1}, t_{3i}) with two vector data ($\overrightarrow{a_i}$ and $\overrightarrow{b_i}$) for any triangle i.

$$w_i = \frac{1}{2}|\overrightarrow{a_i} \times \overrightarrow{b_i}| \quad \textbf{4-8}$$

$$\overrightarrow{a_i} = t_{3i-1} - t_{3i-2} \quad \textbf{4-9}$$

$$\overrightarrow{b_i} = t_{3i} - t_{3i-2} \quad \textbf{4-10}$$

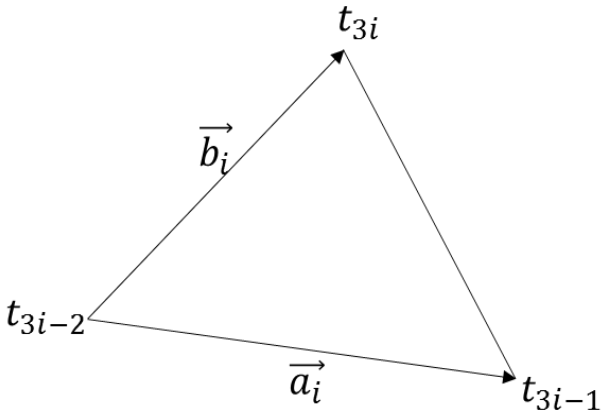

Figure 4-7 Vector cross product based on the STL file

I note that the weight of each vertex is illustrated using $w_{\lceil \frac{i}{3} \rceil}$ in Eq. (4-6) and (4-7) because each triangle is formed from three vertices and these vertices are assigned the same weights in the same triangle. That is, the first triangle is formed from three points (*P1, P2,* and *P3*), the second triangle is then formed from another three points (*P4, P5,* and *P6*), where two points in the second triangle are shared with the first triangle. This process continues until the last triangle is formed from points *P(3n-*

2), P(3n-1), and *P(3n).* Figure 4-8 (a) illustrates the idea with one triangle and Figure 4-8 (b) shows two triangles with two shared points. As seen in Figure 4-8 (a) with one triangle, the center point of each layer (LCPX and LCPY) can then be calculated as shown in Eq. (4-11) and (4-12).

$$LCPX = \frac{x_1 \times w_1 + x_2 \times w_1 + x_3 \times w_1}{w_1 + w_1 + w_1} \quad \textbf{4-11}$$

$$LCPY = \frac{y_1 \times w_1 + y_2 \times w_1 + y_3 \times w_1}{w_1 + w_1 + w_1} \quad \textbf{4-12}$$

Similarly, Eq. (4-13) and (4-14) show how the LCPX and LCPY can be calculated when there are two triangles with two shared points (Figure 4-8 (b)).

$$LCPX = \frac{(x_1 \times w_1 + x_2 \times w_1 + x_3 \times w_1) + (x_4 \times w_2 + x_5 \times w_2 + x_6 \times w_2)}{(w_1 + w_1 + w_1) + (w_2 + w_2 + w_2)} \quad \textbf{4-13}$$

$$LCPY = \frac{(y_1 \times w_1 + y_2 \times w_1 + y_3 \times w_1) + (y_4 \times w_2 + y_5 \times w_2 + y_6 \times w_2)}{(w_1 + w_1 + w_1) + (w_2 + w_2 + w_2)} \quad \textbf{4-14}$$

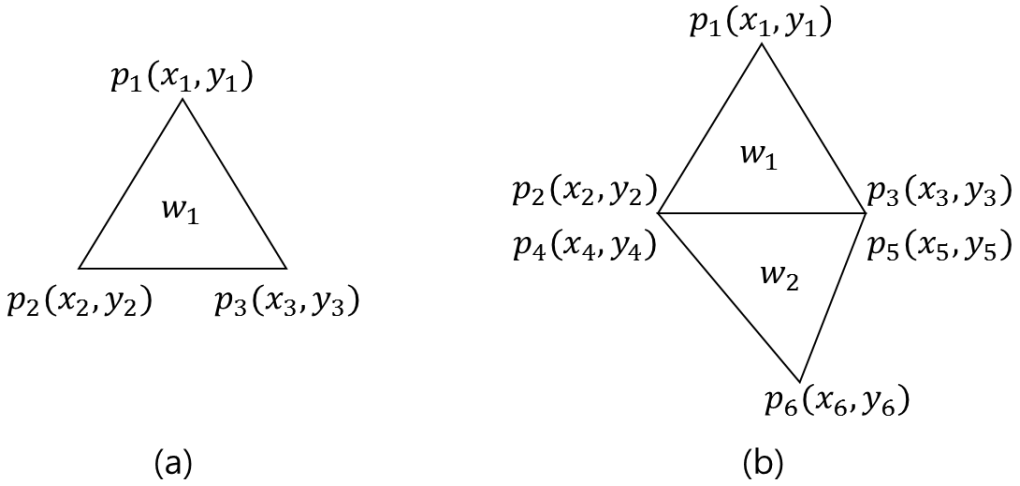

Figure 4-8 LCPX and LCPY calculation examples for a) one triangle, b) two triangles

Next, to obtain the value of the quadratic gradient *'a'* of each layer, representing the degree of curvature, the sample's layer area, and height need to be calculated. As discussed earlier, an increase in the absolute value of the quadratic gradient *'a'* implies that the curvature is more sharply curved. Additionally, I observed that the quadratic gradient *'a'* increases when a particular layer area is much higher than the others. It is likely that if the layer area becomes larger, the residual stress between an upper and a lower layer can possibly be higher due to the contraction from phase transition (i.e., when powders are sintered, they become viscoelastic material and elastic).

The layer area (S_l) can be calculated using Eq. (4-15) based on the total weight assigned for all triangles of the layer, total weight assigned for all triangles of the part sample, volume of the part

sample (v), and layer depth (d). As discussed earlier, the weight (w) is used to account for the different densities of the vertices in the STL file because it contains triangles of varied size. As seen in Eq. (4-15), the multiplication by three is used in the denominator term, $3 \times \sum_{i=1}^{n} w_i$, as points *P(3n-2), P(3n-1),* and *P(3n)* all have the same weight (w_n). To illustrate the weight analysis, suppose that the layer of interest simply contains two triangles from the ten triangles of the whole part. It follows that the numerator term, $\sum_{i=1}^{n} w_{\lceil \frac{i}{3} \rceil}$, is $(w_1 + w_1 + w_1) + (w_2 + w_2 + w_2)$ for n=2; whereas the denominator term, $3 \times \sum_{i=1}^{n} w_i$, becomes $3 * (w_1 + w_2 + \cdots + w_{10})$ for n=10.

$$S_l = \frac{Total\ weight\ assigned\ for\ all\ trinalges\ of\ the\ layer}{Total\ weight\ assigned\ for\ all\ triangles\ of\ the\ part\ sample} * \frac{Volume\ of\ the\ part\ sample}{Layer\ depth} = \frac{\sum_{i=1}^{n} w_{\lceil \frac{i}{3} \rceil}}{3 \times \sum_{i=1}^{n} w_i} * \frac{v}{d} \quad \textbf{4-15}$$

Thus, the volume of layer l can be approximated by multiplying the ratio of the weight value of layer l by the total volume of sample (v). Next, the layer area (S_l) can be calculated by dividing the volume of layer l by the thickness of each layer (d). I observe that when the calculated centroid and area of one particular layer are very different to the others, the surface between layers is found to be quite rough. Thus, the five-sample moving average filter is used in this model to smooth out short-term fluctuations of data (i.e., centroid of each layer and layer area) for all layers of the part. In particular, the moving average technique is used to analyze data points by creating a series of averages of different subsets (i.e., five samples in this study) of the full data set. I find that the five-sample moving average in this study can smooth the overall surface of the part and reduce the stair-stepping error (staircase effect) between layers.

The patterns of deformation from different AM printers may cause some differences. Therefore, in this study, I fabricated the reference samples shown in Figure 3-16 and extracted the quadratic gradients of the deformation patterns from sPro60 SLS machines by 3D systems. Eq. (4-16) and (4-17) illustrate the quadratic gradient equations extracted by the reference samples used in this study. I note that different AM processes may exhibit different geometrical characteristics.

$$a_{xl} = 1.3 \times (0.00005 + S_l) \times \left(z_{Top} - z_i\right) \times 1.8125 \times 10^{-10} \quad \textbf{4-16}$$

$$a_{yl} = (0.00005 + S_l) \times \left(z_{Top} - z_i\right) \times 1.8125 \times 10^{-10} \quad \textbf{4-17}$$

5. A case study of a deformation compensation framework

5.1 Tail lamp

I tested the compensation framework with a real vehicle component using a tail lamp part. The tail lamp or tail light is a complicated part of the lighting system of a vehicle attached at the rear part of the vehicle. The compensation framework discussed in Section 4.2 is used in this Chapter in a similar way to the previous sample part experiments. Initially, two tail lamps were made: one was based on the original CAD model and the other was based on the compensated CAD model. To compare these two parts, the 3D scanner was used to measure dimensional data. I ran this test on two 3D printers (sPro 60 and sPro230) and ran Geometric Dimensioning and Tolerancing and scan tests, respectively. The program used for each test was programmed through Matlab®. Please refer to the appendix for a detailed code of the compensation program.

5.1.1 Geometric Dimensioning and Tolerancing (GD & T) test for the tail lamp (sPro60)

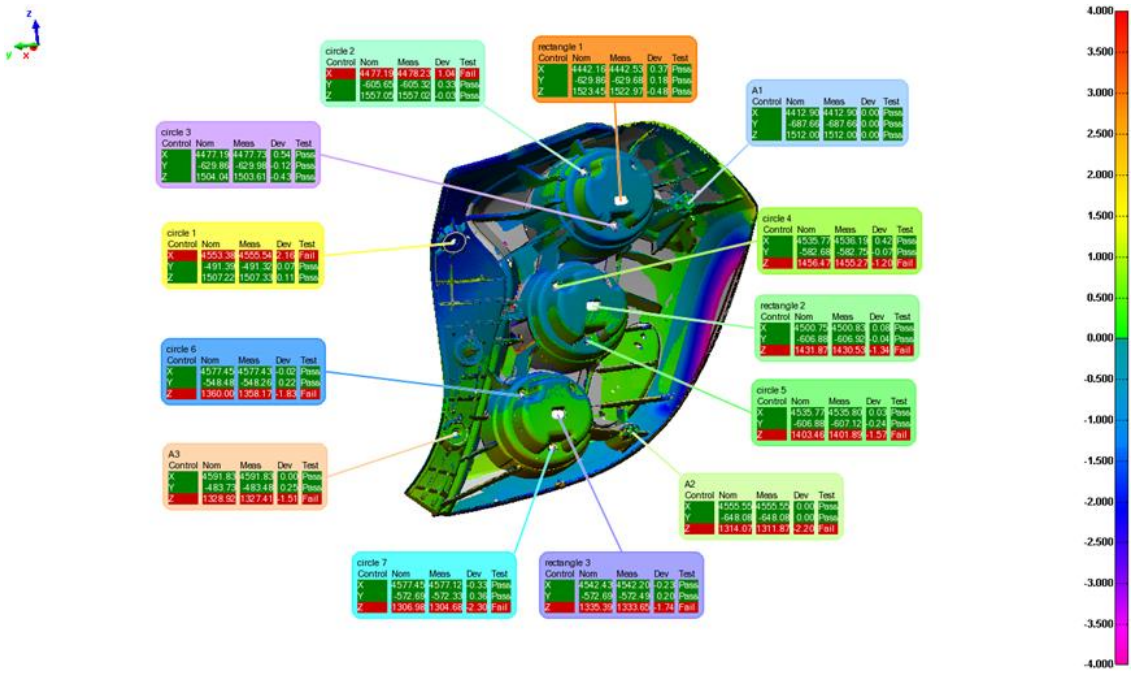

Figure 5-1 Original CAD model result

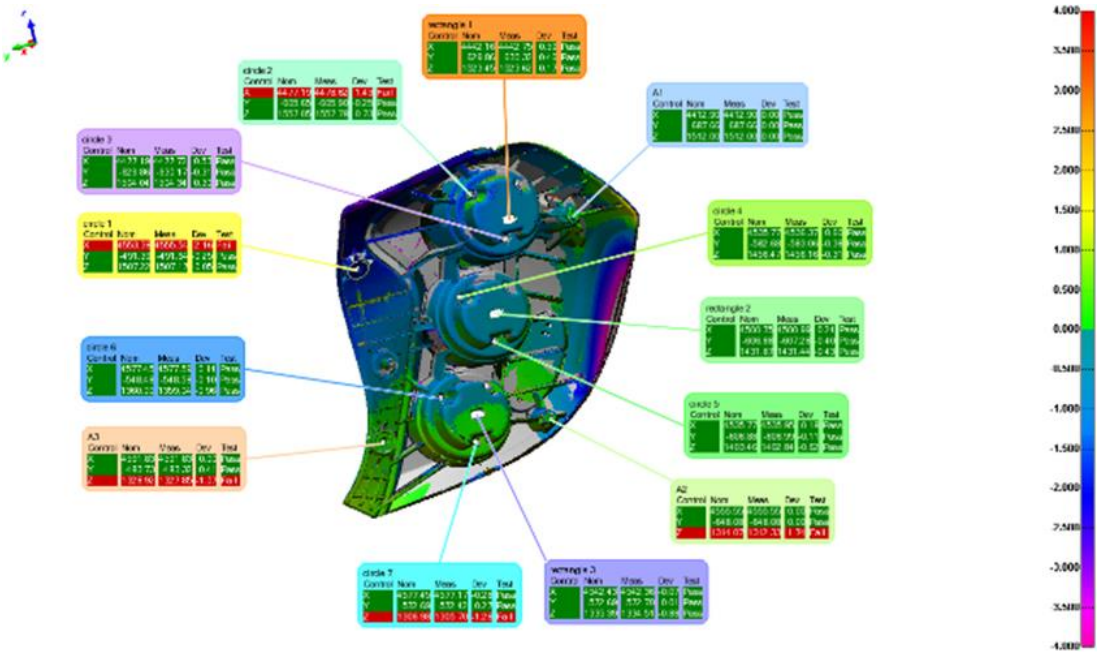

Figure 5-2 Compensated CAD model result

Table 5-1 sPro60 GD&T TEST result

Error	S0 (original)			S2 (compensated)		
Unit: mm	X	Y	Z	X	Y	Z
Circle 1	2.16	0.07	0.11	2.16	-0.25	-0.05
Circle 2	1.04	0.33	-0.03	1.43	-0.25	0.73
Circle 3	0.54	-0.12	-0.43	0.53	-0.31	0.30
Circle 4	0.42	-0.07	-1.20	0.60	-0.38	-0.31
Circle 5	0.03	-0.24	-1.57	0.18	-0.11	-0.62
Circle 6	-0.02	0.22	-1.83	0.14	-0.10	-0.96
Circle 7	-0.33	0.36	-2.30	-0.28	0.27	-1.28
A 1	0.00	0.00	0.00	0.00	0.00	0.00
A 2	0.00	0.00	-2.20	0.00	0.00	-1.74
A 3	0.00	0.25	-1.51	0.00	0.41	-1.07
Rectangle 1	0.37	0.18	-0.48	0.59	-0.46	0.17
Rectangle 2	0.08	-0.04	-1.34	0.24	-0.40	-0.43
Rectangle 3	-0.23	0.20	-1.74	-0.07	-0.01	-0.88
Abs Average	0.40	0.16	1.13	0.48	0.23	0.66

Table 5-2 sPro60 TEST T-test result

	P-VALUE	AVERAGE	STDEV
S0_X Dev	**0.077**	0.402	0.607
S2_X Dev		0.478	0.640
S0_Y Dev	**0.222**	0.160	0.120
S2_Y Dev		0.227	0.166
S0_Z Dev	**0.006**	1.134	0.827
S2_Z Dev		0.657	0.518

As shown in Figure 5-1 and Figure 5-2 and Table 5-1, I can confirm that 10 out of 13 reference points generated spec out (tolerance: 1mm) before applying the compensation model. However, applying the compensation model, only 5 out of 13 points resulted in spec out. It can be confirmed that the z value had a large error especially when the sample was made using the original file. Therefore, it can be seen that the spec out data was reduced by about 60% from 8 to 3 when only z-axis data were compared. As shown in Table 5-2, significant improvements were found especially in the z-direction. Through this framework, it is possible to mitigate the constraints that arise when arranging samples. Therefore, the flexibility of the manufacturing system can be ensured, and the sample preparation time and cost can be reduced.

5.1.2 Scan test for the tail lamp (sPro230)

Figure 5-3 illustrates the scanning images of both the original and the compensated CAD models of tail lamps. I then summarize the error values associated with the scanned data between the two in Table 5-3.

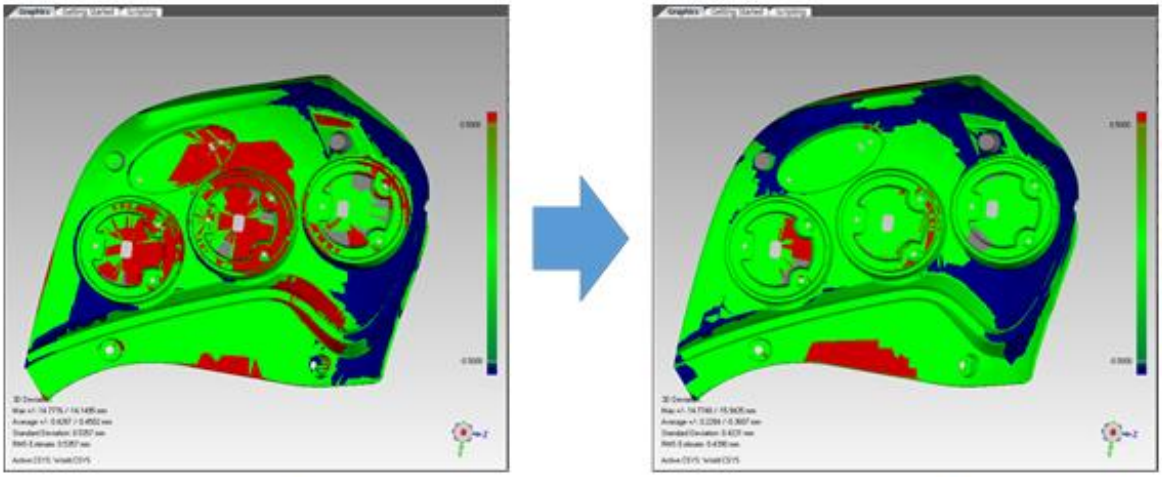

Figure 5-3 A scan data of the original and compensated CAD models of the tail lamp part

Table 5-3 The error values of the tail lamp part between original and compensated CAD models

CAD model vs. printed part	*Average Distance*		*Standard Deviation*	*RMS Estimate*
	Positive	Negative		
Compensated (C)	0.228	-0.361	0.423	0.439
Original (O)	0.429	-0.45	0.536	0.536
O-C	0.2	-0.09	0.113	0.097
(O-C)/O	0.467	0.199	0.21	0.181

Note: RMS denotes Root Mean Square

As the tail lamp used in this validation process is a real vehicle part, the dimensional tolerance is an important factor to be considered. After discussion with the automotive company staff, the dimensional tolerance suggested for the study was set at ±0.5 millimeters and I used this tolerance value as a basis to test the effectiveness of the compensation model by comparing the amount of sampling data that exceeded the tolerance limit between the original and the compensated models. As

shown in Figure 5-3, while the tail-lamp part fabricated by the original CAD model contains 39% of data that exceeds the tolerance limit, the part fabricated based on the compensated CAD model has 19% of data that exceeds the tolerance limit. This accounts for a 25 % improvement using the compensation model.

Table 5-3 presents the error values of data to compare the application of the compensation model (C) and the original data (O) without the application of the compensation model. I calculated the average distance (both positive and negative), the standard deviation (SD), and the root means square (RMS) estimate in Table 5-3. The positive average distances (i.e., the 3D printed sample is larger than the CAD model) and negative average distances (i.e., the 3D printed sample is smaller than the CAD model) values were improved by around 47% and 20%, respectively. In addition, the SD of the scanned data was improved by 21% and the RMS estimate for the dimensional accuracy was improved by 18% when the compensation model was applied.

I further conducted a statistical analysis by randomly collecting 34 sampling data for both the original and the compensated CAD model when the compensation model was applied. After all the sampling data were collected, a paired t-test was used to analyze them. The p-value of 0.018 indicates that there was a significant difference when the compensation framework was applied. The proposed compensation framework was found to be effective and can be used as a pre-processor for production of 3D printed parts with higher accuracy.

5.2 Front lamp

In order to compare the results of the other samples, Figure 5-4 shows the results of the scan on the right front lamp of the vehicle made in January 2017. The tendency of the scan result on the left front lamp is also the same as the result of the right front lamp. I used the original CAD data and compensated CAD data to fabricate 2 left front lamps and 2 right front lamps. The 3D printer was sPro230, and various parameter values are at the default value.

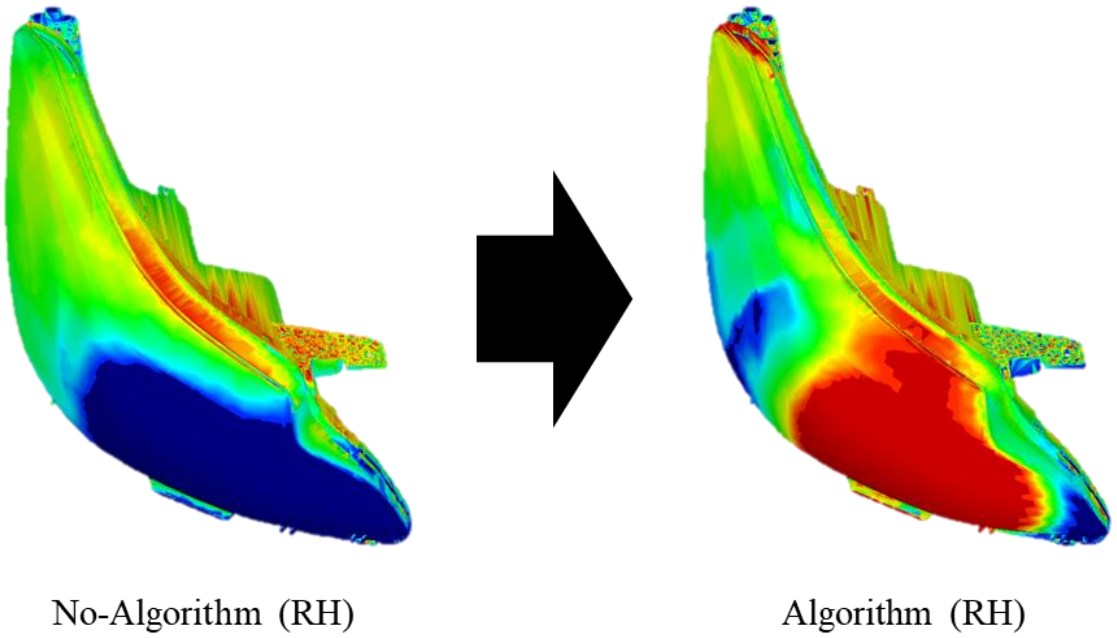

Figure 5-4 The scan test result of the right front lamp

Table 5-4 The scan test result of the right front lamp

RH/LH	AL/NO-AL	RMS ERROR
LH	Compensated	**0.8686**
	Original	**0.9625**
RH	Compensated	**0.8739**
	Original	**1.0032**

Figure 5-4 shows that the scan result changes from blue to red at the bottom of Figure 5-4. That means the degree of compensation is excessive. For 3D printers, it is necessary to periodically replace the lens, and the scale factor is compensated at that time. That is, there is a pattern of deformation, but the degree of deformation can be changed by a lens replacement or the like. Therefore, it is expected that the compensation operation is over-developed. To solve this problem, it is necessary to calibrate the scale factor value such as the count value of the compensation model during the calibration operation. Nevertheless, as shown in Table 5-4, the RMS values show that the overall dimensional

accuracy is better than before. It can be confirmed that both the right and left sides are improved by about 10%. From these results, I confirmed that the compensation model can mitigate the deformation.

5.3 Summary of compensation framework

Based on the data obtained in Section 3.2.2, I made a simple model using the average of the amount of bending deformation of the top and bottom of the samples and the center point of each layer. The effect of the compensation model was confirmed by applying the model to the samples. In order to confirm the reproducibility, I confirmed the reproducibility of the deformation measurement result after re-manufacturing the samples by using the CAD file applying the compensation model.

Then, based on the data obtained in Section 3.2.3, a compensation model applicable to samples of complex shapes rather than a simple structure is presented. This model relaxes the deformation by predicting the deformation using the center point of each layer of the sample and the area of each layer. In order to verify the compensation model applicable to this complex shape sample, I applied it to the front lamp and tail lamp CAD models of the actual vehicle and compared them with the samples made with the original CAD model. As a result, it was confirmed that the dimension was improved. However, as the degree of deformation changes over time, it was confirmed that a periodic compensation model calibration is needed to compensate for the variation of the amount of bending deformation.

6. Conclusion and Further works

6.1 Summary

In Chapter 3, a model to predict the deformation of AM part was proposed by analyzing the densification of raw material in SLS. And it was confirmed that the degree of deformation shows a tendency similar to the density difference according to the energy density. In addition, I analyzed the differences in deformation dependent on the production layout and the shape. Even with minor disparities between 3D printers, the differences in deformation according to the position were still verified. The printed product from sPro60, in particular, showed a more severe bending deformation in the bottom portion. It was also confirmed that the contraction and deformation degree varied according to the layout position. The analysis of the cause of deformation in the final product showed that the humidity had a great influence.

In Chapter 4, an experimental design was conducted to investigate the dimensional deformation of 3D printed samples based on different factors including the x, y, and z directions; the bending deformation between the top and bottom surface of each part; and the part locations for both upper and lower locations of the SLS's build chamber. A quadratic polynomial regression model was then used to analyze the deformation patterns and it was found that the quadratic function representing the bending deformation in the negative direction to the original CAD files can be used in the compensation model to minimize such deformation. The modified CAD files with the compensation model were statistically analyzed by conducting a paired t-test to compare the samples before and after compensation. The statistical results confirmed that the proposed compensation model is an effective countermeasure against the bending deformation of the printed samples.

In Chapter 5, I provided a practical case study using the compensation model with a real vehicle part. The compensation framework was shown to provide a more effective solution to the dimensional deformation of printed products, which is not manageable by simply using the scale factor provided by SLS manufacturers. As a result of comparing several samples before and after applying the frameworks using other 3D printers, I confirmed that various 3D printers can improve the dimensional accuracy of various samples by using this method.

6.2 Research contribution

The selective laser sintering process (SLS) is one additive manufacturing technique that is popular and well-known to enhance a product's engineering properties and durability in the auto part development process.

However, a limitation of the SLS process is the dimensional inaccuracy from thermo-mechanical deformation. Current approaches mentioned in the literature and countermeasures taken by printer manufacturers to solve dimensional deformation are systematic, thus, constrained; practical approach lacks. There are few analytical studies on the cause of bending deformation, but none for the compensation method. As a numerical expression of the degree of bending is feasible, I primarily used the regression model to numerically express the bending deformation. This work presents a method of representing the degree of bending deformation by using the regression model coefficient value.

In addition, manuals can be provided to improve dimensional accuracy and to minimize deformations. For example, in order to improve the dimensional accuracy as well as the density of the sample, manufacturers should increase the laser power and the thickness of the layer or modify the production layout. It is recommended to test this process with the same humidity for sample management and measurement. A method to minimize deformation and minimize bending deformation is also proposed.

The compensation model can be used to further improve dimensional accuracy, while also reducing post-processing costs and time. In addition, the compensation framework allows more space for fabrication of 3D printed parts in the part bed, allowing more samples to be placed. Therefore, the production costs and time are also reduced. The compensation model was used by a real vehicle company and the result was also positive. That is, it can be practically used in the industrial field and its advantages are also confirmed.

Through these processes, the improvement of the dimensions can be achieved, which means a reduction of the cost or time required to make parts using AM. In addition, from the case studies, the applications of AM have been confirmed. For example, these positive effects were verified not only for front-lamp and tail-lamps as mentioned in Chapter 5, but also for emblems and cup holders. To conclude, since the manufacturing precision of AM can be improved, it will be possible to more actively implement the advantages of AM: the fabrication of molds for the manufacture of parts in the development of new vehicles and the manufacturing of pieces for the repair of discontinued vehicles.

6.3 Research limitation & further works

In the case of the deformation prediction method, the difference in control variable values was not sufficient to obtain statistically significant results. Therefore, it is likely that further experimentation will be needed in which the difference in control variable values is increased. For more accurate verification of the mathematical model of densification deformation, further experiments are needed to find the constant values in the elastic modulus. In addition, research is also needed on the effect of other parameters used in energy density calculations. To promote the new industrial applications of additive manufacturing, many quality and reliability issues considering safety and use conditions should be investigated. Thus, in the future, dynamic material properties and the lifetime of the printed parts under severe and realistic use conditions need to be studied.

There are difficulties in obtaining additional data due to the limited amount of studies on deformation with respect to the position of the placement. For this reason, the deformation pattern analysis mainly covers the explanation of the pattern without touching much on its cause. To remedy this, further research is needed.

Whilst the proposed compensation framework was also found to be effective in remedying the bending deformation, its impact on other deformation patterns, such as contraction on the x and y directions should be further investigated. This will further maximize the effect of dimensional improvement. In addition, as multi-material AM components are gaining interest from various industries, future research should test the compensation model with multiple materials.

These works are expected to be applied to metal AM processes by adding deformation according to the residual stress change when support structures are removed. As the accuracy of the simulation improves, time and cost can be saved for the use of industrial applications. In addition, as the accuracy of the deformation simulation increases, the CAD model shown in the preliminary study can be modified in the direction opposite to the deformed direction before fabrication to improve the dimensional accuracy.

References

Ahmed, R. (2017). Why Atomic Diffusion Additive Manufacturing is a Game-changer. In: 3D PRINTING.COM.

Alexandrea, P. (2017). The Complete Guide to Electron Beam Melting 3D Printing (EBM), 3Dnatives your source for 3D printing. In: 3D natives your source for 3D printing.

ASTM. (2012). Additive manufacturing - General prinicples - Terminology. In (Vol. ISO/ASTM 52900:2015).

Attaran, M. (2017). The rise of 3-D printing: The advantages of additive manufacturing over traditional manufacturing. *Business Horizons, 60*(5), 677-688. doi:https://doi.org/10.1016/j.bushor.2017.05.011

Beal, V. E., Paggi, R. A., Salmoria, G. V., & Lago, A. (2009). Statistical evaluation of laser energy density effect on mechanical properties of polyamide parts manufactured by selective laser sintering. *Journal of Applied Polymer Science, 113*(5), 2910-2919. doi:10.1002/app.30329

Beer, F., Jr. Johnston, E. R., DeWolf, J., & Mazurek, D. (2008). *Mechanics of Materials*: McGraw-Hill Companies,Incorporated.

Beyer, C. (2014). Strategic Implications of Current Trends in Additive Manufacturing. *Journal of Manufacturing Science and Engineering, 136*(6), 064701. doi:10.1115/1.4028599

Bourell, D. L., Watt, T. J., Leigh, D. K., & Fulcher, B. (2014). Performance Limitations in Polymer Laser Sintering. *Physics Procedia, 56*, 147-156. doi:https://doi.org/10.1016/j.phpro.2014.08.157

Cadoni, E., Labibes, K., Albertini, C., Berra, M., & Giangrasso, M. (2001). Strain-rate effect on the tensile behaviour of concrete at different relative humidity levels. *Materials and Structures, 34*(1), 21--26.

Caulfield, B., McHugh, P. E., & Lohfeld, S. (2007). Dependence of mechanical properties of polyamide components on build parameters in the SLS process. *Journal of Materials Processing Technology, 182*(1), 477-488. doi:https://doi.org/10.1016/j.jmatprotec.2006.09.007

Chen, T.-C., Chang, C.-J., Hung, J.-P., Lee, R.-M., & Wang, C.-C. (2016). Real-Time Compensation for Thermal Errors of the Milling Machine. *Applied Sciences, 6*(4), 101. doi:10.3390/app6040101

Chen, X., Zhou, L., & Li, G. (2010, 11-12 May 2010). *Finite Element Based Dimension Deformation Predication and Anti-deformation Compensation Model for Composite Part.* Paper presented at the 2010 International Conference on Intelligent Computation Technology and Automation.

Choi, S.-K. (2014). 3D printing technology and architectural application. *Review of Architectural Institute of Korea, 58*(2), 17-25.

Despa, V., & Gheorghe, I. G. (2011). Study of selective laser sintering: a qualitative and objective approach. *Scientific Bulletin of Valahia University Materials Mechanics, 6*, 150-155.

Edwards, P., O'Conner, A., & Ramulu, M. (2013). Electron Beam Additive Manufacturing of Titanium Components: Properties and Performance. *Journal of Manufacturing Science and Engineering, 135*(6).

Fernlund, G., Osooly, A., Poursartip, A., Vaziri, R., Courdji, R., Nelson, K., . . . Griffith, J. (2003). Finite element based prediction of process-induced deformation of autoclaved composite structures using 2D process analysis and 3D structural analysis. *Composite Structures, 62*(2), 223-234. doi:10.1016/S0263-8223(03)00117-X

Gao, W., Zhang, Y., Ramanujan, D., Ramani, K., Chen, Y., Williams, C. B., . . . Zavattieri, P. D. (2015). The status, challenges, and future of additive manufacturing in engineering. *Computer-Aided Design, 69*, 65-89.

Gardan, J. (2015). Additive manufacturing technologies: state of the art and trends. *International Journal of Production Research, 54*(10), 1-15. doi:10.1080/00207543.2015.1115909

Gasik, M., & Zhang, B. (2000). A constitutive model and FE simulation for the sintering process of powder compacts. *Computational Materials Science, 18*(1), 93-101. doi:10.1016/S0927-

0256(00)00090-2

German, R. M. (1984). *Powder metallurgy science* (1st ed.). Princeton, NJ: Metal Powder Industries Federation.

Gibson, I. (2010). *Additive Manufacturing Technologies Rapid Prototyping to Direct Digital Manufacturing*: Boston, MA : Springer US : Imprint: Springer.

Gibson, L. J., & Ashby, M. F. (1999). *Cellular Solids: Structure and Properties* (2nd ed. ed.): Cambridge University Press.

Goodridge, R. D., Tuck, C. J., & Hague, R. J. M. (2012). Laser sintering of polyamides and other polymers. *Progress in Materials Science, 57*(2), 229-267. doi:https://doi.org/10.1016/j.pmatsci.2011.04.001

Gou, G., Zhang, M., Chen, H., Chen, J., Li, P., & Yang, Y. P. (2015). Effect of humidity on porosity, microstructure, and fatigue strength of A7N01S-T5 aluminum alloy welded joints in high-speed trains. *Materials & Design, 85*, 309--317.

Gu, D., & Shen, Y. (2009). Effects of processing parameters on consolidation and microstructure of W–Cu components by DMLS. *Journal of Alloys and Compounds, 473*(1), 107-115. doi:10.1016/j.jallcom.2008.05.065

Guo, N., & Leu, M. C. (2013). Additive manufacturing: technology, applications and research needs. *Frontiers of Mechanical Engineering, 8*(3), 215-243.

Ha, S., Han, H., Kwon, D., Kim, N., Kim, H., Hwang, C., . . . Park, K. (2015). *Systematic Dimensional Calibration Process for 3D Printed Parts in Selective Laser Sintering (SLS).* Paper presented at the ASME 2015 International Design Engineering Technical Conferences and Computers and Information in Engineering Conference, Boston, Massachusetts, USA.

Ha, S., Ransikarbum, K., Han, H., Kwon, D., Kim, H., & Kim, N. (2018). A dimensional compensation algorithm for vertical bending deformation of 3D printed parts in selective laser sintering. *Rapid Prototyping Journal*. doi:doi:10.1108/RPJ-12-2016-0202

Ha, S., Ransikarbum, K., & Kim, N. (2016). *Phenomenological deformation patterns of 3D printed products in a selective laser sintering process.* Paper presented at the the 18th International Conference on Industrial Engineering.

Haffane, N., Benameur, T., & Vergnaud, J. M. (1997). Hardness variation of a thermoset in contact with a liquid. *Polymer Testing, 16*(3), 259-270. doi:10.1016/S0142-9418(96)00046-3

Han, J. Y. (2013). A study on the Prototype Modeling Method using 3D Printing. *Journal Packaging Culture Design Research, 34*, 97.

Hopkinson, N., & Sercombe, T. B. (2008). Process repeatability and sources of error in indirect SLS of aluminium. *Rapid Prototyping Journal, 14*(2), 108-113. doi:10.1108/13552540810862073

Huang, Q. (2016). An Analytical Foundation for Optimal Compensation of Three-Dimensional Shape Deformation in Additive Manufacturing. *Journal of Manufacturing Science and Engineering, 138*(6), 061010. doi:10.1115/1.4032220

Huang, Q., Nouri, H., Xu, K., Chen, Y., Sosina, S., & Dasgupta, T. (2014). Statistical Predictive Modeling and Compensation of Geometric Deviations of Three-Dimensional Printed Products. *Journal of Manufacturing Science and Engineering, 136*(6), 061008. doi:10.1115/1.4028510

Huang, Q., Zhang, J., Sabbaghi, A., & Dasgupta, T. (2015). Optimal Offline Compensation of Shape Shrinkage for 3D Printing Processes. *IIE Transactions, 47*(5), 00-00. doi:10.1080/0740817X.2014.955599

Islam, M. N., Boswell, B., & Pramanik, A. (2013). *An Investigation of Dimensional Accuracy of Parts Produced by Three-Dimensional Printing.* Paper presented at the Proceedings of the World Congress onEnineering, London, U.K.

Islam, M. N., & Sacks, S. (2016). An experimental investigation into the dimensional error of powder-binder three-dimensional printing. *The International Journal of Advanced Manufacturing Technology, 82*(5), 1371-1380. doi:10.1007/s00170-015-7482-7

Jin, S., Liu, C., Lai, X., Li, F., & He, B. (2017). Bayesian network approach for ceramic shell deformation fault diagnosis in the investment casting process. *The International Journal of Advanced Manufacturing Technology, 88*(1), 663-674. doi:10.1007/s00170-016-8795-x

Jin, Y., Qin, S. J., & Huang, Q. (2015, 24-28 Aug. 2015). *Out-of-plane geometric error prediction for additive manufacturing.* Paper presented at the 2015 IEEE International Conference on

Automation Science and Engineering (CASE).
Kim, H., Gillia, O., & Bouvard, D. (2003). A phenomenological constitutive model for the sintering of alumina powder. *Journal of the European Ceramic Society, 23*(10), 1675-1685. doi:https://doi.org/10.1016/S0955-2219(02)00411-9
Ko, H., Moon, S., & Hwang, J. (2015). Design for additive manufacturing in customized products. *International Journal of Precision Engineering and Manufacturing, 16*(11), 2369-2375. doi:10.1007/s12541-015-0305-9
Kruth, J.-P. (1991). Material incress manufacturing by rapid prototyping techniques. *CIRP Annals-Manufacturing Technology, 40*(2), 603-614.
Kwon, D., Park, E., Ha, S., & Kim, N. (2017). Effect of humidity changes on dimensional stability of 3D printed parts by selective laser sintering. *International Journal of Precision Engineering and Manufacturing, 18*(9), 1275-1280. doi:10.1007/s12541-017-0150-0
Lassila, L. V. J., Nohrström, T., & Vallittu, P. K. (2002). The influence of short-term water storage on the flexural properties of unidirectional glass fiber-reinforced composites. *Biomaterials, 23*(10), 2221-2229. doi:10.1016/S0142-9612(01)00355-6
Li, C., Liu, J. F., Fang, X. Y., & Guo, Y. B. (2017). Efficient predictive model of part distortion and residual stress in selective laser melting. *Additive Manufacturing, 17*, 157-168. doi:10.1016/j.addma.2017.08.014
Li, X., Birnbaum, J. C., Williford, R. E., Fryxell, G. E., Coyle, C. A., Dunham, G. C., & Baskaran, S. (2003). Effect of humidity treatments on porosity and mechanical integrity of mesoporous silica films. *Chemical Communications, 16*(16), 2054-2055. doi:10.1039/b304843h
Li, Y., Zhou, K., Tan, P., Tor, S. B., Chua, C. K., & Leong, K. F. (2018). Modeling temperature and residual stress fields in selective laser melting. *International Journal of Mechanical Sciences, 136*, 24-35. doi:https://doi.org/10.1016/j.ijmecsci.2017.12.001
Lindhe, U., & Harrysson, O. (2000). *Rapid Manufacturing with Electron Beam Melting (EBM)--A Manufacturing Revolution?* : Society of Manufacturing Engineers.
Liu, Y., Yang, Y., & Wang, D. (2016). A study on the residual stress during selective laser melting (SLM) of metallic powder. *The International Journal of Advanced Manufacturing Technology, 87*(1), 647-656. doi:10.1007/s00170-016-8466-y
Luan, H., & Huang, Q. (2015). *Predictive modeling of in-plane geometric deviation for 3D printed freeform products.* Paper presented at the 2015 IEEE International Conference on Automation Science and Engineering (CASE), Gothenburg, Sweden.
Mercelis, P., & Kruth, J.-P. (2006). Residual stresses in selective laser sintering and selective laser melting. *Rapid Prototyping Journal, 12*(5), 254-265. doi:10.1108/13552540610707013
Moodleah, S., Bohez, E. J., & Makhanov, S. S. (2016). Five-axis machining of STL surfaces by adaptive curvilinear toolpaths. *International Journal of Production Research, 54*(24), 7296-7329. doi:10.1080/00207543.2016.1176265
Nelson, J. (1993). *Selective laser sintering: A definition of the process and an empirical sintering model.* (PhD), The University of Texas,
Newman, S. T., Zhu, Z., Dhokia, V., & Shokrani, A. (2015). Process planning for additive and subtractive manufacturing technologies. *CIRP Annals - Manufacturing Technology, 64*(1), 467-470.
Olevsky, E. A. (1998). Theory of sintering: from discrete to continuum. *Materials Science and Engineering: R: Reports, 23*(2), 41-100. doi:10.1016/S0927-796X(98)00009-6
Palchik, V. (1999). Influence of Porosity and Elastic Modulus on Uniaxial Compressive Strength in Soft Brittle Porous Sandstones. *Rock Mechanics and Rock Engineering, 32*(4), 303-309. doi:10.1007/s006030050050
Park, J.-y., Ha, S., Park, E., Kwon, D., & Kim, N. (2016). *Hygroscopic Swelling Behavior of 3D Printed Parts due to Changes in Environmental Conditions.* Paper presented at the ASME 2016 International Design Engineering Technical Conferences and Computers and Information in Engineering Conference.
Park, J., Tari, M. J., & Hahn, H. T. (2000). Characterization of the laminated object manufacturing (LOM) process. *Rapid Prototyping Journal, 6*(1), 36-50. doi:10.1108/13552540010309868
Parthasarathy, J., Starly, B., Raman, S., & Christensen, A. (2010). Mechanical evaluation of porous

titanium (Ti6Al4V) structures with electron beam melting (EBM). *J Mech Behav Biomed Mater, 3*(3), 249-259. doi:10.1016/j.jmbbm.2009.10.006

Paul, R., & Anand, S. (2015). A combined energy and error optimization method for metal powder based additive manufacturing processes. *Rapid Prototyping Journal, 21*(3), 301-312. doi:10.1108/RPJ-07-2013-0065

Paul, R., Anand, S., & Gerner, F. (2014). Effect of Thermal Deformation on Part Errors in Metal Powder Based Additive Manufacturing Processes. *Journal of Manufacturing Science and Engineering, 136*(3), 031009. doi:10.1115/1.4026524

Ramos-Grez, J., Amado-Becker, A., José Yañez, M., Vargas, Y., & Gaete, L. (2008). Elastic tensor stiffness coefficients for SLS Nylon 12 under different degrees of densification as measured by ultrasonic technique. *Rapid Prototyping Journal, 14*(5), 260--270.

Sevostianov, I., Kováčik, J., & Simančík, F. (2006). Elastic and electric properties of closed-cell aluminum foams: Cross-property connection: Cross-property connection. *Materials Science & Engineering A, 420*(1-2), 87-99. doi:10.1016/j.msea.2006.01.064

Shinagawa, K. (1996). Finite element simulation of sintering process (Microscopic modelling of powder compacts and constitutive equation for sintering). *JSME international journal. Ser. A, Mechanics material engineering, 39*(4), 565-572.

Sidambe, A. (2014). Biocompatibility of Advanced Manufactured Titanium Implants-A Review. *Materials, 7*(12), 8168-8188. doi:10.3390/ma7128168

Sing, S. L., Wiria, F. E., & Yeong, W. Y. (2018). Selective laser melting of lattice structures: A statistical approach to manufacturability and mechanical behavior. *Robotics and Computer Integrated Manufacturing, 49*, 170-180. doi:10.1016/j.rcim.2017.06.006

Singh, R., & Singh, S. (2017). Additive Manufacturing: An Overview. In *Reference Module in Materials Science and Materials Engineering*: Elsevier.

Singh, S., Sachdeva, A., & Sharma, V. S. (2012). Investigation of dimensional accuracy/mechanical properties of part produced by selective laser sintering. *International Journal of Applied Science Engineering, 10*(1), 59-68.

Soe, S. P. (2012). Quantitative analysis on SLS part curling using EOS P700 machine. *Journal of Materials Processing Tech., 212*(11), 2433-2442. doi:10.1016/j.jmatprotec.2012.06.012

Soe, S. P., Eyers, D. R., & Setchi, R. (2013). Assessment of non-uniform shrinkage in the laser sintering of polymer materials. *The International Journal of Advanced Manufacturing Technology, 68*(1), 111-125. doi:10.1007/s00170-012-4712-0

Song, J., Gelin, J. C., Barrière, T., & Liu, B. (2006). Experiments and numerical modelling of solid state sintering for 316L stainless steel components. *Journal of Materials Processing Tech., 177*(1-3), 352-355. doi:10.1016/j.jmatprotec.2006.04.111

Song, S., Wang, A., Huang, Q., & Tsung, F. (2014). *Shape deviation modeling for fused deposition modeling processes.* Paper presented at the 2014 IEEE International Conference on Automation Science and Engineering (CASE).

Song, Y., Li, Y., Zhou, Z., Lai, Y., & Ye, Y. (2011). A multi-field coupled FEM model for one-step-forming process of spark plasma sintering considering local densification of powder material. *Full Set - Includes `Journal of Materials Science Letters', 46*(17), 5645-5656. doi:10.1007/s10853-011-5515-7

Starr, T. L., Gornet, T. J., & Usher, J. S. (2011). The effect of process conditions on mechanical properties of laser-sintered nylon. *Rapid Prototyping Journal, 17*(6), 418-423. doi:10.1108/13552541111184143

Steen, W. M. (2010). *Laser material processing* (4th ed ed.). New York: New York : Springer.

Suwanprateeb, J. (2007). Comparative study of 3DP material systems for moisture resistance applications. *Rapid Prototyping Journal, 13*(1), 48-52. doi:10.1108/13552540710719217

Talagani, M. R., DorMohammadi, S., Dutton, R., Godines, C., Baid, H., Abdi, F., . . . Blue, C. (2015). Numerical simulation of big area additive manufacturing (3D printing) of a full size car. *SAMPE Journal, 51*(4), 27-36.

Tong, K., Amine Lehtihet, E., & Joshi, S. (2003). Parametric error modeling and software error compensation for rapid prototyping. *Rapid Prototyping Journal, 9*(5), 301-313. doi:10.1108/13552540310502202

Tong, K., Joshi, S., & Amine Lehtihet, E. (2008). Error compensation for fused deposition modeling (FDM) machine by correcting slice files. *Rapid Prototyping Journal, 14*(1), 4-14. doi:10.1108/13552540810841517

Tontowi, A. E., & Childs, T. H. C. (2001). Density prediction of crystalline polymer sintered parts at various powder bed temperatures. *Rapid Prototyping Journal, 7*(3), 180-184. doi:10.1108/13552540110395637

Vandenbroucke, B., & Kruth, J.-P. (2007). Selective laser melting of biocompatible metals for rapid manufacturing of medical parts. *Rapid Prototyping Journal, 13*(4), 196-203. doi:10.1108/13552540710776142

Vyroubal, J. (2011). Compensation of machine tool thermal deformation in spindle axis direction based on decomposition method. *Precision Engineering, 36*(1). doi:10.1016/j.precisioneng.2011.07.013

Wachtman, J. B., Tefft, W. E., Lam, D. G., & Apstein, C. S. (1961). Exponential Temperature Dependence of Young's Modulus for Several Oxides. *Physical Review, 122*(6), 1754-1759. doi:10.1103/PhysRev.122.1754

Wang, A., Song, S., Huang, Q., & Tsung, F. (2017). In-Plane Shape-Deviation Modeling and Compensation for Fused Deposition Modeling Processes. *Automation Science and Engineering, IEEE Transactions on, 14*(2), 968-976. doi:10.1109/TASE.2016.2544941

Wang, D., Dong, A., Zhu, G., Shu, D., & Li, F. (2018). The propagation and accumulation of dimensional shrinkage for ring-to-ring structure in investment casting. *The International Journal of Advanced Manufacturing Technology, 96*(1), 623-629. doi:10.1007/s00170-018-1631-8

Wang, D., Yang, Y., Yi, Z., & Su, X. (2013). Research on the fabricating quality optimization of the overhanging surface in SLM process. *The International Journal of Advanced Manufacturing Technology, 65*(9-12), 1471-1484.

Wang, H., & Huang, Q. (2007). Using Error Equivalence Concept to Automatically Adjust Discrete Manufacturing Processes for Dimensional Variation Control. *Journal of Manufacturing Science and Engineering, 129*(3), 644. doi:10.1115/1.2714581

Wang, J. (1984). Young's modulus of porous materials. *Journal of Materials Science, 19*(3), 809-814. doi:10.1007/BF00540452

Wohlers, T. (2018). *Wohlers Report 2018*. Retrieved from

Wu, A., Brown, D., Kumar, M., Gallegos, G., & King, W. (2014). An Experimental Investigation into Additive Manufacturing-Induced Residual Stresses in 316L Stainless Steel. *Metallurgical and Materials Transactions A, 45*(13), 6260-6270. doi:10.1007/s11661-014-2549-x

Xing, Y. L., & Jiang, J. (2003). Environmental effects on the dimensions of SL5195 resin. *Rapid Prototyping Journal, 9*(2), 88-94. doi:10.1108/13552540310698152

Yang, H., Kong, Z., & Sarder, M. (2016). *Additive Manufacturing: A New Paradigm For Manufacturing.* Paper presented at the Proceedings of the 2016 Industrial and Systems Engineering Research Conference, Availability, Development.

Zeng, Q., Li, K., Fen-Chong, T., & Dangla, P. (2012). Effect of porosity on thermal expansion coefficient of cement pastes and mortars. *Construction and Building Materials, 28*(1), 468-475. doi:https://doi.org/10.1016/j.conbuildmat.2011.09.010

Zhang, L. C., & Attar, H. (2016). Selective Laser Melting of Titanium Alloys and Titanium Matrix Composites for Biomedical Applications: A Review *Advanced Engineering Materials, 18*(4), 463-475. doi:10.1002/adem.201500419

Appendix

Appendix A sPro60 compensation model code

```
clear all
close all
clc

[F,verte] = stlread('Tail_Lamp.stl');
thetaX=0;
thetaY=0;
thetaZ=0;
RX=[1 0 0; 0 cos(thetaX) -sin(thetaX); 0 sin(thetaX) cos(thetaX)];
RY=[cos(thetaY) 0 sin(thetaY); 0 1 0; -sin(thetaY) 0 cos(thetaY)];
RZ=[cos(thetaZ) -sin(thetaZ) 0; sin(thetaZ) cos(thetaZ) 0; 0 0 1];
vertexp=verte*RX*RY*RZ;

n=length(vertexp);

X=vertexp(:,1);
Y=vertexp(:,2);
Z=vertexp(:,3);
Volume=625998.1720;
d=0.5;
Max=max(Z);
Min=min(Z);
Z1=zeros (length(Z),1);
Length=length(Min:d:Max);
LA = zeros (Length,1);
XA = zeros (Length,1);
YA = zeros (Length,1);
xt = zeros (Length,1);
yt = zeros (Length,1);
Count = zeros (Length,1);
S=zeros(n/3,1);
for a=1:n/3
    a1=X(3*a-1)-X(3*a-2);
    a2=Y(3*a-1)-Y(3*a-2);
    a3=Z(3*a-1)-Z(3*a-2);
    b1=X(3*a)-X(3*a-2);
    b2=Y(3*a)-Y(3*a-2);
    b3=Z(3*a)-Z(3*a-2);
    S(a)=sqrt((a2*b3-b2*a3)^2+(b1*a3-a1*b3)^2+(a1*b2-b1*a2)^2)/2;
end

N=1;
SUM=sum(S);
for m=Min:d:Max
    XT=0;
    SXT=0;
    YT=0;
    SYT=0;
    count =0;
    for i=1:n

            if Z(i)>=m && Z(i)<m+d
```

```
                count=count+S(ceil(i/3))/SUM;
                XT=XT+X(i)*S(ceil(i/3));
                SXT=SXT+S(ceil(i/3));
                YT=YT+Y(i)*S(ceil(i/3));
                SYT=SYT+S(ceil(i/3));
            end

    end
    Count(N)=count;
    XA(N)=XT/SXT;
    YA(N)=YT/SYT;
    N=N+1;

end
LA=Count/3*Volume/d;
Num=1;
MAXA(1)=XA(1);
MAXA(2)=(XA(1)+XA(2)+XA(3))/3;
MAXA(Length-1)=(XA(Length)+XA(Length-1)+XA(Length-2))/3;
MAXA(Length)=XA(Length);
MAYA(1)=YA(1);
MAYA(2)=(YA(1)+YA(2)+YA(3))/3;
MAYA(Length-1)=(YA(Length)+YA(Length-1)+YA(Length-2))/3;
MAYA(Length)=YA(Length);
MALA(1)=LA(1);
MALA(2)=(LA(1)+LA(2)+LA(3))/3;
MALA(Length-1)=(LA(Length)+LA(Length-1)+LA(Length-2))/3;
MALA(Length)=LA(Length);
for a=3:Length-2
    MAXA(a)=(XA(a-2)+XA(a-1)+XA(a)+XA(a+1)+XA(a+2))/5;
    MAYA(a)=(YA(a-2)+YA(a-1)+YA(a)+YA(a+1)+YA(a+2))/5;
    MALA(a)=(LA(a-2)+LA(a-1)+LA(a)+LA(a+1)+LA(a+2))/5;
end
for m=Min:d:Max
    for i=1:n
        if Z(i)>=m && Z(i)<m+d
            if MALA(Num)<5000
                Z1(i)=Z(i)-1.3*(0.00005)*((X(i)-MAXA(Num))^2)-
(0.00005)*(Y(i)-MAYA(Num))^2;
            else
                Z1(i)=Z(i)-1.3*(0.00005+MALA(Num)*(Max-
Z(i))*1.8125/(10^10))*((X(i)-MAXA(Num))^2)-(0.00005+MALA(Num)*(Max-
Z(i))*1.8125/(10^10))*(Y(i)-MAYA(Num))^2;
            end
        end
    end
    Num=Num+1;
end
vertex=[X,Y,Z1];
vvertex=vertex*inv(RZ)*inv(RY)*inv(RX);
% Open the file for writing
 stlwrite('Tail_Lamp_compensation.stl',F,vvertex);
```

Appendix B sPro230 compensation model code

```
set(handles.edit13,'String','Loading');
file1=get(handles.edit1,'String');
path1=get(handles.edit2,'String');
file2=get(handles.edit3,'String');
path2=get(handles.edit4,'String');
thetaX=str2double(get(handles.edit7,'String'));
thetaY=str2double(get(handles.edit8,'String'));
thetaZ=str2double(get(handles.edit9,'String'));
positionX=str2double(get(handles.edit21,'String'));
positionY=str2double(get(handles.edit22,'String'));
positionZ=str2double(get(handles.edit23,'String'));
Volume=str2double(get(handles.edit10,'String'));
d=str2double(get(handles.edit11,'String'));


[F,verte] = stlread([path1 file1]);

RX=[1 0 0; 0 cos(thetaX) -sin(thetaX); 0 sin(thetaX) cos(thetaX)];
RY=[cos(thetaY) 0 sin(thetaY); 0 1 0; -sin(thetaY) 0 cos(thetaY)];
RZ=[cos(thetaZ) -sin(thetaZ) 0; sin(thetaZ) cos(thetaZ) 0; 0 0 1];
vertexp=verte*RX*RY*RZ;
n=length(vertexp);

X=vertexp(:,1);
Y=vertexp(:,2);
Z=vertexp(:,3);
Max=max(Z);
Min=min(Z);
Z1=zeros (length(Z),1);
Length=length(Min:d:Max);
XA = zeros (Length,1);
YA = zeros (Length,1);
Count = zeros (Length,1);
S=zeros(n/3,1);
for a=1:n/3
    a1=X(3*a-1)-X(3*a-2);
    a2=Y(3*a-1)-Y(3*a-2);
    a3=Z(3*a-1)-Z(3*a-2);
    b1=X(3*a)-X(3*a-2);
    b2=Y(3*a)-Y(3*a-2);
    b3=Z(3*a)-Z(3*a-2);
    S(a)=sqrt((a2*b3-b2*a3)^2+(b1*a3-a1*b3)^2+(a1*b2-b1*a2)^2)/2;
end

N=1;
SUM=sum(S);
for m=Min:d:Max
    XT=0;
    SXT=0;
    YT=0;
    SYT=0;
    count =0;
    for i=1:n
        if Z(i)>=m && Z(i)<m+d
            count=count+S(ceil(i/3))/SUM;
            XT=XT+X(i)*S(ceil(i/3));
```

```
            SXT=SXT+S(ceil(i/3));
            YT=YT+Y(i)*S(ceil(i/3));
            SYT=SYT+S(ceil(i/3));
        end
    end
    Count(N,1)=count;
    if XT==0
        if N==1
            XA(N,1)=0;
        else
            XA(N,1)=XA(N-1,1);
        end
    else
        XA(N,1)=XT/SXT;
    end
    if YT==0
        if N==1
            YA(N,1)=0;
        else
            YA(N,1)=YA(N-1,1);
        end
    else
        YA(N,1)=YT/SYT;
    end
    N=N+1;

end
LA=Count/3*Volume/d;

MAXA(1)=XA(1);
MAXA(2)=(XA(1)+XA(2)+XA(3))/3;
MAXA(Length-1)=(XA(Length)+XA(Length-1)+XA(Length-2))/3;
MAXA(Length)=XA(Length);

MAYA(1)=YA(1);
MAYA(2)=(YA(1)+YA(2)+YA(3))/3;
MAYA(Length-1)=(YA(Length)+YA(Length-1)+YA(Length-2))/3;
MAYA(Length)=YA(Length);

MALA(1)=LA(1);
MALA(2)=(LA(1)+LA(2)+LA(3))/3;
MALA(Length-1)=(LA(Length)+LA(Length-1)+LA(Length-2))/3;
MALA(Length)=LA(Length);

for a=3:Length-2
    MAXA(a)=(XA(a-2)+XA(a-1)+XA(a)+XA(a+1)+XA(a+2))/5;
    MAYA(a)=(YA(a-2)+YA(a-1)+YA(a)+YA(a+1)+YA(a+2))/5;
    MALA(a)=(LA(a-2)+LA(a-1)+LA(a)+LA(a+1)+LA(a+2))/5;
end

Num=1;
for m=Min:d:Max
    for i=1:n
        if Z(i)>=m && Z(i)<m+d
            if MALA(Num)<5000
                Z1(i)=Min+(Z(i)-Min)/(1.01-0.00006*(Z(i)-Min+positionZ))-
1.25*0.00001*((X(i)-MAXA(Num))^2)-0.00001*(Y(i)-MAYA(Num))^2;
            else
                Z1(i)=Min+(Z(i)-Min)/(1.01-0.00006*(Z(i)-Min+positionZ))-
```

```
0.00001*((MALA(Num)/5000)^(1/3))*(Z(i)-2*Min+Max)/(Max-Min)*(1.25*((X(i)-
MAXA(Num))^2)+(Y(i)-MAYA(Num))^2);
            end
        end
    end
    Num=Num+1;
end

vertex=[X,Y,Z1];
vvertex=vertex*inv(RZ)*inv(RY)*inv(RX);
% Open the file for writing
stlwrite([path2 file2],F,vvertex);
f = warndlg('This work is finished.', 'Finish');
set(handles.edit13,'String','Finish');
drawnow     % Necessary to print the message
waitfor(f);
set(handles.edit13,'String','-');
```

Appendix C Manual of program for sPro230

1. *Click the Open button to select Original STL file*
2. *Click the Open button to select a new file storage location and name*
3. *Enter the entire volume of the part on Volume column*
4. *Input the layer depth for calculating compensation algorithm*
5. *After clicking OK button, please wait until Finish appears in the State column*

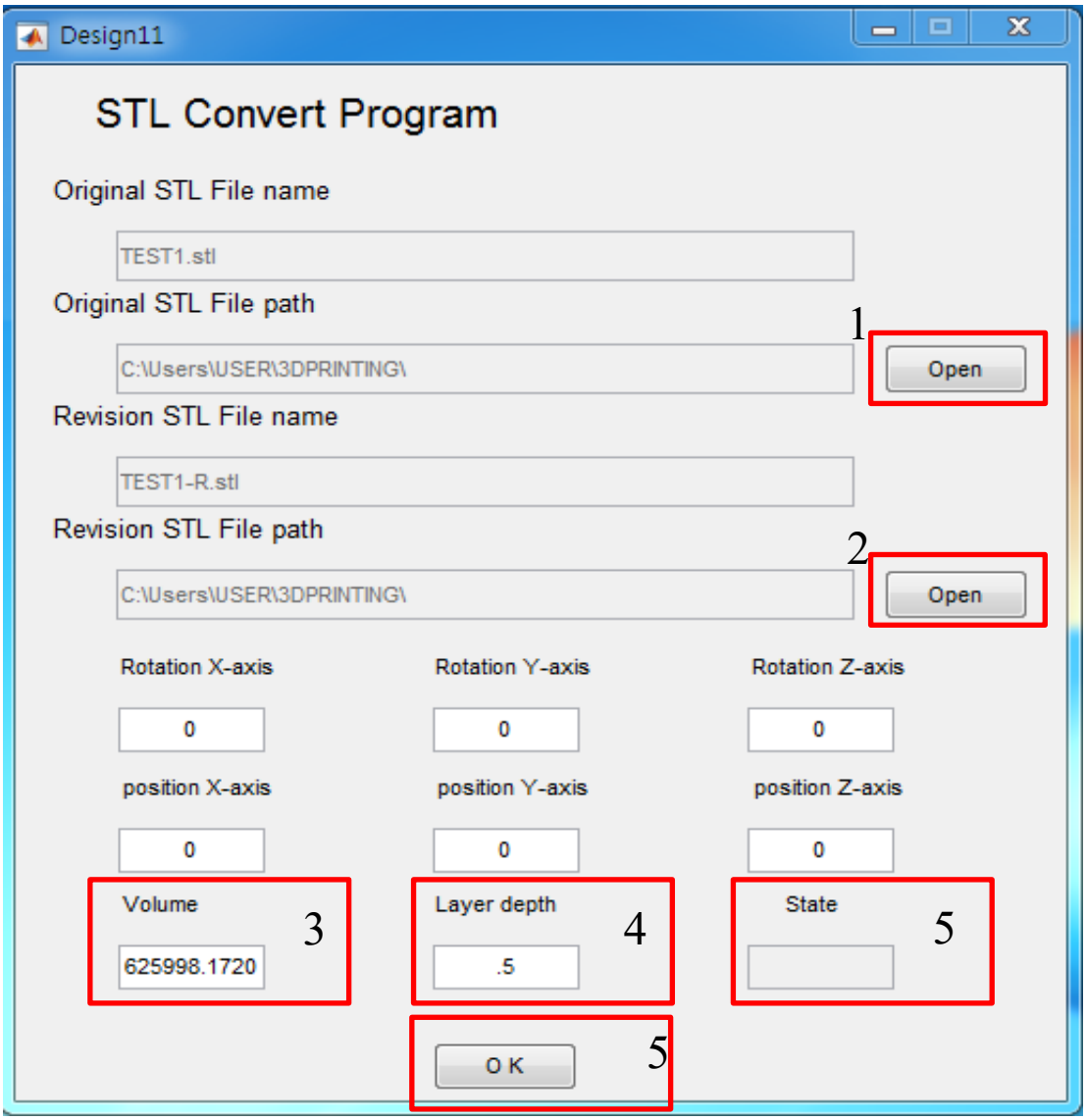

Acknowledgement

Above all, I would like to sincerely thank my advisor, Prof. Namhun Kim for his guidance and support. I could complete my Ph.D. course through his belief and passionate encouragement. During my 20s, I received a lot of good memories and experiences from my advisor at UNIST. I also thank my other committee members, Prof. Duck Young Kim, Daeil Kwon Young-bin Park and In Gwun Jang. When I was a junior of undergraduate student, I changed my second track to the engineering design track and got a lot of guidance from Prof. Duck Young Kim with Namhun Kim. When I became a graduate student, Prof. Daeil Kwon supported my research. When I was an undergraduate, I took the most classes from Prof. Young-bin Park. And I was able to build a lot of knowledge. And I would like to thank Prof. In Gwun Jang for giving me a lot of advice on how to improve my dissertation so that I can make it a better dissertation. And I want to show my sincere appreciation to Hyunshik Shin senior manager, Hyeonnam Kim manager, Cheolwoong Hwang manager of GM Korea and all the other people who worked with me on the project.

I thank senior and junior of U-CIM. When I first came into U-CIM lab, Moise Busogi, Hae-seung Park, Yeong-gwang Oh, and A-rm Yoo all gave me a lot of advice. Thank you very much. And I enjoyed the class that I attended with Woo-yeol Lee. Jeong-sik Kim, who spent the most time with me and helped me when I was in need. When I wanted to play, I played with him. Thanks to you, I carry a lot of good memories. First of all, I am especially grateful to Dr. Eunju Park and Dr. Ju Youn Kwon for helping me find many flaws and correct them in my dissertation, and also to Hae Kwon Jung for English proofreading. Thank you 3DAM members and Jin-sik Kim for helping me with my research. And I thanks to all of my juniors who helped me a lot, Dong-hwan Song, Ik-chan Joo, Hwee-young Han, Hae-joon Choi, Eun-seo Lee, Moon-yeong Lee, Ga-hyung Kim and Tae-Yang Choi, I was able to live happily in the lab.

And I thank my friends who studied and shared a lot of experiences at UNIST. I had a lot of pleasant experiences with Seungwon Kim who used the same room the most. I would like to thank Sujeong Baek for helping me all the way from undergraduate to graduate school. Also, I enjoyed spending time with all of you, Seona Kim, Anjung Lee, Minho Hong, Kangmin Lee, Daniel Song and all other friends. I thank all my friends for their friendship and pleasant memories. And above all, as my girlfriend for 10 years at UNIST, Ji-ae Park, who has been with me all the time at UNIST, is the biggest axis of my self-esteem. She always fills my deficiencies and encourages me. I love you.

Lastly, I want to thank my family for always supporting, helping, and believing in my choices. I was able to complete my Ph.D course because of my family's infinite love and trust. Thank you all and love you.